NASA/CR—2012-217655

Dielectric Barrier Discharge Plasma Actuator for Flow Control

Final Report

Dmitry F. Opaits
Princeton University, Princeton, New Jersey

September 2012

NASA STI Program . . . in Profile

Since its founding, NASA has been dedicated to the advancement of aeronautics and space science. The NASA Scientific and Technical Information (STI) program plays a key part in helping NASA maintain this important role.

The NASA STI Program operates under the auspices of the Agency Chief Information Officer. It collects, organizes, provides for archiving, and disseminates NASA's STI. The NASA STI program provides access to the NASA Aeronautics and Space Database and its public interface, the NASA Technical Reports Server, thus providing one of the largest collections of aeronautical and space science STI in the world. Results are published in both non-NASA channels and by NASA in the NASA STI Report Series, which includes the following report types:

- TECHNICAL PUBLICATION. Reports of completed research or a major significant phase of research that present the results of NASA programs and include extensive data or theoretical analysis. Includes compilations of significant scientific and technical data and information deemed to be of continuing reference value. NASA counterpart of peer-reviewed formal professional papers but has less stringent limitations on manuscript length and extent of graphic presentations.

- TECHNICAL MEMORANDUM. Scientific and technical findings that are preliminary or of specialized interest, e.g., quick release reports, working papers, and bibliographies that contain minimal annotation. Does not contain extensive analysis.

- CONTRACTOR REPORT. Scientific and technical findings by NASA-sponsored contractors and grantees.

- CONFERENCE PUBLICATION. Collected papers from scientific and technical conferences, symposia, seminars, or other meetings sponsored or cosponsored by NASA.

- SPECIAL PUBLICATION. Scientific, technical, or historical information from NASA programs, projects, and missions, often concerned with subjects having substantial public interest.

- TECHNICAL TRANSLATION. English-language translations of foreign scientific and technical material pertinent to NASA's mission.

Specialized services also include creating custom thesauri, building customized databases, organizing and publishing research results.

For more information about the NASA STI program, see the following:

- Access the NASA STI program home page at *http://www.sti.nasa.gov*

- E-mail your question to *help@sti.nasa.gov*

- Fax your question to the NASA STI Information Desk at 443–757–5803

- Telephone the NASA STI Information Desk at 443–757–5802

- Write to:
  STI Information Desk
  NASA Center for AeroSpace Information (CASI)
  7115 Standard Drive
  Hanover, MD 21076–1320

NASA/CR—2012-217655

Dielectric Barrier Discharge Plasma Actuator for Flow Control

Final Report

Dmitry F. Opaits
Princeton University, Princeton, New Jersey

Prepared under Cooperative Agreement NNX07AC02A

National Aeronautics and
Space Administration

Glenn Research Center
Cleveland, Ohio 44135

September 2012

Acknowledgments

This thesis presents results of my five year long research at Princeton University which would not have been possible without the contribution of many people. I am sincerely thankful to my advisor, Professor Richard Miles, whose motivation, mentorship, and support from the beginning to the end of my studies at Princeton have enabled me to develop into the researcher that I am. Thank you Professor Miles for teaching me to see new opportunities, rather than problems in any challenges I face. It was an honor for me to work with Dr. Sergey Macheret and Dr. Mikhail Shneider. To Sergey, I am grateful for his continued involvement and guidance in my research, especially being all the way out on the West Coast. To Mikhail, for always having his door widely open and our timely discussions regarding subjects ranging from gigantic red sprites to neurophysiology. I also want to thank Dr. Macheret and Professor Luigi Martinelli for their time and valuable suggestions regarding my manuscript.

I am thankful to Alexander Likhanskii for being my colleague in solving DBD mysteries for the last five years, in particular for providing the numerical part of the solution. I would also like to mention Alex Critien (Oxford University), Gabriele Neretti (University of Bologna), Matthew Edwards (Princeton University), and Dr. Sergey Leonov (Institute for High Temperatures, Russian Academy of Sciences), who have worked with me during different stages of my research.

I would also like to thank fellow members of the Applied Physics Group for their camaraderie and valuable contribution to my overall success here at Princeton: Sohail Zaidi, Phil Howard, Arthur Dogariu, Adom Giffin, Chiranjeev, Bruce, Manny, and James. I want to thank Tim Ombrello and Sang Hee Won from Professor Yiguang Ju lab for help with ozone visualization. I am thankful to the PU Russians, too many to list here, for the wonderful time I had in Princeton. A special thanks to Dr. David Ashpis from NASA Glenn for long-term financial support which made this work possible.

This dissertation carries the number T−3218T in the records of the Department of Mechanical and Aerospace Engineering.

This work was sponsored by the Fundamental Aeronautics Program at the NASA Glenn Research Center.

Level of Review: This material has been technically reviewed by NASA technical management.

Available from

NASA Center for Aerospace Information
7115 Standard Drive
Hanover, MD 21076–1320

National Technical Information Service
5301 Shawnee Road
Alexandria, VA 22312

Available electronically at http://www.sti.nasa.gov

Abstract

Electrohydrodynamic (EHD) and magnetohydrodynamic phenomena are being widely studied for aerodynamic applications. The major effects of these phenomena are heating of the gas, body force generation, and enthalpy addition or extraction, [1, 2, 3]. In particular, asymmetric dielectric barrier discharge (DBD) plasma actuators are known to be effective EHD device in aerodynamic control, [4, 5]. Experiments have demonstrated their effectiveness in separation control, acoustic noise reduction, and other aeronautic applications. In contrast to conventional DBD actuators driven by sinusoidal voltages, we proposed and used a voltage profile consisting of nanosecond pulses superimposed on dc bias voltage. This produces what is essentially a non-self-sustained discharge: the plasma is generated by repetitive short pulses, and the pushing of the gas occurs primarily due to the bias voltage. The advantage of this non-self-sustained discharge is that the parameters of ionizing pulses and the driving bias voltage can be varied independently, which adds flexibility to control and optimization of the actuators performance. Experimental studies were conducted of a flow induced in a quiescent room air by a single DBD actuator. A new approach for non-intrusive diagnostics of plasma actuator induced flows in quiescent gas was proposed, consisting of three elements coupled together: the schlieren technique, burst mode of plasma actuator operation, and 2-D numerical fluid modeling. During the experiments, it was found that DBD performance is severely limited by surface charge accumulation on the dielectric. Several ways to mitigate the surface charge were found: using a reversing

DC bias potential, three-electrode configuration, slightly conductive dielectrics, and semi conductive coatings. Force balance measurements proved the effectiveness of the suggested configurations and advantages of the new voltage profile (pulses+bias) over the traditional sinusoidal one at relatively low voltages. In view of practical applications certain questions have been also addressed, such as electrodynamic effects which accompany scaling of the actuators to real size models, and environmental effects of ozone production by the plasma actuators.

Contents

List of Figures

List of Tables

Chapter 1

Introduction and Background

Sapere aude

Flow control consists of manipulating a flow to achieve a desired change. Usually it means modifying the laminar-to-turbulent transition in the boundary layer and preventing flow separation, increasing the lift and reducing the drag of an airfoil, enhancing mixing or reducing acoustic noise. It is of great practical importance for aerospace industry, commercial and military aviation, energy systems, automobile industry, and everywhere where external and internal airflows occur.

There are several mechanisms through which the flow can be manipulated. Control over laminar-to-turbulent transition can be very beneficial. For example, in certain cases the turbulent boundary layer can have an order of magnitude higher skin-friction drag than the laminar one. For aircrafts and cars suppression of transition means better fuel efficiency, longer ranges, and higher speeds.

The range of operational conditions for a wind turbine, take-off and landing speeds of an aircraft, maneuverability of a fighter jet are highly affected by maximum lift and stall characteristics of the airfoil. The produced lift depends on the ability of the flow to follow the curve and increases with the angle of attack and camber of the

wing. At some point however the flow fails to follow the curve and separates. Thus suppression of boundary layer separation is one of the main opportunities for flow control.

Another important issue is the acoustic noise produced by turboprops, helicopters, cars, wind turbines (infra sound), etc. It is associated with the turbulent nature of many flows and is an area where flow control can have a significant impact. In some circumstances turbulence is desired since it enhances mixing and here again, the flow control can play an important role.

The title of this thesis is "Dielectric barrier discharge plasma actuator for flow control." It follows from the title that the problem is quite multidisciplinary and requires expertise in several areas to tackle it, namely "dielectric" and "barrier" requires knowledge in material sciences, "discharge" and "plasma" – in gas discharge physics and plasma physics, "flow" stands for fluid mechanics, and "actuator" and "control" for control theory. There are also a few areas which are not mentioned explicitly but are implied – optical diagnostics, high voltage electronics, electrodynamics. To avoid spreading out our efforts to all of these areas of science and engineering we concentrated mostly on the DBD plasma part, keeping in mind that its application would be for flow control.

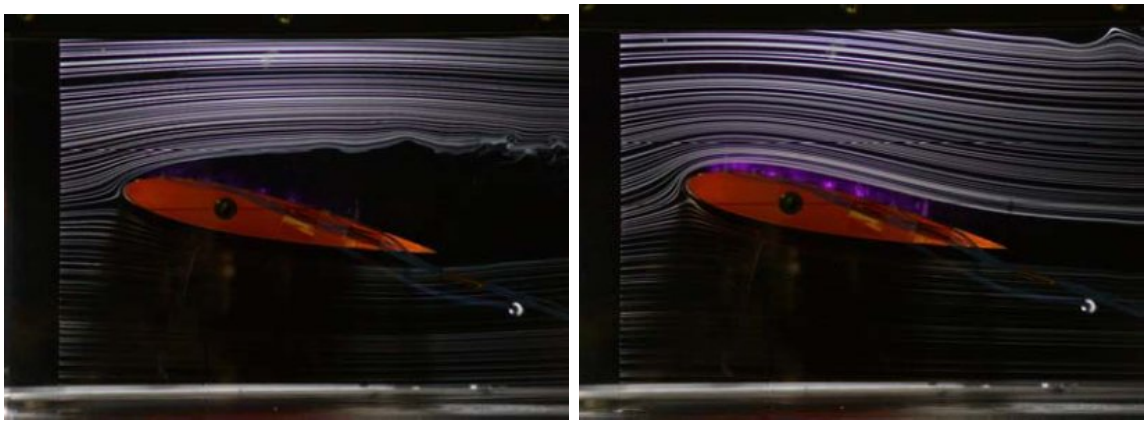

Figure 1.1: DBD plasma flow control. Plasma OFF (left), plasma ON (right). Taken from [6]

1.1 Background

The story of DBD plasma actuators for flow control began in 1998 when Reece Roth from University of Tennessee presented his first paper [9] on DBD flow control. His demonstration of DBD flow control capabilities is shown at Figure 1.1, where he demonstrated that separation at high angles of attack can be suppressed. The main advantages of plasma actuators are their robustness, simplicity, light weight, low power consumption, and fast enough response time to make them capable of real-time flow control.

Since 1998, interest in DBD plasma actuators has been growing exponentially as is illustrated by number of Google hits on "plasma actuator" at Figure 1.2. Still, understanding of the underlying physics is incomplete, and, although several approaches have been shown to improve the performance of plasma actuators, only a complete understanding of both plasma processes and their interaction with the flow will allow optimization of the performance. It is the intention of this dissertation to investigate mechanisms of DBD plasma actuator flow control and suggest further improvements to it.

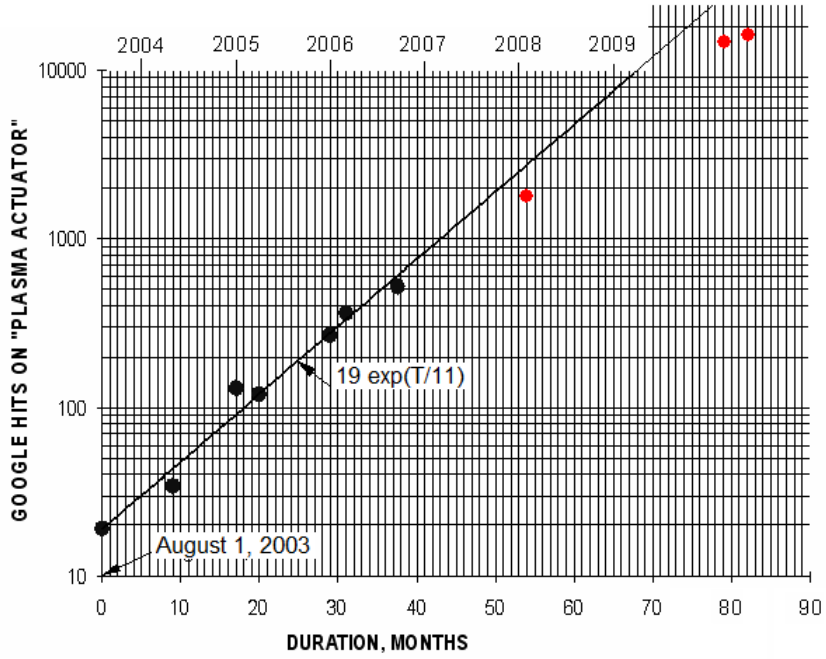

Figure 1.2: Interest in plasma actuators. Some data are taken from [7].

The introduction would not be complete without mentioning that, even though DBD plasma actuators were introduced to current public by R. Roth, they were known back in the sixties in Soviet Ukraine, [8]. Figure 1.3 shows a schematic of one of those experiments. The configuration is slightly different from the one suggested by Roth. The top electrode is flush mounted on the airfoil and the segmented bottom electrode consists of several wires embedded into the flap. Regardless this difference, the plasma induced flow velocities and separation control results were similar to those obtained nowadays. The reason the technology has been forgotten was probably because at those times most efforts were spent on super- and hyper-sonic flights, and the plasma induced flows of the orders of 10 m/s did not look that impressive after all.

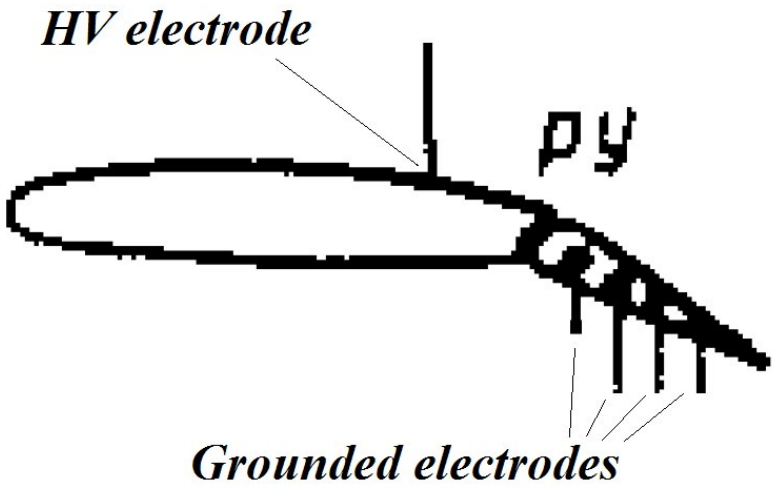

Figure 1.3: DBD plasma actuator in 1968, from [8].

1.1.1 Dielectric barrier discharge

A dielectric barrier discharge (DBD) is an electrical discharge between two electrodes separated by an insulating dielectric barrier. It was first reported by Werner von Siemens in 1857, [19], as a new method of ozone generation. Originally it was called the silent discharge in contrast with a spark discharge, which is accompanied by substantial heating and generation of an audible noise. From a fundamental point of view, the main difference between DBD and spark discharges is the presence of the dielectric barrier which precludes dc operation of the DBD. DBDs are usually driven by sinusoidal voltages at frequencies between 0.05 and 500 kHz or by high voltage pulses. When the applied voltage reaches breakdown value, the electric current deposits surface charge onto the dielectric and the discharge self-terminates.

In most cases the DBD in room air is not uniform and consists of numerous microdischarges, as shown at Figure 1.4. Let us take a closer look at the plasma formation process, [20]. A typical breakdown starts with one free electron. When the electric field reaches the breakdown value the free electron produces secondary

electrons by direct ionization and starts an electron avalanche. In certain cases, if the Meek condition is satisfied, [21], the avalanche develops into a streamer discharge. After several nanoseconds, the streamer filament reaches the dielectric barrier, and builds up surface charge on the surface. At this point the local electric field collapses, which leads to self-termination of the discharge leaving a cloud of electrons and ions. In atmospheric pressure air it takes about 10 nanoseconds for the electrons to attach to molecular oxygen forming negative ions. The residual ion-ion cloud decays in microseconds due to recombination processes and drift/diffusion to the walls. If the next breakdown happens while the ion plasma is still present or before the local heating has dissipated it will most likely follow the same path. That is why it is possible to see a stable pattern of the microdischarges in DBD, even though each of them consists of multiple sequential streamers. Sometimes the plasma decays and thermalizes completely before the next breakdown occurs so the streamers start at random locations each time. In this case the discharge appears uniform and its structure can be revealed only by using ultra fast cameras.

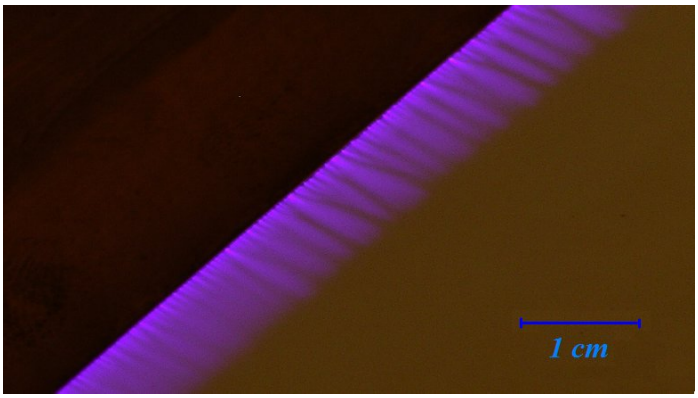

Figure 1.4: DBD plasma appearance.

Typical parameters of a microdischarge are summarized in Table 1.1, from [22]. As we can see, the plasma is highly non-equilibrium with hot electron and cold heavy particles. This characterizes most applications for the discharge, where energetic

electron efficiently transfer energy to ionization, electron excitation, and electron impact dissociation, but not significantly to direct heating.

Lifetime	1–20 ns	Filament radius	50–100 μm
Peak current	0.1 A	Current density	0.1–1 kA cm^{-2}
Electron energy	1–10 eV	Electron density	10^{14}–10^{15} cm^{-3}
Total transported charge	0.1–1 nC	Gas temperature	Close to average, about 300K
Total dissipated energy	5μJ	Reduced electric field	E/n = (1–2)(E/n)Paschen
Overheating	5K		

Table 1.1: Typical parameters of a microdischarge.

In more than 150 years of studies, the DBD has found many industrial applications such as for ozone generation, for high-power CO_2 lasers, and as a UV-source in eximer lamps. Most notably DBD's are used in plasma display panels of large-area flat television screens. DBD's are widely used for polymer surface treatment to promote wettability and adhesion; and for pollution control to remove dust or CO, NO_x, and VOCs from exhaust gases. Among recent and yet to be perfected DBD applications are plasma medicine/sterilization, plasma assisted ignition and combustion, and plasma aerodynamics.

1.1.2 Flow control

There are many definitions of boundary layer flow control, one of which was given by Flatt in 1961 [23], stating: "Boundary layer control includes any mechanism or process through which the boundary layer of a fluid flow is caused to behave differently than it normally would were the flow developing naturally along a smooth straight surface."

Ludwig Prandtl was the first one to realize importance of the boundary layer on the entire flow structure in 1904. He was also the one who demonstrated active

flow control by delaying separation from the surface of cylinder using boundary layer suction, [24]. Since then the field of flow control has grown and many other flow control methods have been developed, both active and passive. Detailed description of them can be found in the literature, see [25] for example. The most common boundary layer control techniques are briefly discussed below:

- **Boundary layer bleed.** We will start with the very first method, which Prandtl used in his original experiment, boundary layer suction. As the boundary layer loses its momentum due to viscous effects, in the presence of adverse pressure gradients the flow direction along the surface can reverse, causing flow separation. Using porous surface or discrete suction slots, the low-momentum part of the boundary layer can be withdrawn from the flow, making the profile fuller. This method has been proven to be effective at both low and high speeds with most of the remaining problems being maintainability and reliability of the suction surfaces. Special care should be taken to protect the suction surface from dust, insects, and ice formation.

- **Boundary layer blowing.** Similar to the previous method, in this case the boundary layer is being manipulated using discrete slots at the wall. In contrast to the previous method, the velocity profile is made fuller not by removing a layer of slow air at the wall but by direct tangential injection of air at high speed along the surface. This flow control technique has been applied to military fighters and STOL transports. High-pressure bleed-air is readily available from the jet engines. Although generally less efficient than suction, blowing requires less interior ducting. In some application, the blowing allows a lighter, cooler or non-reacting gas to be introduced into the boundary layer to provide thermal protection at hypersonic speeds.

- **Passive vortex generators.** Passive vortex generators are essentially small-

aspect-ratio airfoils mounted normal to the surface of a wing. Being large enough to stick out of the boundary layer into the free stream, they create stream-wise vortices which circulate the retarded near-wall flow with the free stream flow, increasing the near wall flow velocity. This approach of boundary layer manipulation is passive, it does not require any power source to operate and is always ON. Among its advantages are simplicity and robustness. The freedom to choose the shapes and positions of the vortex generators on an airplane wing or turbine blade leaves many opportunities for optimization. On the other hand, the vortex generators cannot adapt to changing flight conditions, and they cause parasitic drag. Nevertheless, they are widely used in most modern commercial airplanes.

- **Boundary layer turbulizers.** Another similar method is based on using groves or rough surfaces to trip the boundary layer and trigger laminar-to-turbulent transition. A turbulent boundary layer is more resistant to separation than a laminar one, and, mostly for that reason, transition advancement may be beneficial in some situations. The mechanism is similar to the previous one, where large-scale vortices provided mixing. Momentum transfer in a turbulent boundary layer is strongly enhanced due to the presence of eddies in the flow, which make the velocity profile fuller and delay separation.

- **Acoustic excitations and periodic forcing.** Other methods for active boundary layer control include acoustic excitations and periodic excitations of the boundary layer. Similarly to the previous method, both of these techniques rely on triggering laminar-to-turbulent transition, but the difference is that they are active are can be applied any time needed. It has been observed that sound of a particular frequency and intensity can affect the boundary layer. The source of the acoustic waves can either be internal – mounted on the surface,

or external – outside of the boundary layer. Periodic forcing was also found to be effective. In this case the velocity field is disturbed directly by computer controlled flaps, oscillating wires, or piezo elements. Both acoustic and periodic forcing methods achieved their best control at specific frequencies which are generally found to occur at a Strouhal number, St = f c/U_∞ (f is frequency, c is the chord's length, U_∞ in the free stream velocity), near unity.

1.2 Literature review of DBD flow control

The conventional DBD plasma actuator consists of two plane electrodes flush mounted asymmetrically on both sides of dielectric, with one electrode encapsulated, and the other exposed to the atmospheric air, as shown at Figure 1.5. The electrodes are usually made of copper or aluminum foil, however thin wires have also been tried as top electrode in some works, see [26] for example. A variety of other DBD plasma actuator geometries exist, for example the double barrier DBD plasma actuator, where both electrodes are covered with dielectric, [27], or the annular DBD plasma actuator, in which the electrodes have a shape of concentric rings, [28]. Different dielectric materials are used in DBDs, such as glass, quartz, kapton, teflon, and ceramics. The thickness of the dielectric varies over a wide range from 100 μm to 6.35 mm (1/4 inch). The discharge is ignited by applying high voltage to one of the electrodes, the other electrode is usually grounded.

The DBD plasma actuator is usually driven by a high voltage sinusoidal voltage profile 1-20 kV, 0.05-20 kHz, however other shapes (triangular, positive and negative sawtooth) have also been tested, see [29]. Sometimes DBD plasma actuators are driven by high voltage nanosecond pulses, [30, 31, 10]

The DBD is normally accompanied by several effects, such as ionic wind, heating, acoustic effects, and plasma chemistry. If the driving voltage is modulated these

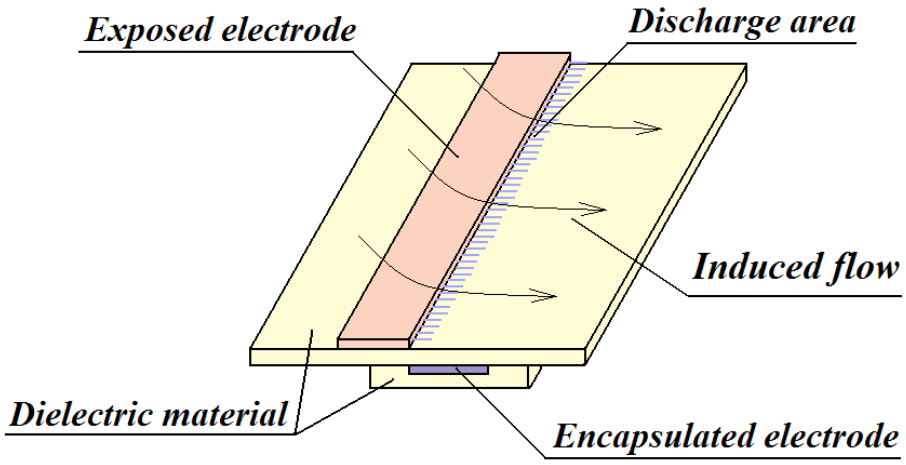

Figure 1.5: Conventional dielectric barrier discharge plasma actuator.

effects become periodic. Different groups have utilized one or the other of these effects, to substitute for a well known mechanical flow control device, usually treating the other phenomena as side effects. So far several mechanisms associated with DBD actuator boundary layer control have been suggested and demonstrated.

- **Introducing momentum into boundary layer.**

  The first method is based on the fact that the DBD imparts momentum into the air. The actuator is placed span-wise and the induced force adds momentum to the decelerated boundary layer in the stream-wise direction, as shown in Figure 1.6.

  This mechanism is very popular and most research groups have used this configuration in their studies. It is very similar to mechanical blowing through slots but it does not introduce additional mass into the flow. If needed, the actuator can be reversed to cause flow separation. The drawback of this method is that in order to be successful the discharge must induce flows with velocities on the order of the boundary layer velocities. Thus, successful demonstrations of the

flow control have primarily been successful at free stream speeds up to 30 m/s due to the low velocity of the DBD surface jet. To overcome this problem the following method was suggested.

- **Creating streamwise vortices.** Similar to the passive vortex generators discussed earlier, the purpose of the stream-wise mounted plasma actuators (which induce flow in span-wise direction) is not to accelerate the boundary layer, but to create stream-wise vortices which will replace the slow boundary layer with high momentum free stream. The idea to use DBD's in such way was first suggested by Roth et al [9] and is illustrated at Figure 1.7. It was later developed by other groups, see [32] for example. They were able to demonstrate that plasma induced flow is more effective for separation control if used to create these vortices than to accelerate the retarded boundary layer directly.

- **Periodic forcing.** Since it has been known from mechanical flow control that

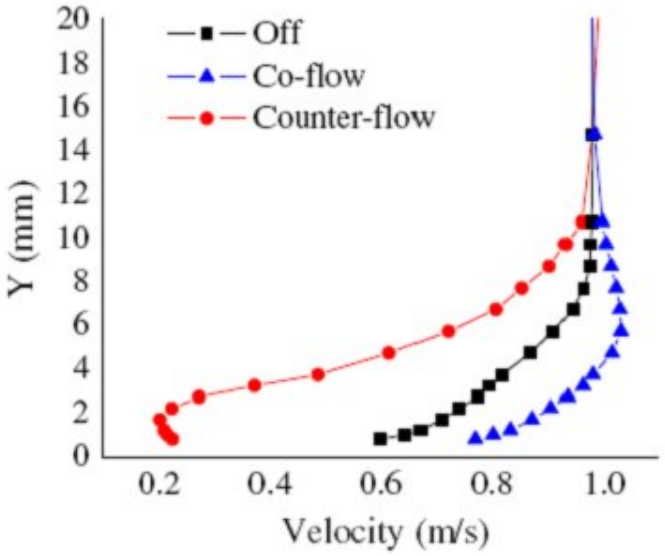

Figure 1.6: Velocity profiles in the boundary layer of a 5 m/s free airflow along a flat plate, with co- and counter-flows, from [9].

the introduction of periodic disturbances near the separation location can prevent or delay the onset of separation, the same approach was undertaken for plasma flow control. Corke et al, [5], performed a set of experiments on flow reattachment around an airfoil NACA 0015 at 21 m/s using a 17 kHz sinusoidal driving field with a variable duty cycle. The 12 in. DBD strip was located at the leading edge of the wing. They discovered that at 10% duty cycle, the stall angle of attack (α_{stall}) was higher than with steady operation as shown at Figure 1.8.

Naturally the flow separates around $\alpha = 15°$ at these conditions with no DBD actuation. When the actuator was ON in "steady" operation, meaning 100% duty cycle, the stall angle increased to 18°. The results at $\alpha = 16°$ are presented in the left part of Figure 1.8. These show that a clear minimum in the voltage required to re-attach the flow exists at an unsteady frequency that is close

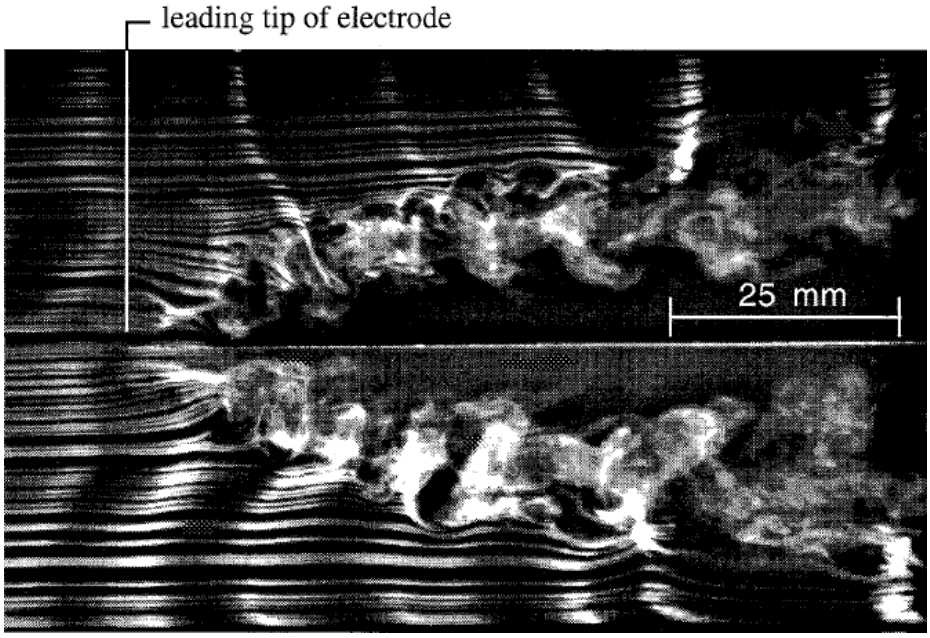

Figure 1.7: Smoke visualization of free airflow along a flat plate with a streamwise DBD actuator, flow speed 5 m/s, from [9].

to that for which St = 1. This frequency was then used for the "unsteady" operation that gave the results in C_L versus α in the right part of Figure 1.8. The unsteady actuator with periodic forcing at St = 1 gave significantly better results than the steady operation. The authors discovered that it significantly increased $C_{L_{max}}$ and α_{stall}, and maintained lift to $\alpha = 22°$, which was 7° past the natural stall angle of attack. Similar improvements were also found for a higher free-stream speed. Note that the power to the actuator was only 10% of that for the steady operation, approximately 2 Watts for the 12 in. span.

- **Acoustic excitations.** In a number of works [10, 33] Starikovskii et al used high voltage (upto 50kV) nanosecond pulses to drive the DBD plasma actuator. Plasma induced gas velocities show near-zero values for nanosecond pulses and the authors relied on tripping and periodic forcing of the boundary layer. Ac-

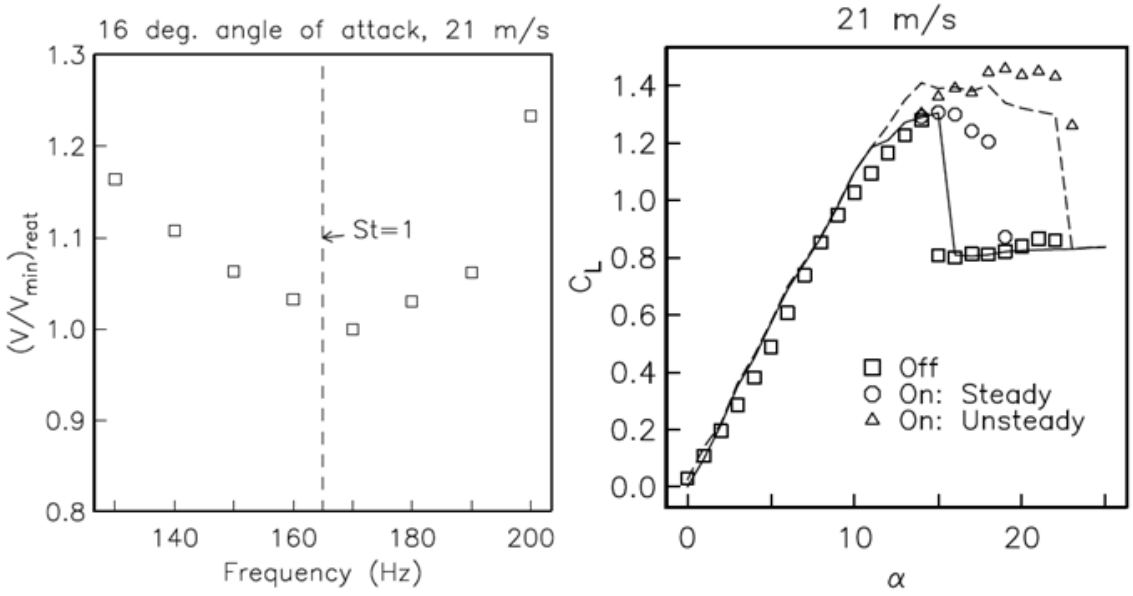

Figure 1.8: Minimum voltage required to re-attach the flow as a function of the actuator frequency for "unsteady" operation at $\alpha = 16°$ (left), and lift coefficient versus angle of attack with leading-edge actuator off and on at optimum Strouhal number, from [5].

cording to the authors, the measurements showed overheating in the discharge region and fast ($\tau \approx 1$ μs) thermolization of the plasma deposited energy. The peak values of the temperature increase of the plasma layer reached 400 K for 50-ns pulse durations. This heating produced an emerging shock wave together with the secondary vortex flows which disturbed the main flow, see Figure 1.9.

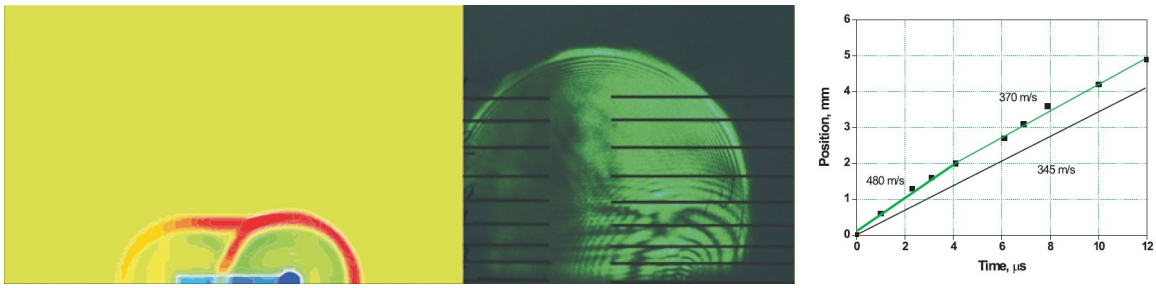

Figure 1.9: Shock wave produced by a single 50 kV 50 ns long pulse. Left: numerical modeling, discharge with hot spot near the edge of the exposed electrode; center: experimental shadow images of shock waves formation; right: shock wave position vs time; from [10].

The resulting pulsed-periodic disturbance causes an efficient transverse momentum transfer into the boundary layer and further flow attachment to the airfoil surface. It thus can be concluded, that for periodic pulsed nanosecond dielectric barrier discharge, the main mechanism of impact is the energy transfer to and heating of the near-surface gas layer. The following pulse-periodic vortex movement trips the boundary layer and stimulates redistribution of the main flow momentum. The authors were able to control boundary layer separation, lift, and drag force coefficients, and obtain acoustic noise reduction in the Mach number range of 0.05 to 0.85.

- **Heating effects.** If the DBD is driven by a sinusoidal voltage, the heat release is more uniform in time. However it is interesting that the major heat release does not necessary happen in the bulk of plasma. The IR image of a DBD plate

with single trace of a hot electrode is shown in Figure 1.10.

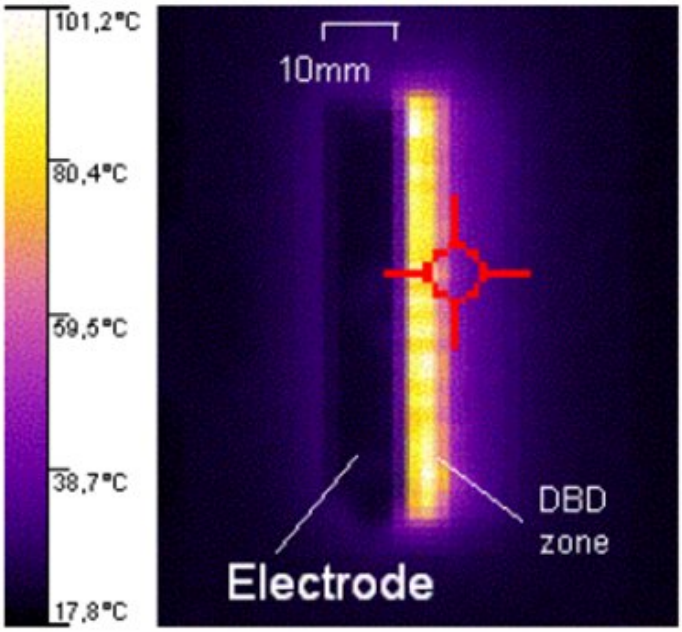

Figure 1.10: IR image of DBD, from [11].

This image was recorded after 30 sec of DBD run time. Leonov et al, [11], showed that there is significant heating of the dielectric surface by the discharge. They suggested that it occurs due to active charged particles deposition on the surface with sequential recombination and thermal energy release. This localized heating increases the viscosity of the gas promoting separation. It also lowers the gas density, deflecting the stream lines and changing the effective shape of the aerodynamic profile, which can be beneficial in some cases.

Regardless the number of configurations DBD plasma actuators can be used to control the flow they all rely on two major effects: heating (fast or steady state) and body force. The flexibility of DBD plasma actuators is that depending on the choice of the driving voltage waveforms the same device can produce different effects on the flow. The DBD allows fast switching between body steady state and periodic

force production, acoustic perturbation, and heating regimes of operation. As it was mentioned above another name for DBD is silent discharge because of the relatively low heating compared to a spark. Thus the heating itself can be more effectively produced using other forms of gas discharge, such as sparks and arcs. There are even simpler solutions which do not involve plasmas. Steady state heating can be produced by ohmic elements. Fast acoustic perturbations of the boundary layer can be produced using piezo elements which possess all advantages of the plasma actuator, they are light weight, small, robust, and very fast. For these reasons this work does not address eating or acoustic effects, but concentrates on body force production, its mechanism and enhancement.

Implicit factors that affect DBD performance

While the instrumentation error of most experiments presented in this work is less than 5% and the accuracy of the data acquired is high, the total error is pretty large. On day-to-day basis variations in readings as high as 25% for some measurements could be observed.

The reason is that some factors which have effect on the overall DBD performance were not monitored or taken into account. All the experiments were performed in room air. Weather outdoors and air conditioning in the lab affected the temperature, pressure and humidity of the room air. Daily temperature and pressure fluctuations can lead to 1 to 3 % variations in air density. This would change the reduced electric field and consequently many plasma processes, for example ionization, which exponentially depends on the field. But this hardly compares with the humidity effects on the DBD performance. It is known that water vapor is a strong electro-negative gas. High humidity increases the breakdown voltage and decreases the ionization level and size of plasma. Recently Benard et al, [12], showed that the DBD induced

flow velocity decreases by a factor of 2 when the relative humidity goes from 40% to 85% and another factor of 2 at 98% relative humidity, Figure 1.11.

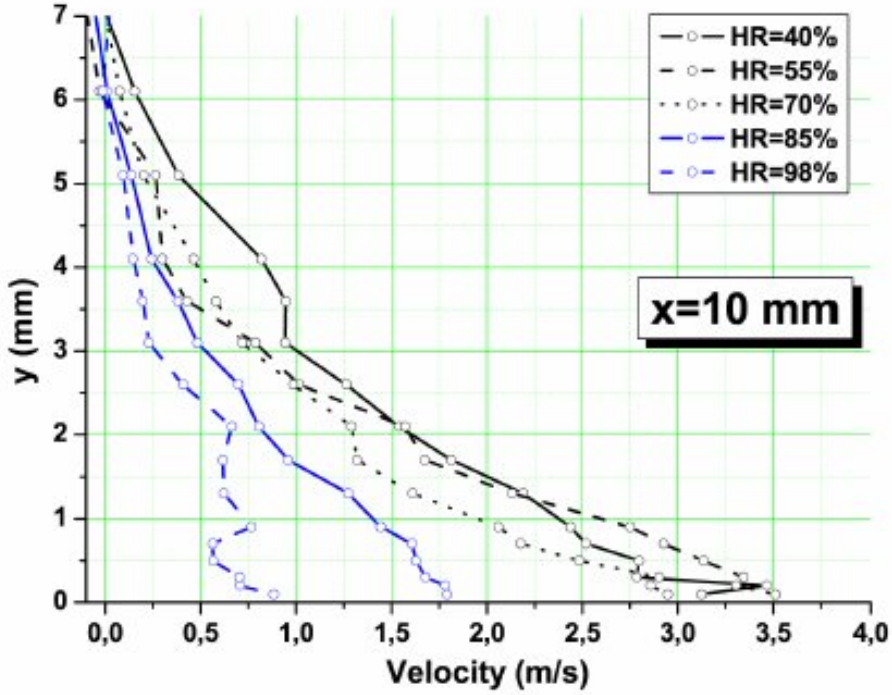

Figure 1.11: DBD induced flow profiles at different values of relative humidity, from [12].

Variations in performance can also be caused by certain dielectric material properties. In DBD plasma actuator problems the dielectric has been usually characterized by two parameters: thickness and dielectric permittivity. Together with electrode configurations and dielectric material these parameters define the electric field and therefore the plasma properties. Until recently these properties had been considered to be constants in DBD related problems. However, even if the thickness of a dielectric is constant, its electric permittivity may not be. In [34] the dependence of the dielectric constant on many factors is considered. For example, the electric permittivity depends on frequency of the applied voltage, temperature, and humidity. Plots

for kapton and MACOR dependences (materials we used in our DBD experiments) on these parameters are presented at Figure 1.12. The data were taken from [13, 14].

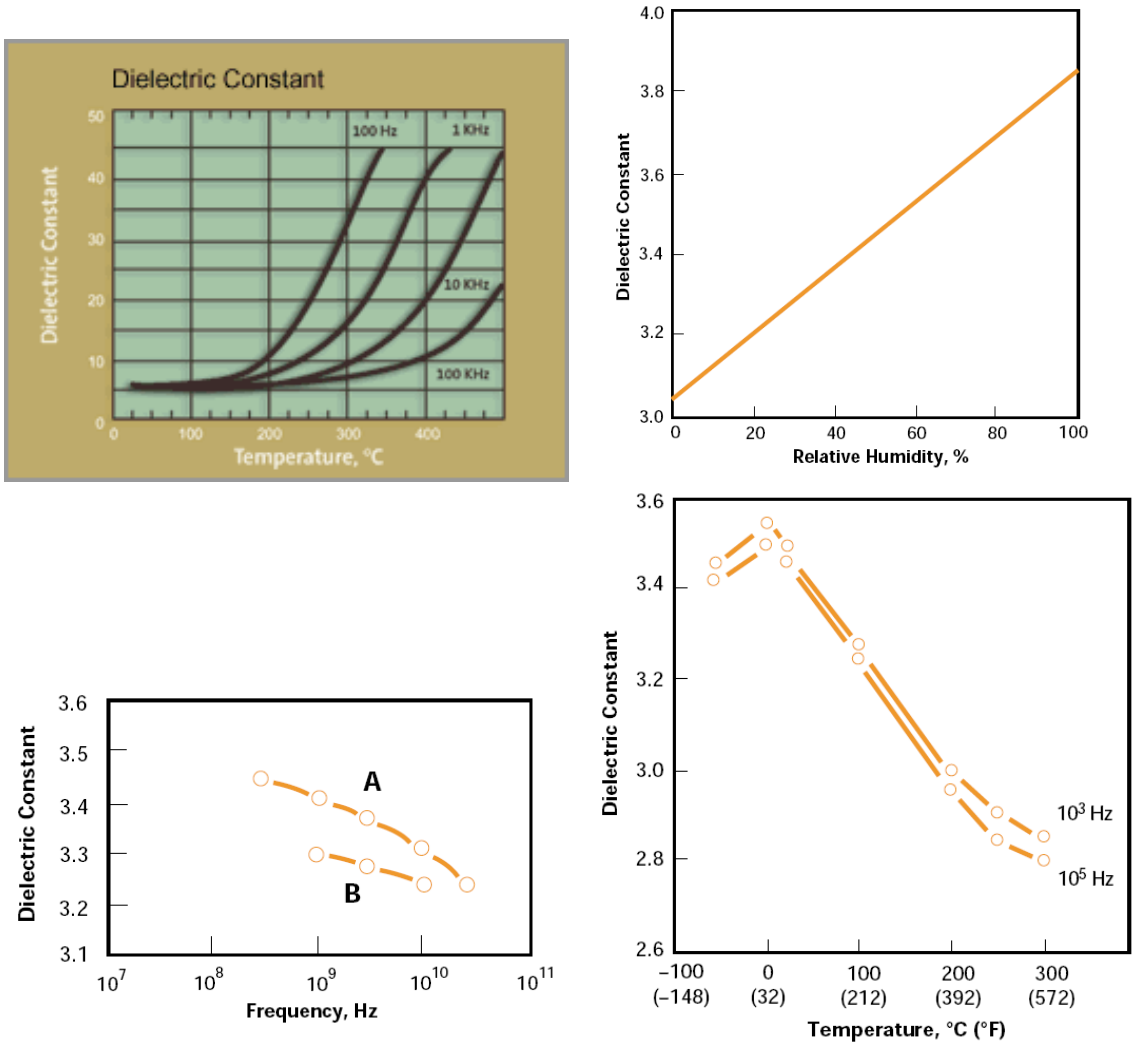

Figure 1.12: Dependence of dielectric permittivity on temperature, frequency and humidity for MACOR (left on the top, data taken from [13]) and Kapton (the other three plots, data taken from [14])

Based on these plots it is evident that the DBD plasma actuator performance can change from day to day due to its dependence on humidity. Temperature dependence can lead to other effects. For example, if the actuator is running for a long time

it heats up. Leonov et al, [11], showed that the dielectric surface can get up to 80 C in 30 seconds of actuators operation. That means its performance will change with time as the actuator is run. The results will also differ if it is a cold run or if it was run just recently and the dielectric is still hot. External flows can provide additional cooling and in laboratory supersonic flows, the wall recovery temperature is usually significantly from room temperature. Another important dependence is voltage frequency. For example, if the DBD is driven by 10 kHz sinusoidal voltage, the dielectric will have one dielectric constant for the 10 kHz electric field and another, lower one, for fast electric field changes caused by ∼10 ns breakdowns. As we can see from the plots, the frequency dependence becomes more crucial as temperature increases, which is very important for high temperature applications of DBD plasma actuators.

1.3 Goals of this research

The main objective in this dissertation was to establish a comprehensive understanding of force production mechanisms in DBD plasma actuators and enhance them. The aim of the work was to break down the process into simple steps and get control over each of them. Certain tasks were not planned in advance but came up as the research advanced. In view of practical applications certain questions were also addressed, such as scaling the actuators to large scales, and ozone production by the actuator. The specific goals and milestones to achieve these objectives are as follows:

1. Design and development non-intrusive diagnostics for DBD plasma actuator characterization. These included schlieren visualization for the plasma induced flow, non-contacting potential measurements of the surface charge, thrust stand measurements for force production in DBD, Pitot probe sensing of the induced

wall jet profile, and visualization of ozone by absorption. The setup should provide a stable, repeatable, and rigid platform to capture various aspects of the DBD plasma actuator performance.

2. Develop simple numerical and analytical models in support of the experiments and to provide a better understanding of the underlying physics and prediction of further steps in the research.

3. Experimental investigation of the dielectric barrier discharge plasma, its characteristics, and the induced flow. Compare the obtained data against the numerical prediction to ensure correct interpretation of the results. Based on the obtain results further investigate the possibility of more effective momentum coupling into the flow using DBD plasma actuators.

The work was positioned as a research and not testing of a plasma device. Thus more attention was paid to understanding the underlying physics and distinguishing the essential processes involved, rather then quantifying the actuator's performance within high accuracy.

1.4 Outline of this dissertation

Chapter 2 introduces the Princeton approach for enhancing the body force production in DBD plasma actuators. This chapter also describes the electric circuit used to power the actuator and presents distinctive features of working with high voltage nanosecond pulses.

Chapter 3 presents results of the schlieren visualization of the plasma induced flow. The results show the effectiveness of pulses+bias voltage profile and suggest the importance of the surface charge that limits the actuator's performance. A new

pulses+ac bias configuration is proposed.

Chapter 4 shows the surface charge evolution (build up, saturation, and depletion) on the dielectric surface for pulsed and sinusoidal driven DBDs. Numerical simulation confirms experimental data. Based on the results of the charge distribution, a new three-electrode configuration is introduced.

Chapter 5 presents results of the force produced by DBD plasma actuators. In addition to pulses+ac bias and three-electrode configuration, DBDs with slightly conductive dielectric and semi-conductive coatings are tested. The result show consistency with schlieren visualization. Comparison with sinusoidally driven DBDs show advantage of pulses+bias waveform.

Chapter 6 provides details about DBD induced flow in quiescent air. The obtained results show the laminar wall jet structure of the flow. An analytical model in boundary layer approximation is developed and shown to be in agreement with the experimental data.

Chapter 7 points out the importance and evaluates ozone production by the actuator. It discusses its potential importance for flow tagging, environment and combustion applications.

Chapter 8 addresses scaling issues which may arise when the actuator is scaled up to a real size aircraft wing. Electrodynamic effects in long plasma actuators are studied both numerically and experimentally.

Chapter 9 concludes the dissertation with a summary of the major developments of the DBD plasma actuator project and a review of its major contributions. The chapter also contains suggestions for further directions of the research which may lead towards the downstream goal of applying the concept to an actual flow control problem.

Chapter 2

High Voltage Power Supply

The majority of the groups studying DBD plasma actuators use a sinusoidal voltage to drive it. In such a case the sine voltage performs two functions simultaneously: plasma production when the electric field reaches breakdown values and body force production between the breakdowns. In such DBD actuators, ionizing pulses (streamer breakdowns) occur randomly, the magnitude and frequency of those ionizing pulses depend entirely on the parameters of the sinusoidal driving voltage. In contrast, the Princeton approach consists in using high voltage repetitive nanosecond pulses superimposed on dc or low-frequency bias voltage. We proposed and used what is essentially non-self-sustained discharge: the plasma is generated by repetitive short pulses, and the pushing of the gas occurs primarily due to the low-frequency (bias) voltage. The advantage of this non-self-sustained discharge is that the parameters of ionizing pulses and the driving bias voltage can be varied independently, which adds flexibility to control and optimization of the actuator performance. The comparison of the approaches can be illustrated by a diagram at Figure 2.1.

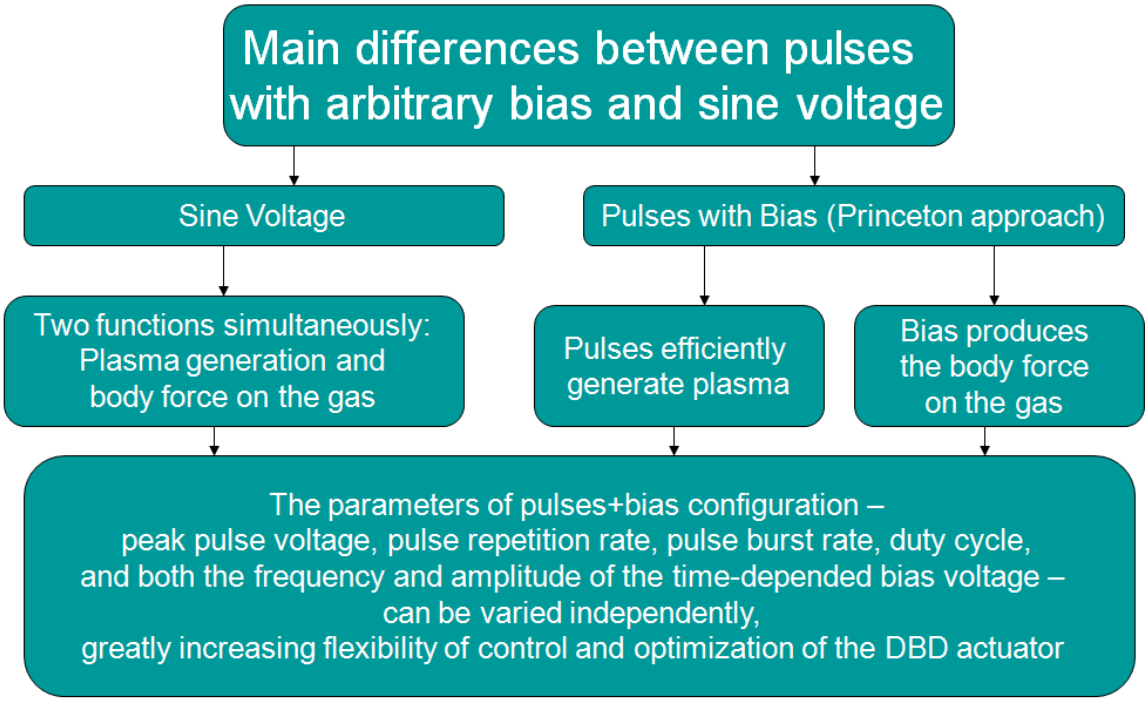

Figure 2.1: Princeton approach.

2.1 Power Circuit

To create the "pulses+bias" voltage profile a circuit was designed so as to superimpose short pulses on a low frequency bias voltage without interference between the pulser and the low frequency power supply. The design of the circuit slightly changed over time but its principle design remained the same. It included a capacitor (100-470 pF) in series with the actuator, which protected the pulser from the bias voltage. Since the capacitance of the actuator was only 4-30 pF (depending on its size and the dielectric used), the main pulse voltage drop occurred just at the plasma actuator. To keep the high voltage nanosecond pulses from going into bias voltage source, 220 kΩ resistors or ferrite rings (high inductances) were used. The charging time for the capacitor through the corresponding resistors was $\tau = \mathrm{RC} = 220\ \mathrm{k\Omega} \times 470\ \mathrm{pF} = 100\ \mu\mathrm{s}$, which corresponds to 10 kHz $\gg$ the 100 Hz, highest frequency of the bias voltage

used in the studies. In early experiments a 10 MΩ resistor was put in parallel with the actuator for safety reasons, but later it was found to be unnecessary. It was used to discharge the high voltage electrode after experiments. Its high impedance did not influence the circuit in any way. Also, a non-inductive matching resistor was added in parallel with the actuator to minimize the pulse reflection. The problem of the impedance matching will be addressed later in this chapter.

Two pulsers and several sources of the bias voltage were used in the experiments over five years of research.

2.1.1 FID Technology pulser FPG 30-100

A pulser used in early experiments (schlieren visualization, Chapter 3, and surface charge measurements, Chapter 4) was an FID Technology pulser FPG 30-100 4 ns full width at half maximum (FWHM). The pulser was capable of running with pulse repetition rate (PRR) of up to 100 kHz, and it was triggered by a 10 V pulse from a Stanford Research, Inc. Pulse Generator. The peak output voltage of the pulser was up to 10 kV which was fed to three separate 3 m long 75 Ω coaxial lines. The three copropagating pulses were converted into a single pulse by taking advantage of the short physical "length" of the pulses, less than 1 m. By connecting the center conductor of the first coaxial line to the outer conductor of the second and the center conductor of the second to the outer conductor of the third, an amplified pulse is produced between the center conductor of the third line and the outer conductor of the first, as shown at Figure 2.2. This essentially is a transformer made of sections of transmission lines, and it is well described in the literature, [35].

The pulser was able to produce pulses of negative polarity only. The bias voltage could be of any polarity but could be added to the pulsed electrode only due to the circuit properties. The terminology used in this work came from the numerical sim-

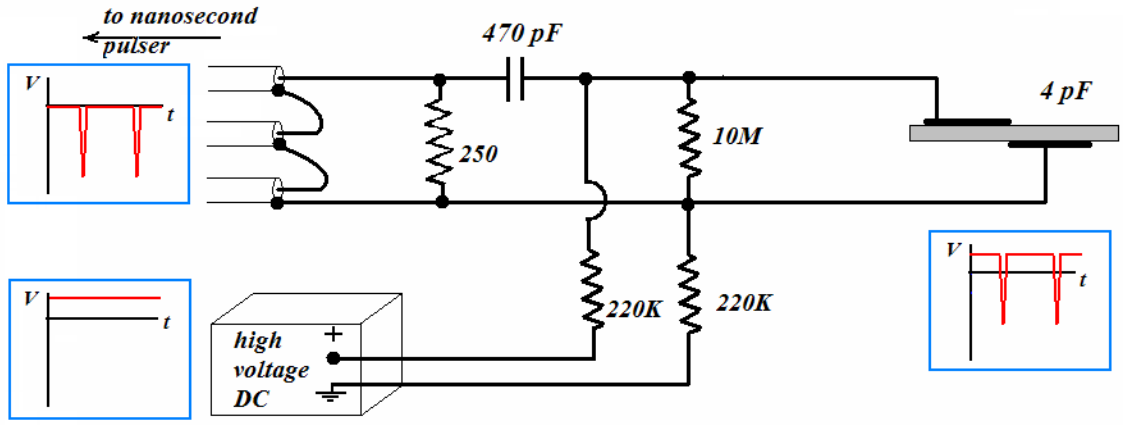

Figure 2.2: Electric circuit with FID Technology pulser FPG 30-100. The circuit is designed so as to combine short pulses with a low frequency bias voltage without interference between the pulser and the low frequency power supply. In experiments with sinusoidal bias, the dc power supply was replaced by a high-voltage transformer.

ulations, where the encapsulated electrode was considered grounded, and the voltage waveform was applied to the exposed electrode. Following the same terminology, we consider the encapsulated electrode to be at zero potential. That means that the term positive refers to a case when the electric field is directed from the exposed electrode to the encapsulated one, i.e., parallel to the induced jet, and negative when in the opposite direction. Thus, applying negative pulses to the lower encapsulated electrode will henceforth be referred to as positive pulses. Further, applying negative bias voltage to the top exposed electrode will be called a negative bias, whereas applying negative bias voltage to the lower encapsulated electrode will be referred to as positive bias. See Figure 2.3 for further examples.

2.1.2 FID Technology pulser FPG 25-200MC4

As the experiments moved forward, a question was raised about the role of the ionizing pulse duration. It was desirable to have pulses of both polarities, but not negative

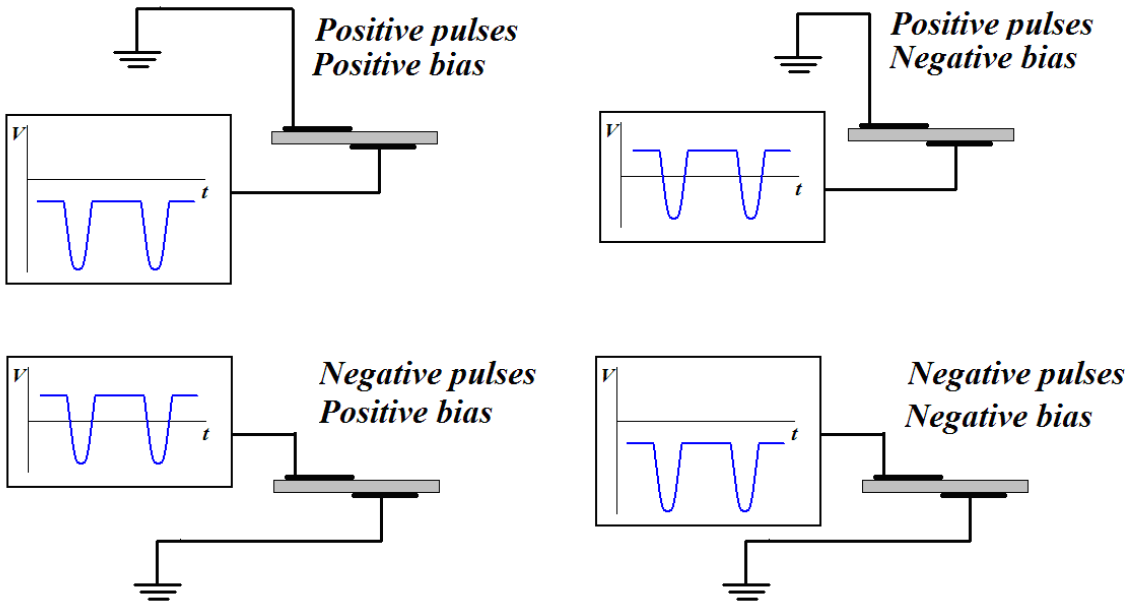

Figure 2.3: Terminology used in the paper for the pulse and bias voltage polarities. The encapsulated electrode is always considered to be at zero potential. The sign of potential of the exposed electrode relative to the encapsulated one determines the pulse and bias polarity.

only, and expand the range of other pulse parameters, such as peak voltage and repetition rate. A new FID Technology pulser FPG 25-200MC4 was purchased for this purpose. It is designed to produce positive and negative voltage pulses with the maximum amplitude of up to +/- 6.25 kV into 125-250 Ω, rise time of 2 ns and the duration of about 3, 7 and 13 ns at 90% of maximum voltage (combined output is 25 kV into 500-1000 Ohm). The pulse duration was changed by replacing pulse forming modules inside of the pulser. The pulse full width at half maximum (FWHM) of the pulses was measured and equals to 5.5, 10, and 17 ns. The pulse profiles at matching load (300 Ω non-inductive resistor) is shown at Figure 2.4.

Similar to previous pulser, its operational principle was based on a transformer made of sections of transmission lines. However the new pulser has four 75 Ω cables – two positive and two negative – and connects to a load as shown at Figure 2.5.

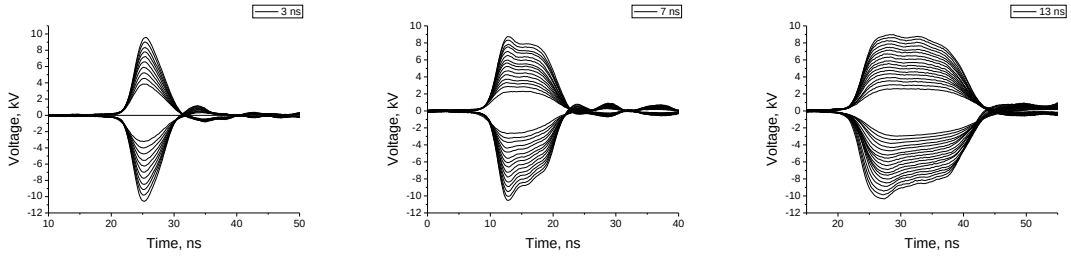

Figure 2.4: High voltage pulse profiles for different pulse widths, FID Technology pulser FPG 25-200MC4.

An example of the electric circuit with the new pulser is shown in Figure 2.6. In this example a high voltage pulse is applied to the top electrode only. To increase the effective pulse voltage, the bottom electrode can be connected to the pulser's cable of the opposite polarity, instead of the ground. In this case both electrodes are driven with the identical pulses of the opposite polarities, which doubles the pulse peak voltage.

The pulser was used in thrust measurement experiments, Chapter 5, ozone visualization, Chapter 8, and to study electro-dynamic effects in long DBDs, Chapter 7.

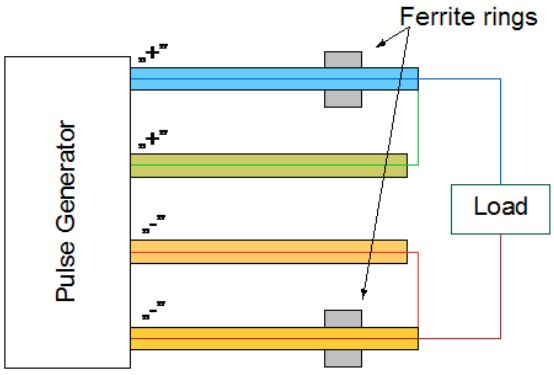

Figure 2.5: Load connection diagram for FID Technology pulser FPG 25-200MC4.

2.1.3 Nanosecond pulse profile

Special attention was paid to the electric pulse waveform. It was measured using a fast high-voltage probe (LeCroy PPE6 kV 400 MHz bandwidth, 5 MΩ input resistance, less than 6 pF input capacitance, or LeCroy PPE20 kV 100 MHz bandwidth, 100 MΩ input resistance, less than 3 pF input capacitance) connected to fast oscilloscope (Tektronix TDS 380, 400 MHz bandwidth, or LeCroy WavePro 7300A, 3GHz bandwidth). Since the pulses are only several nanoseconds long, they are reflected back from the plasma actuator and then reflected again by the pulser toward the actuator. Therefore, each pulse actually looks like a series of damped pulses. To reduce this ringing, a computer code incorporating the actuators and the probes capacitances was developed. The code calculated the reflection of a pulse from a RLC load. The code was based on Kirchhoffs laws written for an LRC load connected to a $3 \times 75\ \Omega = 225\ \Omega$ cable. The load consisted of a capacitance (representing DBD actuator) connected in parallel with a resistor (a matching load). The inductance of the connecting wires was also taken into account. The discharge contribution to the impedance was neglected. A schematic of the transformer made of sections of transmission lines connected to a RLC load is shown in Figure 2.7a. In the figure, Z is the cable impedance, Z_0 is defined by parasitic impedances and/or impedance of cable connecting wires, C is the capacitance of the actuator and the voltage probe, R is resistance of the noninductive matching resistor, and L_R and L_C are inductances of the connecting wires. Note that usually $Z_0 \gg nZ$, where n is the number of the cables. This simplifies the circuit to the one shown in Figure 2.7b.

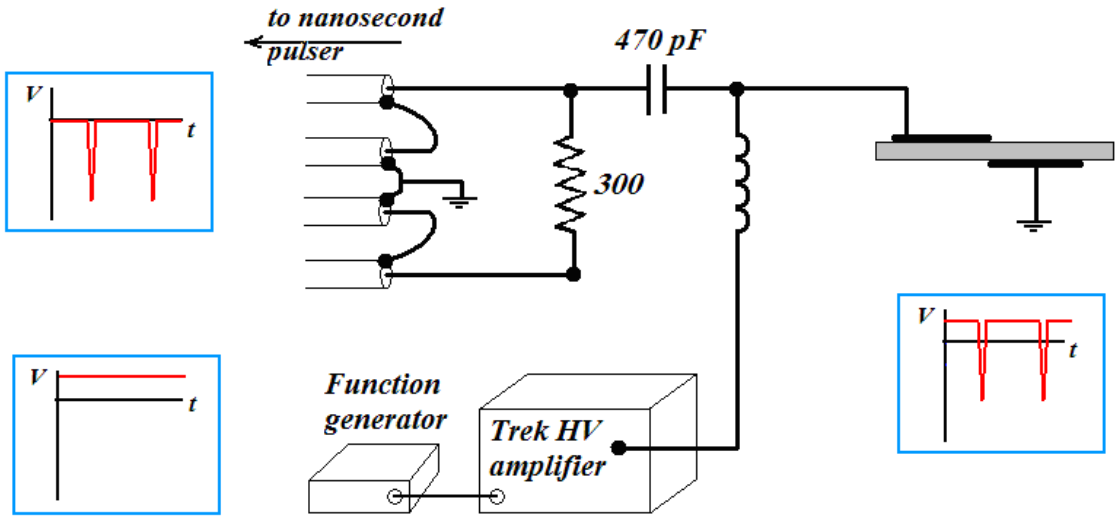

Figure 2.6: Electric circuit with FID Technology pulser FPG 25-200MC4. The circuit is designed so as to combine short pulses with a low frequency bias voltage without interference between the pulser and the HV amplifier.

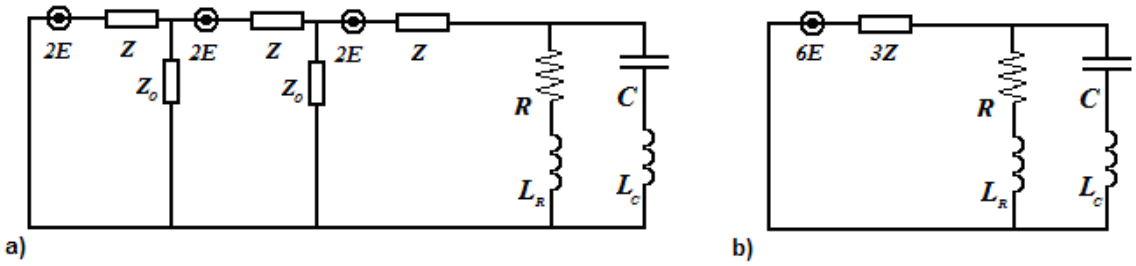

Figure 2.7: An equivalent scheme of the transformer made of sections of transmission lines connected to the RLC load. a) full circuit. b) reduced circuit.

Kirchhoffs laws for this circuit can be written as,

$$6E = 3Z_0(I_{RL} + I_{LC}) + I_{RL}R + L_R\frac{dI_{RL}}{dt} \tag{2.1}$$

$$6E = 3Z_0(I_{RL} + I_{LC}) + V + L_C\frac{dI_{LC}}{dt} \tag{2.2}$$

$$V = \frac{1}{C}\int_0^t I_{LC}d\tau \tag{2.3}$$

From these, we get the following set of two integro-differential equations for the currents:

$$\frac{dI_{RL}}{dt} = \frac{1}{L_R}\left(6E - 3Z_0(I_{RL} + I_{LC}) - I_{RL}R\right) \tag{2.4}$$

$$\frac{dI_{LC}}{dt} = \frac{1}{L_C}\left(6E - 3Z_0(I_{RL} + I_{LC}) - \frac{1}{C}\int_0^t I_{LC}d\tau\right) \tag{2.5}$$

Solving the set of equations using first order explicit Eulers method, we obtain the dependence of the currents on time. From that, the time-dependent voltage on the plasma actuator and of the reflected pulse is calculated as

$$V_{reflected} = 3Z_0(I_{RL} + I_{LC}) - 3E \tag{2.6}$$

In the absence of a reactive load, this gives a well-known result–the ringing can be eliminated by a matching load. In our case, it was 225 Ω. In the experiments, the connecting wires had finite dimensions, i.e., inductances. To evaluate the inductances, we used an approximate expression for circular loop inductance,

$$L_{circle} = R\mu_0\left[\ln\left(\frac{8R}{a}\right) - 2\right] \tag{2.7}$$

where R is the radius of the loop, a is the radius of the wire, and μ_0 is the permeability of free space. In the experiments with the old pulser, the wires connecting the resistance formed a loop with ∼1 cm radius, while the wires connecting the actuator were longer and the corresponding radius was ∼5 cm. This corresponds to inductances of L_R=0.038 μH and L_R =0.294 μH. Substituting these numbers into the numerical code, the pulse reflection can be calculated. Calculations showed that at these values of inductances, there is almost no difference if a 250 Ω resistor is used as the matching impedance instead of the 225 Ω one. Therefore, in the experiments, a 250 Ω resistor was used due to its availability in the laboratory. Unfortunately, the reflection of the pulse from the pulser back to the actuator could not be calculated because of the complex structure of the pulser. Therefore, the numerical results are for single reflection only, whereas the experimental ones show all the ringing which takes place between the actuator and the pulser.

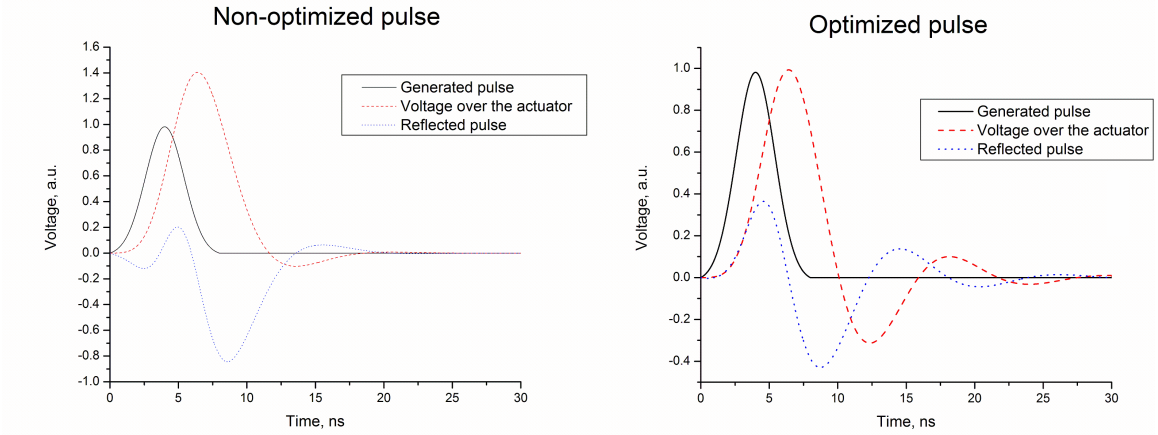

Figure 2.8: Numerical calculation of the nanosecond pulses. The plots show profiles of the pulse originally generated by the pulser, the voltage profile over the actuator, and the pulse reflected back into the cables. Left plot is for non-optimized load. Right plot is for optimized load with 250 non-inductive resistor. Adding the resistor decreases the ratio of the reflected pulse to the voltage on the actuator from 60% to 40%. These 40% are due to inductances of the connecting wires.

The voltage over the actuator and the reflected pulse is shown in Figure 2.8. By choosing the right resistance, we were able to reduce the ratio of the reflected pulse to the voltage over the actuator from 60% to 40%. The main reason for the 40% reflection is the inductance of the connecting wires. The measured pulse profiles before and after optimization are shown in Figure 2.9.

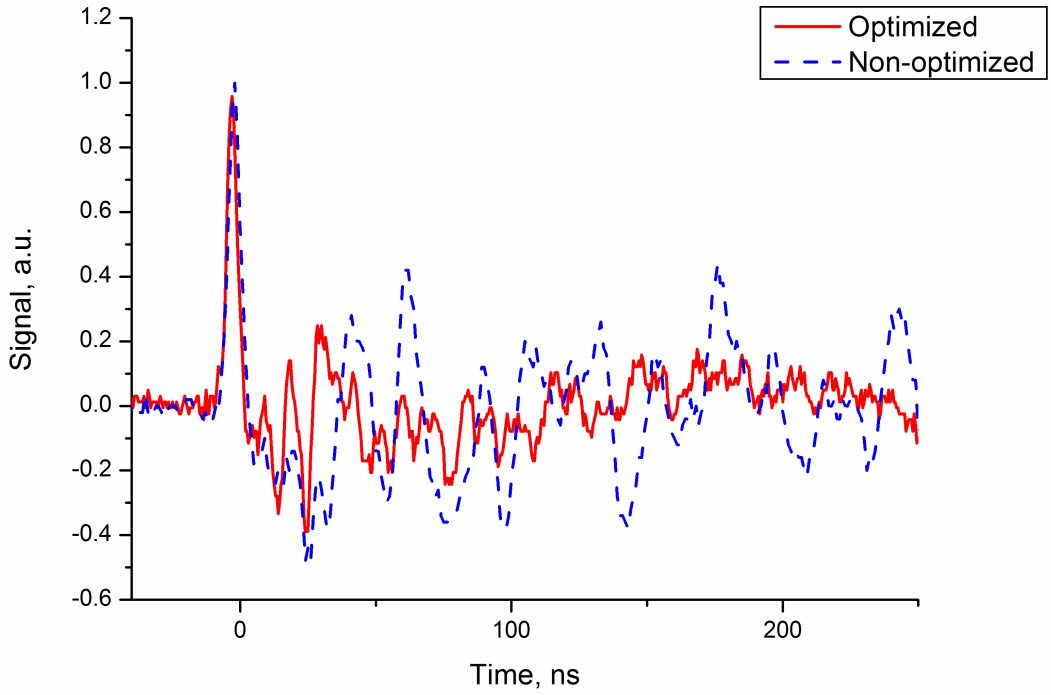

Figure 2.9: The measured pulse profile before and after optimization.

The numerical model also predicted that increasing the actuators capacitance leads to a lower peak voltage and to increased pulse duration. This result was verified experimentally and the same behavior was observed, as shown at Figure 2.10. Although the original pulses were 4 ns HWHM they became longer (∼5.5 ns HWHM) and lower in amplitude at the actuator due to its capacitance (∼27 pF, measured by Fluke 189 multimeter).

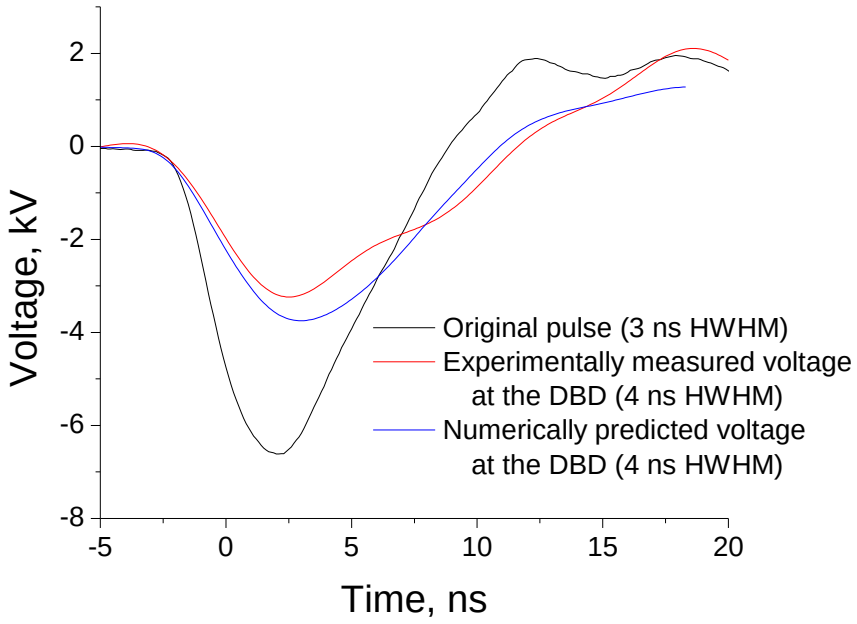

Figure 2.10: Ionization pulse profile from.

2.1.4 Bias voltage sources

Various bias voltage sources were used throughout the experiments. A source of constant bias voltage used in the schlieren experiments presented in Chapter 3 and surface charge measurements presented in Chapter 4 was High Voltage DC Supply model 412 by John Fluke MFG Co, Inc., capable of producing output voltages up to 2 kV dc both polarities. The sinusoidal bias voltage used in the schlieren experiments, Chapter 3, was produced by an ozone generator transformer by Plasma Technics, Inc. A Trek Model 20/20C HV Amplifier driven by a signal from Tenma 72-7210 function generator was used as a source of the alternating bias voltage in force balance testing, Chapter 5, and ozone visualization, Chapter 8, and as an ac voltage source in the surface charge experiments, Chapter 4.

Chapter 3

Schlieren Experiments

Experimental studies are conducted on a flow induced in initially quiescent room air by a single asymmetric dielectric barrier discharge driven by voltage waveforms consisting of repetitive nanosecond high-voltage pulses superimposed on dc or alternating sinusoidal or square-wave bias voltage. A new approach for non-intrusive diagnostics of plasma actuator induced flows in quiescent gas is proposed, consisting of three elements coupled together: the schlieren technique, burst mode of plasma actuator operation, and two-dimensional numerical fluid modeling. The force and heating rate calculated by a plasma model are used as inputs to a two-dimensional viscous flow solver to predict the time-dependent dielectric barrier discharge induced flow field. This approach allows prediction of the entire two-dimensional unsteady plasma induced flow pattern as well as the characteristics of the plasma induced force. Both the experiments and computations show the same vortex flow structures induced by the actuator. Parametric studies of the vortices at different bias voltages, pulse polarities, peak pulse voltages, and pulse repetition rates are conducted experimentally. The significance of charge buildup on the dielectric surface is demonstrated. The charge buildup decreases the effective electric field in the plasma and reduces the plasma actuator performance. The accumulated surface charge can be removed by

switching the bias polarity, which leads to a newly proposed voltage waveform consisting of high-voltage nanosecond repetitive pulses superimposed on a high-voltage low frequency sinusoidal voltage. Advantages of the new voltage waveform are demonstrated experimentally.

3.1 Introduction

Experiments reported in this chapter have demonstrated that the new voltage profile which consists of nanosecond pulses superimposed on a high-voltage low frequency sinusoidal bias voltage does indeed lead to higher performance.

To conduct experiments with DBD actuators one needs to develop reliable non-intrusive flow diagnostics. Difficulties for diagnostics of the actuator induced flow arise from its small approximately millimeter scale, low speed m/s, proximity to the plasma and the dielectric surface, and produced electro-magnetic noise. Most common techniques to diagnose the induced wall jet include particle image velocimetry, smoke visualization, hot wires, etc. Unfortunately, these methods are intrusive and must be used with great care.

For example, in particle image velocimetry measurements the particles may get charged in the plasma and may not only depict the flow incorrectly but may also affect the plasma and the gas flow, [36]. In [28] the flow field obtained with PIV showed streamlines which go into a solid wall. These facts demonstrate the unsuitability of PIV for visualization of DBD induced flows.

The main difficulty of Pitot-probe measurements is their low sensitivity. The measurements have to be taken at some distance downstream from the actuator in order not to perturb the plasma. Pitot measurements are also local, and to obtain the entire flow pattern, a scan through the entire flow region should be performed. The task becomes much more complicated with nonstationary flows.

Attempts to use nonintrusive optical methods were made in a number of works. A laser deflection technique was used to measure density by probing index of refraction gradients in the air, [37]. Being nonintrusive, this approach, however, gives only local measurements and, like the Pitot-probe one, is hard to apply to nonstationary flows.

The use of the schlieren technique for DBD induced flow measurements was reported earlier, [11, 38]. In the first paper, Leonov et al [11] used a conventional schlieren technique for flow visualization. The technique is based on following thermal disturbances in the jet and extracting the flow speed from that. However, the authors found this insufficient for quantitative speed measurements and used schlieren streak video instead. Another, similar, application of the schlieren technique to DBD plasma actuator was demonstrated by Sosa et al in [38]. Turbulent eddies were treated as tracers in the flow. A new, helium based technique of schlieren image processing was suggested to observe the flow field. In the region outside the turbulent flow a helium jet was injected in order to produce the necessary contrast. The helium jet, however, can disturb the plasma and the flow field. All of the above techniques are based on disturbances and/or turbulence in the induced flow. As noted in [38] the technique is not applicable for laminar flows.

In this work, we used a new approach for the induced flow visualization and velocity measurements. Since the discharge slightly heats the air, it is possible to visualize the induced wall jet. The principal feature of our schlieren technique, distinguishing it from other studies, is the modulation of the voltage waveform applied to the discharge so that the plasma actuator is operated in pulse-burst mode. In the burst mode, separate pulse jets are created by each burst. The advantage of this approach is the ability to visualize two-dimensional 2D, laminar, low speed, small, nonstationary plasma induced jets. An advantage of studies with quiescent air is that it is possible to observe some features of the induced flow which otherwise would be washed out

by an external flow. A numerical model based on the 2D Navier- Stokes equations predicts similar structures and allows us to extrapolate the entire flow pattern by matching the schlieren images of a single vortex. The numerical modeling also allows us to infer the magnitude of the body forces exerted by the DBD actuator on the gas.

As will be discussed in the chapter, the schlieren imaging in the pulse-burst mode demonstrated that the DBD actuator produces vortices. Note that similar structures have been observed in DBD experiments using smoke visualization, [39], with schlieren technique, [40], in DBD induced flow numerical simulations,[41, 42] and also in plane wall jet experiments and numerical simulations, [43, 44, 45]. However, in this work, we demonstrate that the strength of the vortices and frequency of their generation can be controlled by the voltage waveform, which has practical implications.

3.2 Experimental setup

DBD plasma actuator used for schlieren experiments consisted of two electrodes placed asymmetrically on either side of the dielectric, with one electrode encapsulated, and the other exposed to the atmospheric air, as shown in Figure 1.5. The electrodes were made of 100 μm thick copper foil. The width of the electrodes was equal to 25 mm and their spanwise dimension was 50 mm. A 100 μm thick kapton tape was used as the dielectric. The discharge was ignited by applying high voltage to one of the electrodes. The other electrode was grounded. The actuator was placed inside a sealed cylindrical aluminum chamber 45 cm high and 40 cm in diameter to eliminate the interaction between the plasma induced flow and air in the room. Side windows of 10 cm in diameter provided optical access to the actuator.

For the plasma actuator induced flow visualization we used a conventional schlieren system Figure 3.1, [46], which consisted of a mercury lamp, a 50 μm pinhole, and two lenses (FL=25 cm, D=6 cm). A vertical knife edge was located at the focus of the

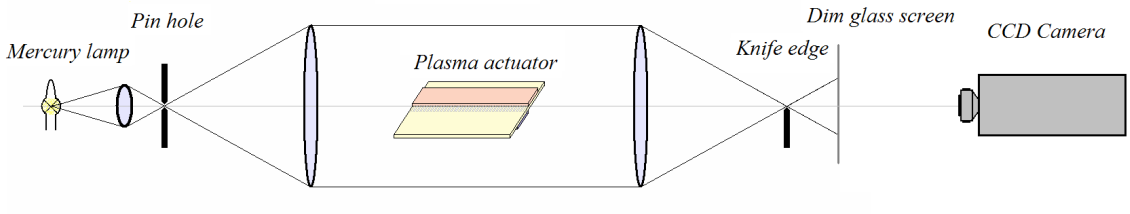

Figure 3.1: Schlieren system.

second lens. The image was projected on a ground glass screen and then captured by a Princeton Scientific Instruments 4-D charge coupled device camera. The camera took 28 consecutive images with 1 ms exposure time and no significant delay between the images.

3.3 Navier-Stokes code

The schlieren technique provides the coupling between the theoretical investigation of the plasma-gas interaction and the experiment. The plasma model predicts the heating rate and the force exerted on the gas. The output parameters from the plasma calculations can be then used as an input for the time-accurate numerical computational fluid dynamics CFD model based on 2D Navier-Stokes equations. The experiments showed, Figure 3.2, that the DBD actuator run in pulse-burst mode generates periodic wall jets which evolve into vortical structures. The numerical model predicts similar vortical structures and allows us to restore the entire flow pattern by matching the schlieren images of a single vortex.

A numerical code to simulate DBD induced flow at the experimental conditions was developed by Likhanskii, [47]. The 2D Navier–Stokes equations were solved

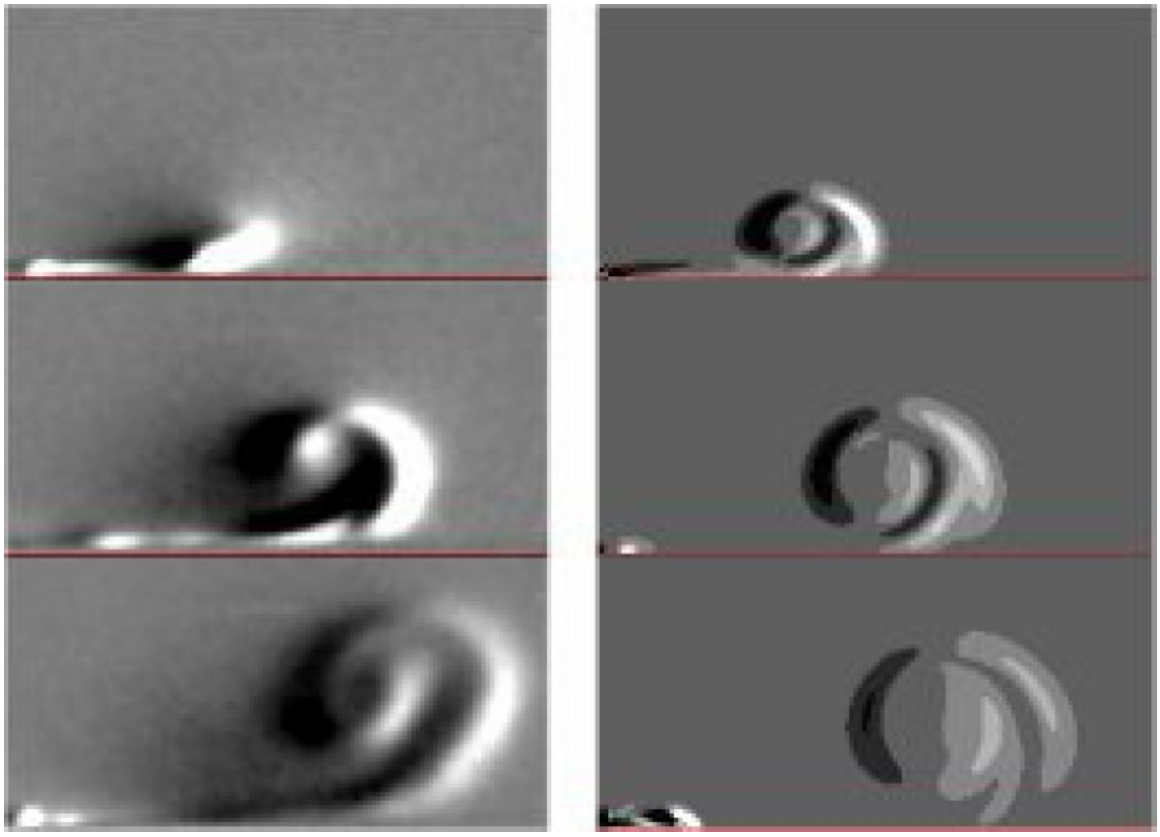

Figure 3.2: An example of experimental left and simulated right schlieren images of the DBD plasma jets. The images are 20 by 10 mm^2 each and correspond to 7, 14, and 21 ms after the burst start.

using second order accurate MacCormack scheme, [48]. The computational domain was 5×2 cm^2. The time step was determined by the Courant-Friedrichs-Lewy (CFL) condition. The modeling has been performed for quiescent air at initial temperature of 300 K. The gas constants have been taken from Anderson, [48]. The dielectric surface temperature 1 mm downstream from the exposed electrode was considered to be 350 K. The plasma region was assumed to be 100×500 μm^2. The force on the gas was considered to act only in horizontal direction downstream and to be uniformly distributed in the interaction region. In the simulations, the force magnitude and heating in the interaction region were varied.

3.4 Results

Consider the flow induced by the DBD plasma actuator in pulse-burst mode. When the DBD is on, the gas in the interaction region is being heated and receives momentum in the downstream direction from left to right. The motion of the gas generates a pressure gradient in the vicinity of the interaction region. The gas is being sucked in that region from the left and from above, creating an upstream vorticity. At the same time another vortex is generated by the induced gas jet as seen in Figure 3.3. There are important differences between the two vortices. One of them is the sign of vorticity. The vorticities of upstream and downstream vortices are negative and positive, respectively. Another principal difference is the gas density in these vortices. The upstream vortex involves motion of the quiescent air at room temperature, thus its temperature is constant. In contrast, the downstream vortex is generated due to the motion of heated gas jet. Thus, it is characterized by well-defined temperature and density profiles. In the schlieren experiments on DBD induced flow, only density gradients can be visualized, i.e., the downstream vortex is observed and the upstream one is not detected.

These results can be important in theoretical investigations of the flow separation control using DBD: the gas flow will interact not only with the observed downstream vortex but also with the hidden upstream one. Representative examples of such vortical structures, both experimental and reproduced in the numerical modeling, are shown in Figure 3.2. By comparing the experimental and computational results, it was thus possible to reconstruct the entire evolving flow pattern and to infer both the induced velocity field and the magnitude of plasma induced body force. For this example the motion of the vortex was around 0.5 m/s 17 mm downstream and that was driven by a surface jet with a velocity of 7 m/s in the plasma vicinity.

Likhanskii et al, [49, 50, 51, 47], calculated the integral momentum transferred to

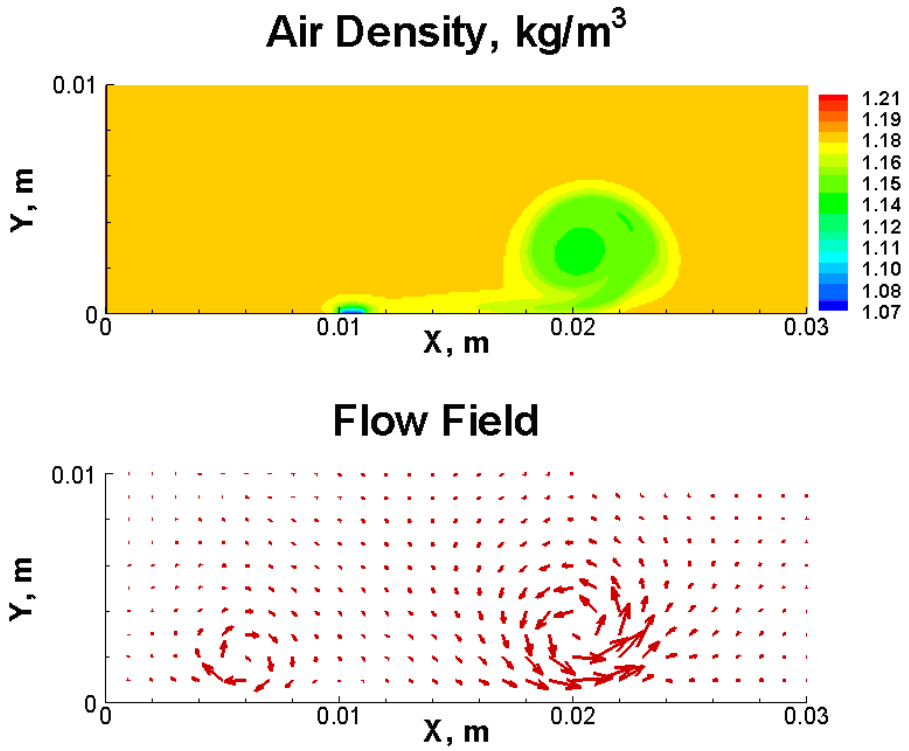

Figure 3.3: Air density and velocity distribution 14 ms after the burst.

the gas by means of positive and negative nanosecond pulses with dc bias, as well as the heating rate in the interaction region. We have now extracted that data and used it as an input to the Navier–Stokes solver. An important assumption in the modeling was that there are no saturation effects due to surface charging. The pulser was considered to operate at 500 kHz repetition rate. The computed vortex propagation velocity as a function of distance from the exposed electrode is shown in Figure 3.4. Taking the results for momentum transfer from [50, 51] for positive 3 kV pulses 4 ns FWHM with 1 kV dc bias and distributing it equally in he interaction region, we get the force in that region, 1.4×10^5 N/m^3. The numerical results for this calculation are

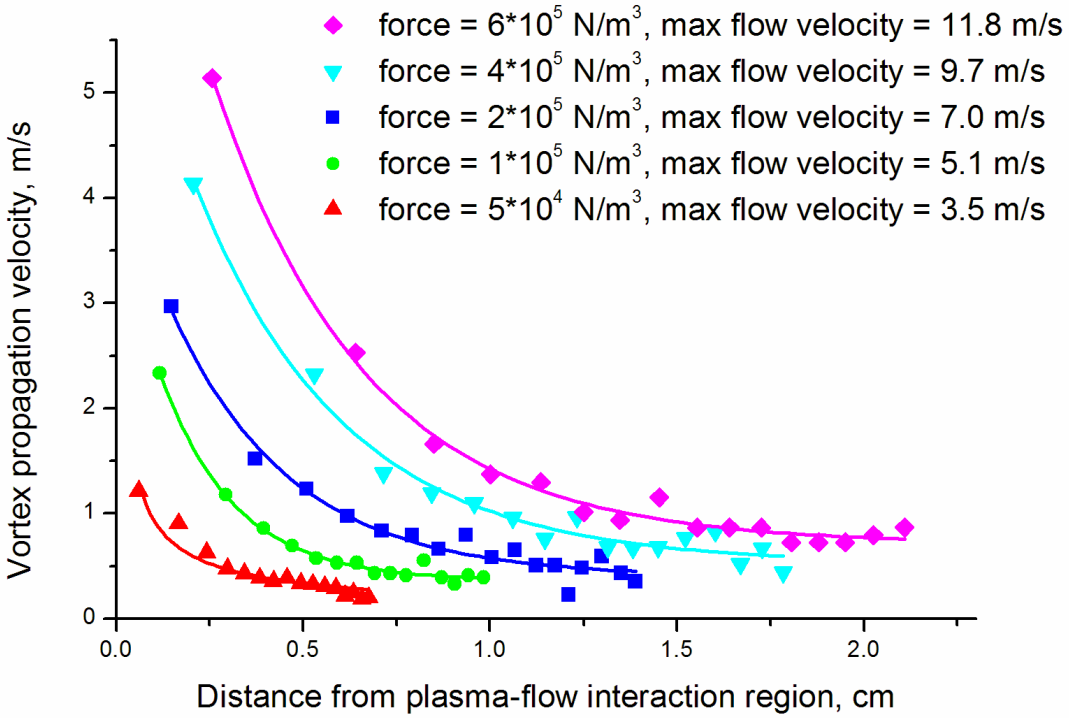

Figure 3.4: Vortex propagation velocity as a function of the distance from DBD at different forces in the interaction region. The maximum velocities of the induced flow at the vicinity of interaction region are designated as max flow velocities".

between the green round and blue square data points in Figure 3.4. The other curves correspond to the different force magnitudes in the interaction region at constant heating rate. It can be clearly seen that the translational vortex velocity significantly drops with the propagation along the surface. This fact is very important, since using the schlieren technique in the experiments we can extract the density gradients at several temporal points and thus determine the vortex propagation speed. The developed model thus allows inferring the induced flow velocity right at the edge of the plasma and the force magnitude in the interaction region by matching the

experimental pictures with numerically obtained ones. The effect of heating was also investigated; however, the results showed that the vortex size has almost no dependence on the heating in the interaction region. Only the temperature of the gas within the vortex varies. Note that the gas temperature cannot be measured by the schlieren technique, and additional measurements with other techniques should be used to provide an additional insight into the plasma-flow interaction.

In the experiment the pulser was run in burst mode at 50 kHz PRR and 50% duty cycle, giving 10 ms bursts with 500 pulses in each burst every 20 ms. The pulse voltage was 5 kV. In addition 2 kV bias voltage was applied to the electrodes.

To examine experimentally how the actuator induced flow speed depends on the constant bias voltage, we ran experiments with fixed pulse voltage and different bias voltages, as shown in Figure 3.5. The vortex translational speed versus downstream coordinate at different bias voltages is shown in Figure 3.6 for both polarities of the pulses. The experiments showed that in the case of negative pulses there is only a weak, within the error bars, dependence of the induced flow velocity on the bias voltage. Bias voltage of either polarity increased the induced jet speed only slightly. For the positive pulses, there was no clear dependence on the bias voltage. These results did not agree with the expectations based on the numerical plasma model that predicted significant increase in the induced flow velocity with the bias voltage.

However, during the experiment, an interesting phenomenon was noticed: a rapid switch of the bias polarity increased the jet velocity for the first several pulse bursts. To observe the details of the first vortices after the bias switch, the camera was triggered at the very beginning of every run so that it captured the first bursts. The actuator was thus run at some value of the bias voltage for 5 s, and then the pulses were turned off. After 10 s off, the pulses were turned on again, and the first two bursts of this second run was captured. This second run was done at either the same

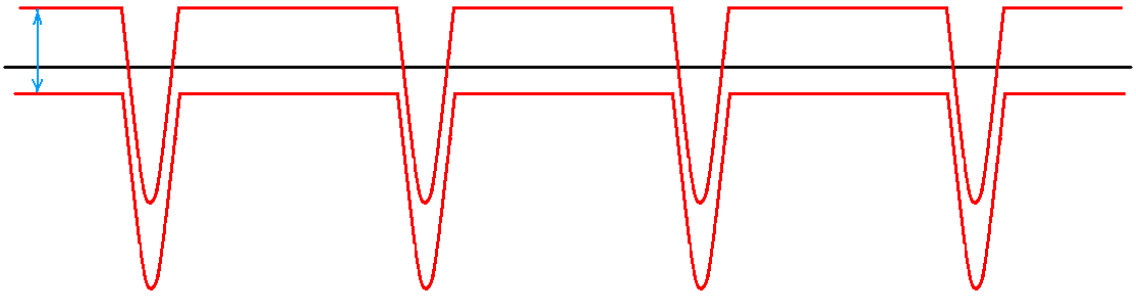

Figure 3.5: Varying the bias voltage in constant bias experiments. The pulse voltage is unchanged, thus change in bias voltage leads to the same change in the peak voltage.

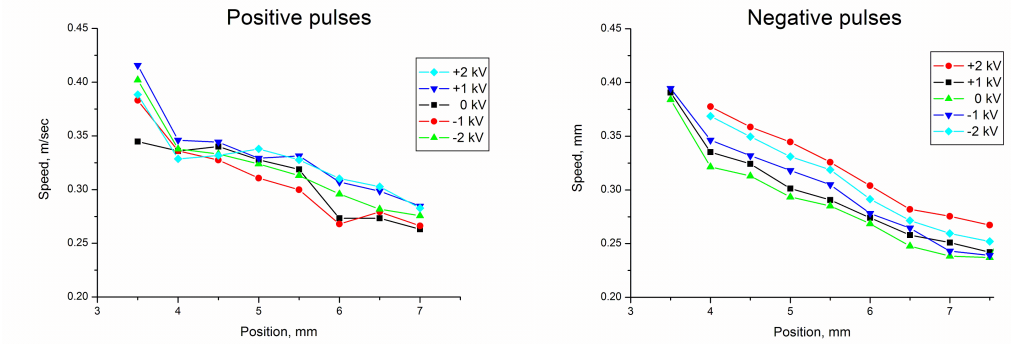

Figure 3.6: The induced flow speed vs distance at different constant bias voltages. The error bar is 0.04 m/s.

or a different value of the bias voltage compared to the first run. As in the previous experiments, the pulser was run in burst mode at 50 kHz PRR and 50% duty cycle, giving 10 ms bursts with 500 pulses in each burst every 20 ms. The pulse voltage was 5 kV, and the bias voltage was changed from -2 to +2 kV. The results are presented in Figure 3.7.

Columns represent images taken 7, 14, and 21 ms after the burst started. Different rows represent different biases. The electrode arrangement is indicated. The results show that switching the polarity of the bias voltage has a dramatic effect on the DBD operation: much faster jets and vortices are generated compared to the constant bias

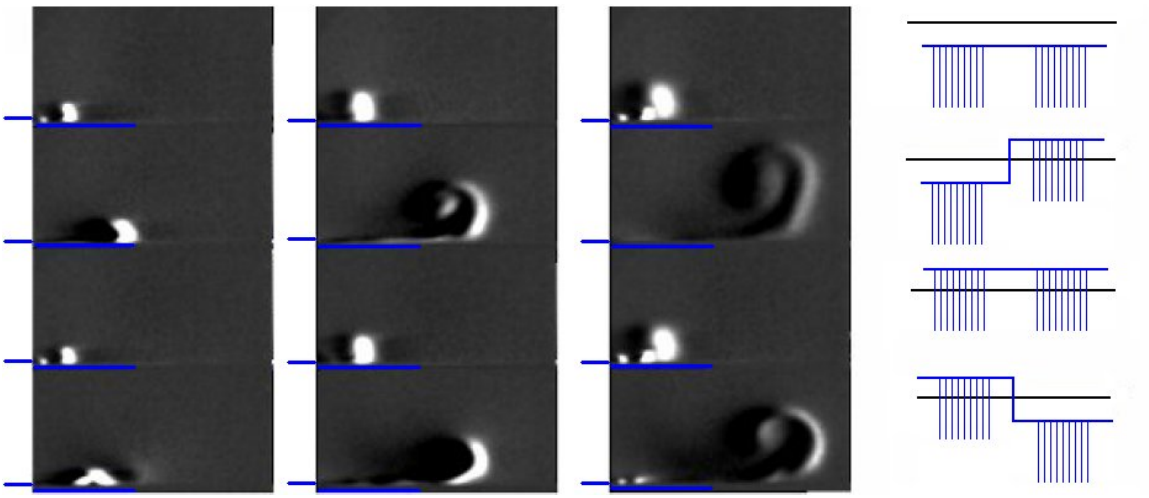

Figure 3.7: Bias voltage switch experiments. The columns represent images taken 7, 14, and 21 ms after the burst started. The bias and pulse polarities are indicated. The results are presented for 5 kV negative pulses, 50 kHz, 50% duty cycle. The bias voltage was +/2 kV. The view field is 20 by 10 mm^2.

cases. An interesting feature can also be observed when switching from positive to negative bias with negative pulses. The induced wall jet from the first burst moves off the surface and then returns back, what looks like a jump. The jet created by the following (second after the bias switch) burst, however, does not jump anymore. The location of the jump is around the region where the plasma ends. In the case of positive pulses, a similar jump can be observed when switching from negative to positive bias voltage. In addition, in that case the second vortex also jumps. The same behavior was observed during switches from 2 to 0, 0 to 2, 0 to +2, and +2 to 0 kV for both polarities of the pulses. However, the jet velocity increase and the jump were not as strong as in the cases of switching between negative and positive polarities of the bias voltage. A likely explanation for the observed behavior is accumulation of surface charge on the dielectric. During the run, the dielectric surface is charged, and shielding of the applied bias electric field occurs, reducing the force on the gas and the jet velocity. This explains why in the first series of experiments the effect was

determined by the difference between the peak voltage and the bias voltage and not so much by the peak voltage or the bias voltage separately. Switching the polarity of the bias removes the surface charge and enhances the actuator performance for a short time, until the surface charge builds up again. One reason for the jump behavior could be an interaction of residual space charge with the surface charge. More studies on this subject were done and are presented in Chapter 4.

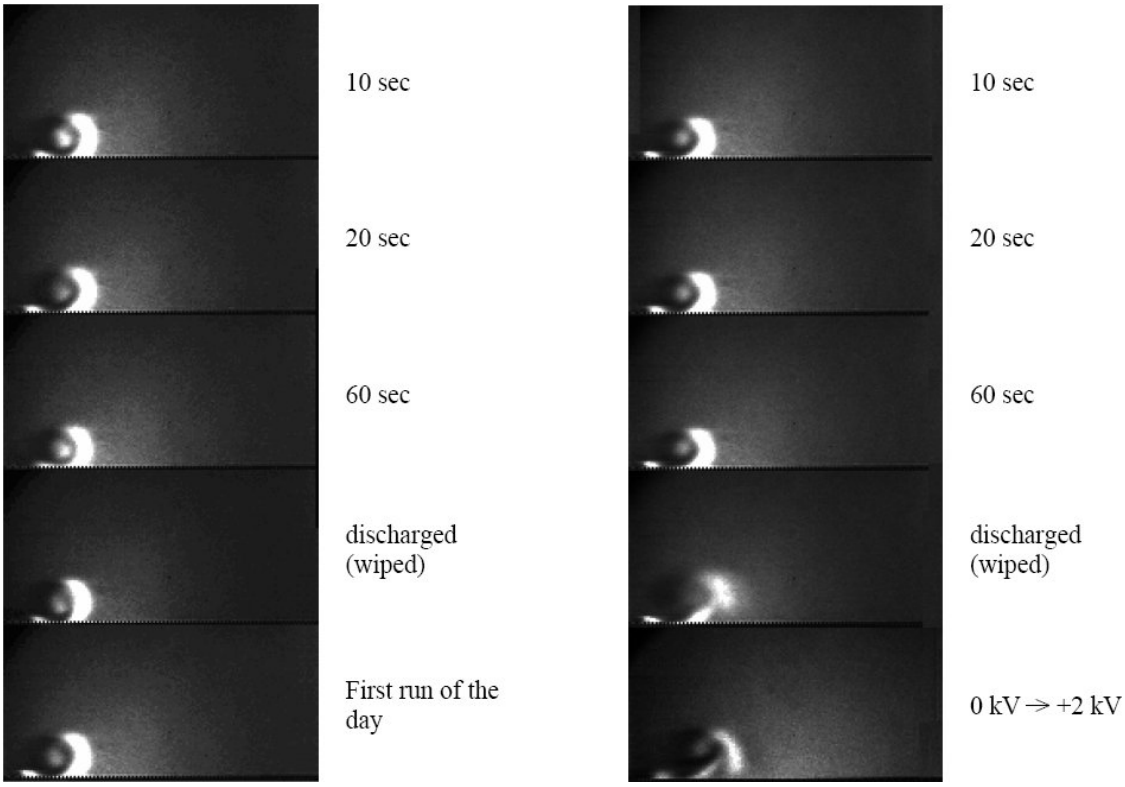

Figure 3.8: Surface wipe experiments. The experiments were done for 0 kV left column and +2 kV right column bias voltages with 5 kV, 50 kHz, 50% duty cycle positive pulses and time delays of 10, 20, and 60 s. Wiped runs were done with 10 s time delay during which the charge was removed from the surface by a grounded wet cloth. The last picture in the left column shows the very first run of the day, when the surface was still charge-free. The last picture in the right column shows a bias switch experiment in which the bias voltage was changed from 0 to +2 kV. The images were taken 12 ms after the burst start. The field of view of each image is 20 by 10 mm^2.

To check if there really is a surface charge accumulated on the dielectric, the next set of experiments was conducted. The conditions were similar to the previous experiments. First the actuator was run for 5 s. Then after some time being off it was run again without switching the bias voltage. The first burst of the second run was captured. The aim was to see how the generated vortex depends on the time delay between the runs. The experiments were done for 2, 0, and +2 kV bias voltages with 5 kV, 50 kHz, 50% duty cycle positive pulses and time delays of 10, 20, and 60 s. Another run was done with 10 s time delay during which the charge was removed from the surface. The surface charge removal was done with a wet grounded cloth. The water provided a good contact with the entire surface, and after a wipe the surface was slightly wet and quickly dried out by itself. The whole procedure took less then 10 s at the end of which the surface was dry and discharged. Wiping the surface with a dry cloth to remove the water might lead to the surface charging through friction. The results are presented in Figure 3.8. It is seen that the vortex-generating performance persists for the times up to 1 minute. If the observed behavior was due to some heating effects, there would not have been such a long hysteresis as 1 minute. This provides evidence in favor of the surface charge. Also the wiped-surface runs with bias look like a switch from zero bias voltage. This shows that the effect does occur due to the surface charge which depends on the bias voltage. It can be seen that the vortex is very similar to the one from the wiped-surface run, which means that both the wipe and the run at kV bias voltage discharge the surface. Again, it can be seen that the surface charge shields the applied bias voltage. However, if the surface charge is removed, the plasma feels the bias voltage, but only until the new charge builds up on the dielectric surface. It was not possible to conduct similar experiments with the negative pulses. As mentioned above, the bias voltage was applied to the same electrode as the pulses, i.e., for the negative pulses that would be the exposed

electrode. Manually wiping the surface to remove the charge in the close vicinity of the electrode at a few kilovolts potential would be unsafe.

Since the jet-enhancement effect disappears as soon as the charge builds up on the dielectric and shields the bias field, to let the effect go on continuously, one needs to keep switching the bias. Thus, a new voltage waveform was used in the subsequent experiments: high-voltage sinusoidal signal 2.6 kV peak to peak, 60 Hz plus nanosecond pulses 50 kHz, 5 kV, positive or negative. Three versions of the voltage waveform were examined:

- 100% duty cycle pulses + sinusoidal bias voltage,
- 50% duty cycle pulses, bursts near the peaks of the sinusoidal voltage + sinusoidal bias voltage,
- 50% duty cycle pulses, bursts at the slopes of the sinusoidal voltage + sinusoidal bias voltage,
- 50% duty cycle pulses with no bias

Since this set of experiments involved 60 Hz sinusoidal signal, a new modulation of the pulses had to be used. The pulses were generated in bursts with 208 pulses per burst and 120 bursts per second. The results are presented in Figure 3.9. From the experimental results we can see that the sinusoidal bias significantly improves the actuator performance. The jet speed increases from 30 cm/s near the discharge in case d) to 80 cm/s at 10 mm downstream in the case a). Thus, even a relatively low bias voltage 1.3 kV compared to 5 kV pulses has a great effect on the DBD actuator operation. Note that the bias voltage itself could not ignite the plasma in the absence of the pulses. Also, vortices are still observed in case a) despite the fact that the pulses are on all the time. This means that the induced wall jet speed strongly depends on

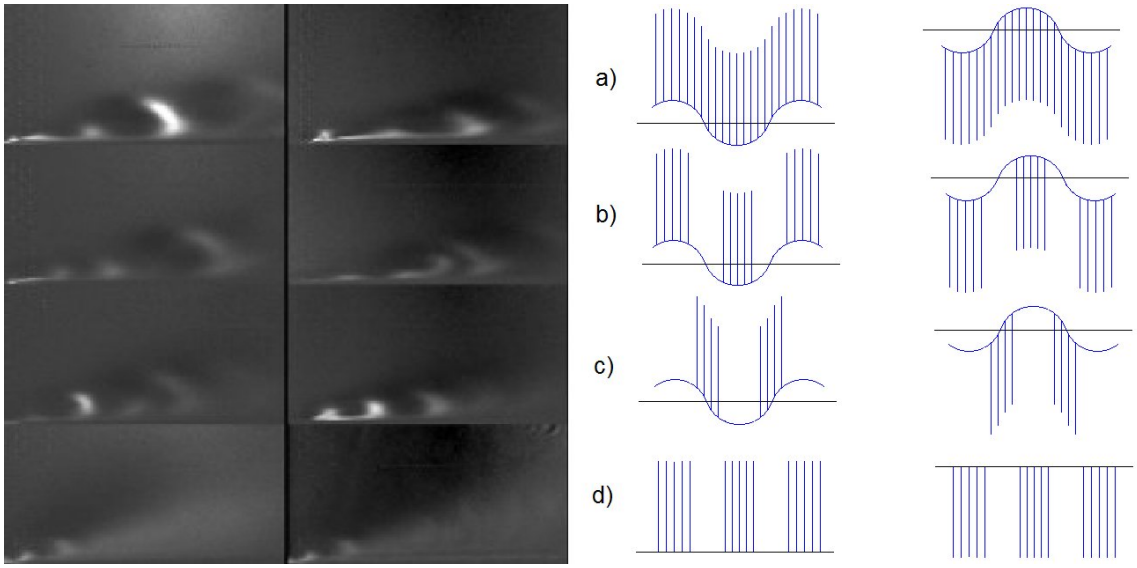

Figure 3.9: Nanosecond pulses combined with sinusoidal bias voltage. 5 kV, 50 kHz positive left column and negative right column pulses combined with 2.6 kV peak-to-peak 60 Hz sinusoidal bias voltage. The field of view of each image is 20 by 10 mm^2.

instantaneous bias voltage as well as on the surface charge on the dielectric. In addition, bursts at different bias voltages, are different. The vortex speed and size depend on whether it was generated during positive/negative bias/slope of the bias voltage.

For further investigation we selected a voltage waveform with pulses near the peaks of the bias voltage, since this waveform was more effective than the one with the pulse bursts at the bias voltage slopes. Additionally, with this waveform, it can be determined unambiguously which burst the vortex came from, which makes the data easier to interpret.

As a baseline voltage waveform, we chose 5 kV pulses at 50 kHz and 50% duty cycle near the peaks of a 10 kV peak-to-peak 60 Hz sinusoidal bias voltage. Then varying one of the parameters at a time, the bias voltage, pulse voltage, and repetition rate, we observed the vortices for each polarity of the pulses. As mentioned above,

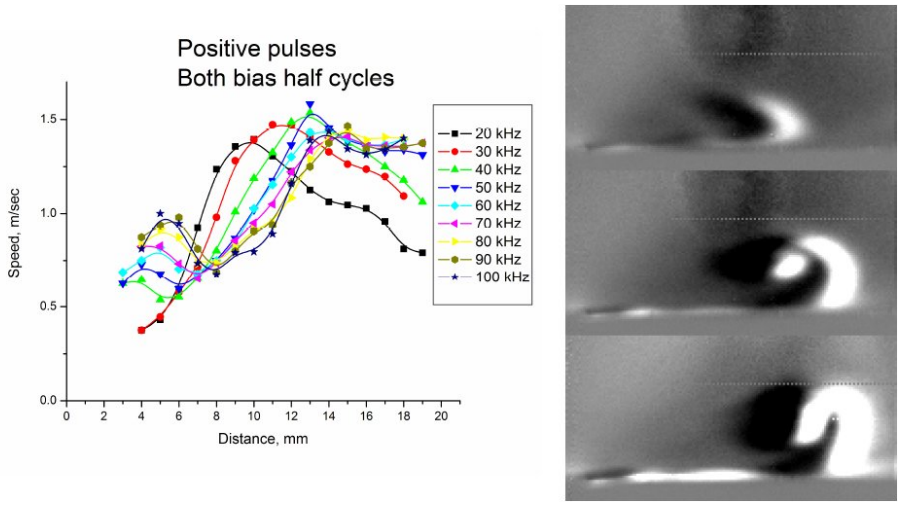

Figure 3.10: Vortex speed vs distance for different PRRs with positive polarity of the pulses. The schlieren images were taken at the same moment of time for 20, 50, and 100 kHz. A slow vortex is created by a jet from positive bias half-cycle, then from 5–7 mm it is accelerated by a jet from the negative bias half-cycle burst. The field of view of each schlieren image is 20 by 10 mm^2.

the vortices coming out of different bias half-cycles differ in speed and size. Thus plots for both kinds of vortices are presented in the figures when possible.

Consider, first, the actuator performance dependence on pulse repetition rate (PRR) for positive pulses Figure 3.10. The vortex coming out of the positive bias half-cycle is slow. It has not moved far away from the plasma region by the time the next vortex appears. The next vortex, which comes out of the negative bias have-cycle, is very fast. It actually does not evolve into a vortex immediately; it is still in its jet phase and thus is hard to notice. Then, upon collision with the earlier generated slow vortex, it also becomes a vortex. Thus, actually there is only one vortex in the schlieren image at a time. As seen in Figure 3.10, there is rather weak dependence on the PRR.

The dependence of vortex parameters on PRR for negative pulses Figure 3.11 is different. The vortices created during the negative bias half-cycles consist of two

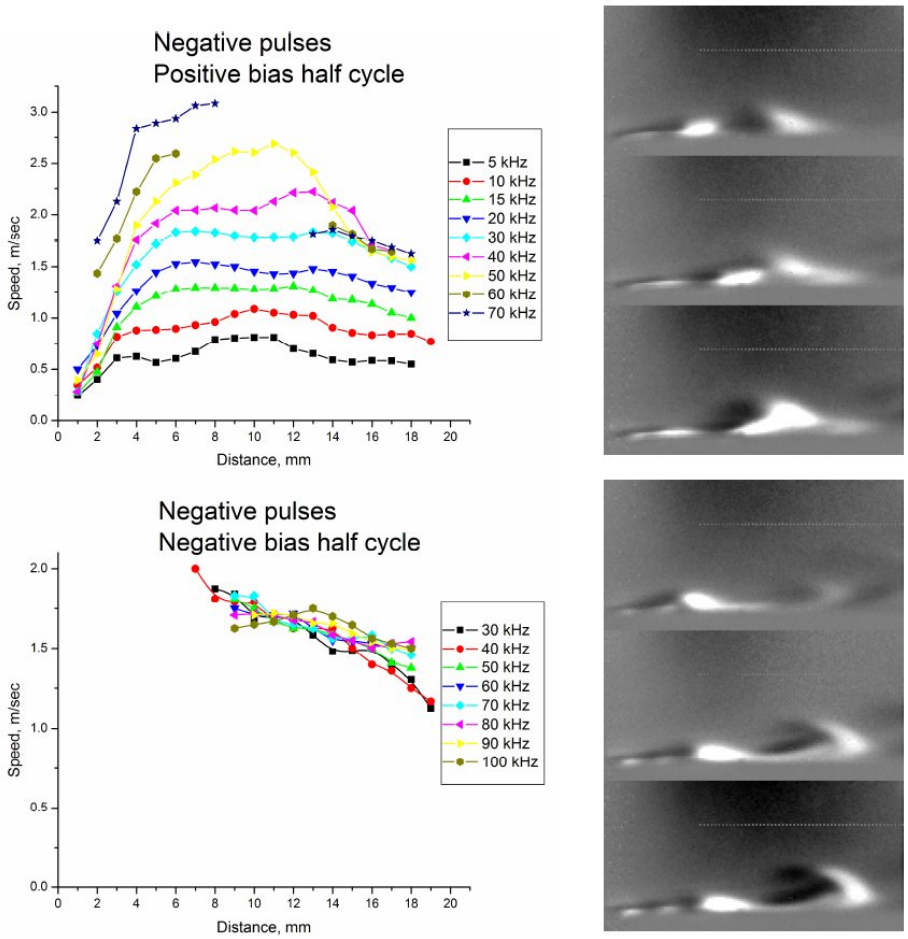

Figure 3.11: Vortex speed vs distance for different PRRs with negative polarity of the pulses. The schlieren images were taken at the same moment of time for 30, 50, and 70 kHz. In the bottom images, a vortex from the negative bias half-cycle is shown. The vortex consists of two parts: head vortex and tail vortex. In the top image, jet from positive bias half-cycle hitting the tail part of the negative vortex is shown. The speed of the positive vortex greatly depends on the PRR, while the speed of the negative one does not. The field of view of each schlieren image is 20 by 10 mm^2.

parts. The head part is not observed for pulses repetition rate lower than 30 kHz. Its speed is relatively high and does not depend on the PRR. The tail part is brighter and much slower. The vortex created during positive bias half-cycle is faster. Its speed strongly depends on the PRR, as seen in Figure 3.11.

The next parameter varied in the experiments was the pulse voltage. The results

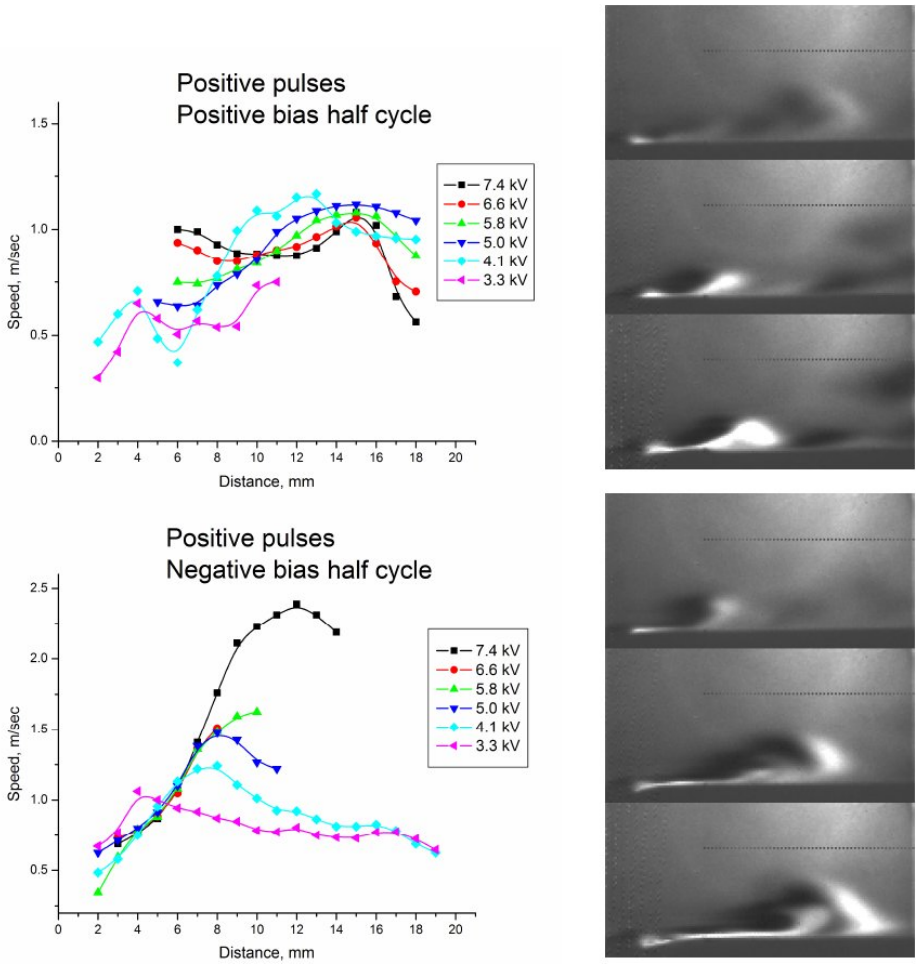

Figure 3.12: Vortex speed vs distance for different pulse voltages with positive polarity of the pulses. The schlieren images were taken at the same moment of time for 3.3, 5.0, and 7.4 kV. In the top images, slow jet from positive bias half-cycle is shown. In the bottom images, a vortex from the negative bias half-cycle is shown. The speed of this vortex is high and depends strongly on the pulse voltage. In the pictures for 5.0 and 7.4 kV, this vortex is colliding with the positive one. The field of view of each schlieren image is 20 by 10 mm^2.

for the positive pulses are presented in Figure 3.12. The speed of positive i.e., generated during the positive half-cycle of the bias voltage vortices weakly depends on the pulse voltage. However, their brightness temperature strongly depends on the pulse voltage. The pulse voltage has a dramatic effect on the speed of negative i.e., generated during the negative half-cycle of the bias voltage vortices.

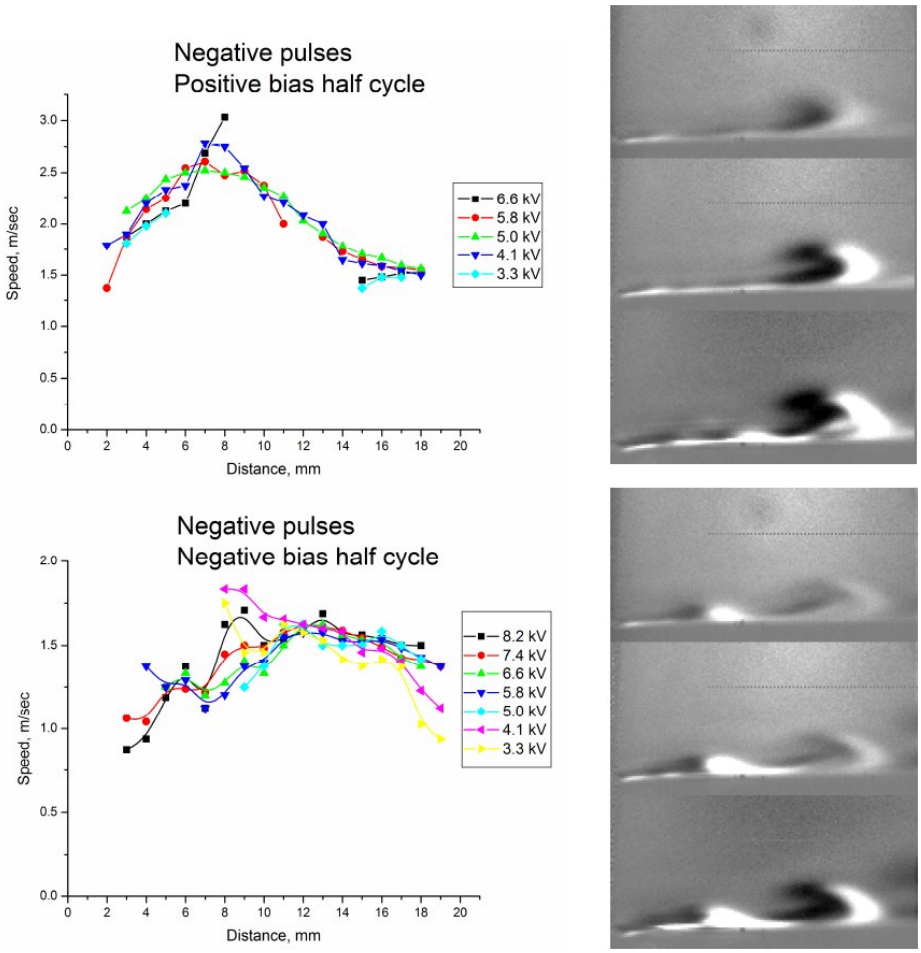

Figure 3.13: Vortex speed vs distance for different pulse voltages with negative polarity of the pulses. The schlieren images were taken at the same moment of time for 3.3, 5.0, and 7.4 kV. In the top images, jet from positive bias half-cycle is shown. In the bottom images, a jet from the negative bias half-cycle is shown, consisting of two parts: head vortex and tail vortex. There is no dependence of the speed of the vortices on the pulse voltage. The field of view of each schlieren image is 20 by 10 mm^2.

For the negative polarity of the pulses, the vortex speed is quite high, and the only effect of the higher pulse voltage is stronger heating. The details are shown in Figure 3.13.

Among all the parameters, the sinusoidal bias voltage has perhaps the strongest influence on the DBD plasma actuator operation. The results for the positive pulses

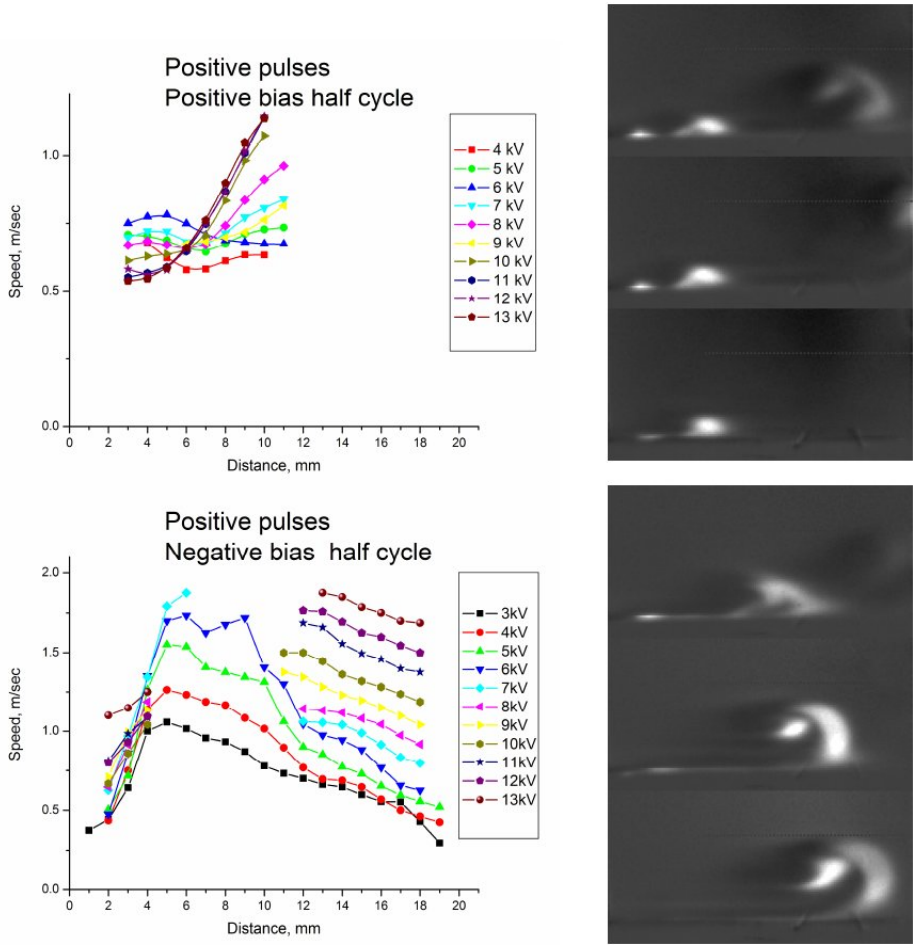

Figure 3.14: Vortex speed vs distance for different peak-to-peak sinusoidal bias voltages with positive polarity of the pulses. The schlieren images were taken at the same moment of time for 5, 10, and 13 kV. In the top images, a slow jet from positive bias half-cycle is shown; when a strong jet from the negative half-cycle arrives, it pushes the positive jet forward, which explains the acceleration in 6-11 mm range. In the bottom images, a vortex from the negative bias half-cycle is shown. Its speed is high and strongly depends on the pulse voltage. In the pictures for 5.0 kV, the collision is still in progress, which explains the complex shape of the vortex. The field of view of each schlieren image is 20 by 10 mm^2.

are presented in Figure 3.14. Again, positive vortices are rather slow, and it is unclear if changing the bias voltage has any effect on them because they propagate only several millimeters before the vortices from the negative bias half-cycles hit them from behind. The speed of vortices from the negative half-cycles depends strongly on

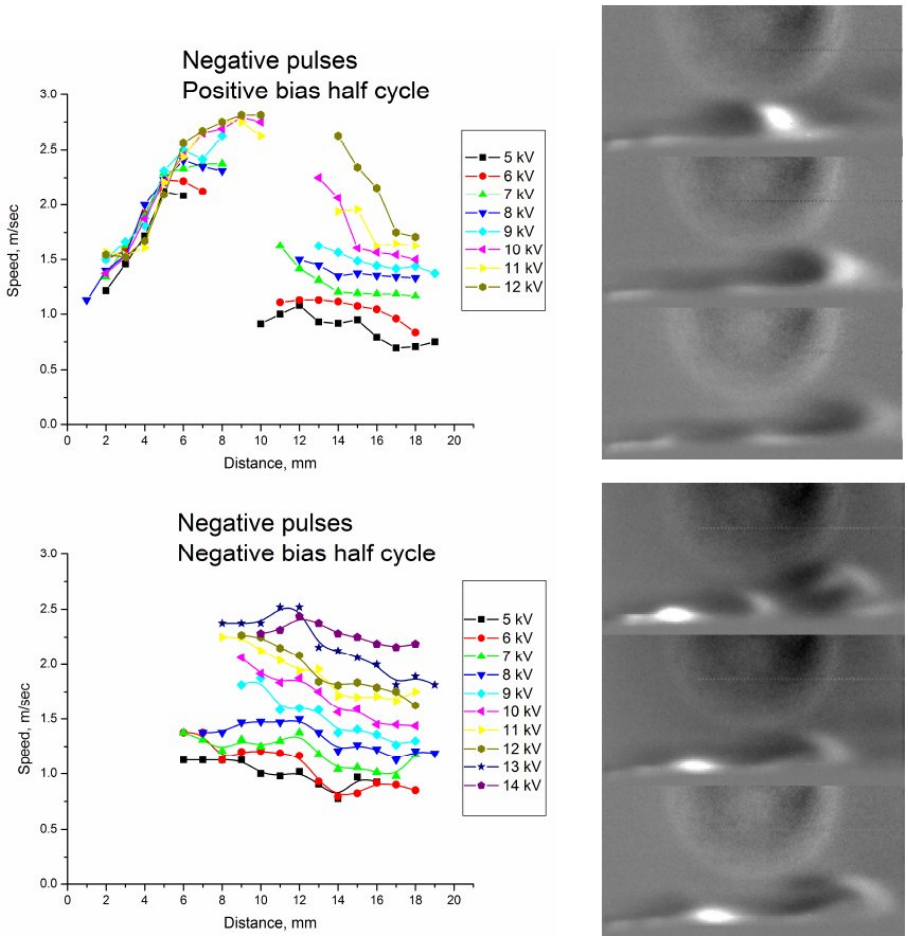

Figure 3.15: Vortex speed vs distance for different peak-to-peak sinusoidal bias voltages with negative polarity of the pulses. The schlieren images were taken at the same moment of time for 5, 10, and 13 kV. In the top images, jet from positive bias half-cycle is shown. The vortex speed strongly depends on the negative pulse voltage. The field of view of each schlieren image is 20 by 10 mm^2. The circle in the images is due to water condensation in the camera.

the bias voltage.

For negative pulses, the increase in bias voltage leads to a significant increase in effect in both half-cycles of the bias voltage. The results are presented in Figure 3.15.

Starting from 5 kV peak-to-peak bias voltage, self-sustained discharge was ignited in the absence of the high voltage pulses. This discharge could remove the surface charge by itself. Since positive pulses create a strong force on the gas only during

the negative bias half-cycle, it was interesting to check if it is still important to have pulse bursts during the positive half-cycle of the bias. Thus experiments were run with the pulses during half-cycles of one polarity only. The voltage waveforms are shown in Figure 3.16.

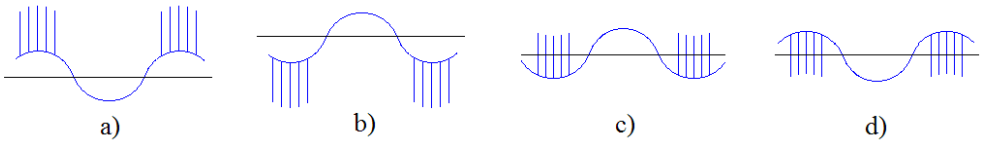

Figure 3.16: Voltage profiles with pulses near the bias voltage peaks of one polarity only.

The results of the experiments are shown in Figure 3.17. It can be seen that in the absence of the pulse burst during the other half-cycle, the induced wall jet speed becomes two to three times lower in all cases. This means that although some of the pulse bursts do not create a strong wall jet, they still play an important role in the DBD operation. Their task is to discharge/recharge the dielectric surface and thus to increase the efficiency of the other bursts. The experiments also clearly show that the wall jets induced by negative pulses evolve into two-vortex formations, whereas the ones from the positive pulses do not. The mechanism of this behavior should be investigated in future studies.

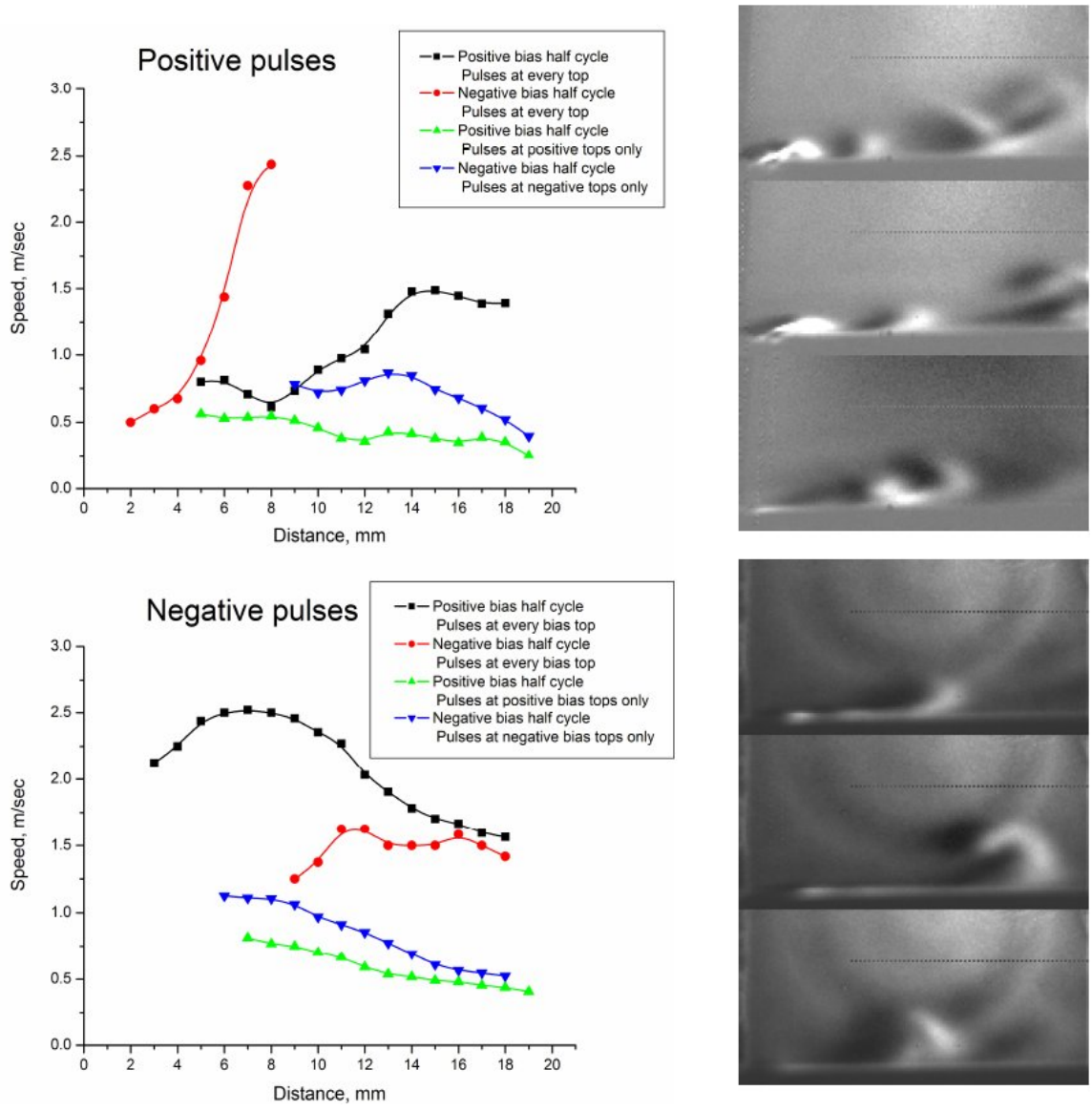

Figure 3.17: Vortex speed vs distance for different voltage waveforms, see Fig. 20. The schlieren images were taken at the same moment of time for pulses during negative half-cycle only, both half-cycles, and positive half-cycle only. The field of view of each schlieren image is 20 by 10 mm^2.

3.5 Summary

We have used a burst mode of plasma actuator operation in conjunction with non-intrusive schlieren diagnostic of the actuator induced flows in quiescent gas. With

this technique, the DBD actuator was observed to generate periodic pulsed wall jets that evolve into vortices. Parametric studies of the vortex speed and size versus parameters of the waveform pulses in repetitive-burst mode plus dc or ac bias voltage were performed. Matching 2D numerical fluid modeling to the experimental results allowed us to infer the magnitude of plasma-generated body force exerted on the gas. The knowledge of the body force magnitude can then be used to compute the entire flow field in both burst and continuous modes of plasma actuator operation.

The experiments showed that although repetitive short pulses do efficiently generate the plasma, a dc bias voltage cannot push the gas efficiently because the charge buildup on the dielectric surface shields the applied dc electric field. To remove the surface charge, periodic switching of the bias voltage polarity is required. Thus, we proposed a new voltage waveform, consisting of high-voltage nanosecond repetitive pulses superimposed on a high-voltage low frequency sinusoidal or square-wave bias voltage. The advantages of the new voltage waveform in significantly enhancing the wall lets and the vortices have been demonstrated experimentally.

Note that in conventional DBD actuators driven by sinusoidal voltages, ionizing pulses streamer breakdowns also occur, but the magnitude and frequency of those ionizing pulses depend entirely on the parameters of the sinusoidal driving voltage. In contrast, we proposed and used what is essentially non-self-sustained discharge: the plasma is generated by repetitive short pulses, and the pushing of the gas occurs primarily due to the low frequency bias voltage. The advantage of this non-self-sustained discharge is that the parameters of ionizing pulses and the driving bias voltage can be varied independently, which adds flexibility to control and optimization of the actuator performance.

Chapter 4

Surface Charge in DBD Plasma Actuators

Schlieren experiments presented in Chapter 3 reveal a significant charge build up at the dielectric surface which have a big impact on the DBD plasma actuator performance. It appears that the surface charge shields the applied bias voltage that otherwise pushes the gas. To verify this hypothesis direct measurements of the dielectric surface potential, its distribution and dynamics are required.

This Chapter presents results of the direct measurements of the dielectric surface potential and its dynamics in asymmetric dielectric barrier discharge (DBD) plasma actuators. It is shown that the charge builds up at the dielectric surface and extends far downstream of the plasma. The surface charge persists for a long time (tens of minutes) after the driving voltage has been turned off. For a sinusoidal voltage waveform, the dielectric surface charges positively. With the voltage waveform consisting of nanosecond pulses superimposed on a dc bias, the sign of the dielectric surface charge is the same as the sign (polarity) of the bias voltage. A simplified numerical model showed a good agreement with the experimental data. This confirms that the surface charge is deposited by the ions which drift from the plasma region to the

dielectric surface in the applied bias field. The surface charging significantly affects DBD plasma actuator performance.

4.1 Introduction

It is understood that electric charge deposition on the dielectric surface limits the current and thus allows operation of nonequilibrium discharges at atmospheric pressure. The important role of the surface charge and its finite relaxation time (the "memory voltage") in the discharge physics was pointed out by Massines et al, [52], and Gadri , [53], for the parallel plate DBD configuration, and by Roth et al., [54] for One Atmosphere Uniform Glow Discharge Plasma (OAUGDP). Since the surface charge plays an important role in DBD physics, it warrants a special study. In the work of Font et al., [55], the surface potential in a DBD driven by sinusoidal voltage was measured using a V-dot probe technique, and the voltage across the plasma was shown to be less than half of that which is applied across the electrodes. Recently the same group, [56] presented the time evolution and the spatial extent of the surface potential. In this Chapter, we describe electrostatic voltmeter measurements of surface charge in DBD plasma actuators driven by various voltage profiles, most notably by pulses plus dc bias but also by sinusoidal voltages. The results for the sinusoidal profile recently reported by Enloe et al., [56] are consistent with our results. For sinusoidal voltages the two approaches are mutually complementary since Enloe et al. measured the surface potential using a different method.

4.2 Electrostatic voltmeter

For non-intrusive surface potential measurements we used the Trek Model 247-3 Electrostatic Voltmeter with Trek Model 6000B-13C Electrostatic Voltmeter Probe, Fig-

ure 4.1. The probe has high resolution around 1 mm, fast response time less than 3 ms for a 1 kV step, and an operating range from 0 to 3 kV dc or peak ac.

A test run was done to verify the probe's spacial resolution. To do that 1 kV dc voltage was applied to the actuator's top electrode, the encapsulated electrode was grounded. Such configuration gives a step-function-like distribution of potential along the surface. The result of testing is shown at Figure 4.1. It shows that the resolution of the given probe is around 1 mm.

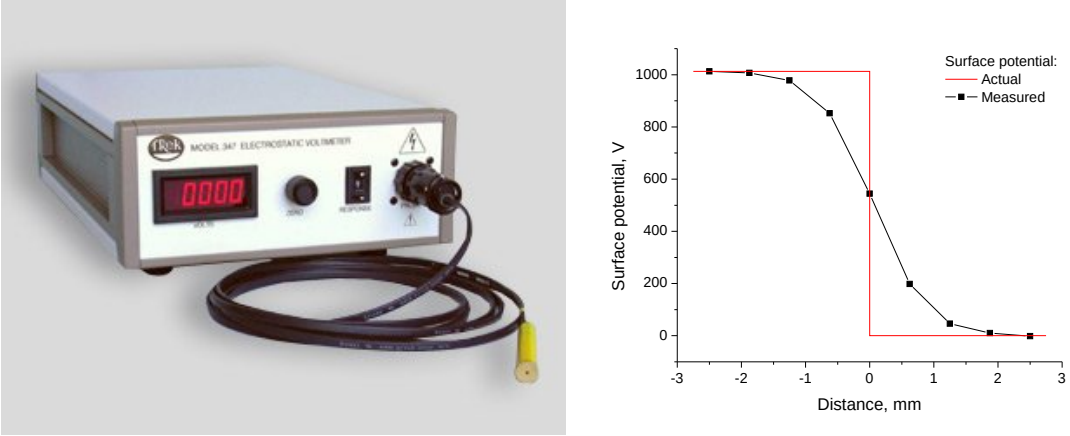

Figure 4.1: Electrostatic voltmeter and its spatial resolution.

The DBD plasma actuator used for these experiments was the same as in schlieren experiments, see Figure 1.5. It was made of copper foil electrodes and 100 μm thick kapton tape. The width of the electrodes was equal to 25 mm and their spanwise dimension was 75 mm. A 100 μm thick kapton tape was used as the dielectric. The discharge was ignited by applying high voltage to one of the electrodes. The other electrode was grounded.

4.3 Numerical model

In order to enable simulations of actual experiments, a simplified numerical model was developed. The original numerical model developed by A. Likhanskii, [49, 51, 47], was derived from the first principles and incorporated full plasma kinetics for electrons and both positive and negative ions coupled with the electric potential and surface processes. This model requires a very long computational time to calculate even several pulses. In this model, the time step was defined from the Courant-Friedrichs-Lewy (CFL) condition for electrons. However, during most of the voltage cycle (the time between the pulses and even a significant portion of the pulse), the electron number density is very low, and the plasma consists predominantly of ions. This enables significant simplification of the model, making it much faster, but still valid qualitatively. By setting the CFL condition defined by the slow ions when the electron density falls below a certain threshold, the computations were made much faster.

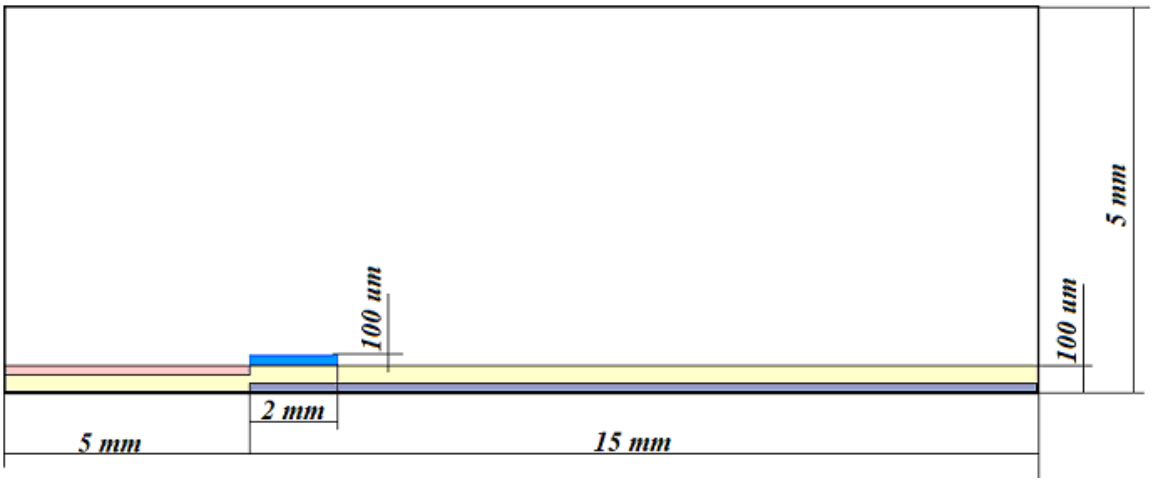

Figure 4.2: Computational domain for surface charge build up.

The modeling was performed for sea-level atmospheric air at room temperature. Air chemistry was not considered in details. The plasma was considered as a three-fluid mixture, consisting of neutrals, and positive and negative ions. The plasma

kinetics included only ion-ion recombination, and interaction with neutral gas was modeled in the drift-diffusion approximation. These simplifications allowed increasing the size of the computational domain from sub-millimeter to a practical size of 20 by 5 mm.

The breakdown phase and plasma formation were not calculated. Instead, it was assumed that the breakdown produces uniform neutral ion-ion plasma of 2 by 0.1 mm with an ion number density of 10^{15} cm^{-3}, Figure 4.2. The values of the plasma dimensions and ion number density were taken according to the results of the original full model. The uniformity of charge distribution and charge neutrality are assumptions which are not exactly true and, as shown later, lead to some deviations from the experimental results. The "pulses", i.e. the ion-ion plasma production, were applied at 10 kHz rate. 2 kV dc positive bias voltage was applied to the electrodes.

4.4 Results

4.4.1 Sinusoidal voltage experiments

First, experiments were conducted for the 3 kHz 10 kV peak-to-peak sinusoidal voltage profile. Since the sinusoidal profile is widely used in DBD experiments, [4] it is interesting to compare its surface potential distribution with the one obtained in pulsed DBD.

The actuator was run for 15 seconds and then the surface potential was measured. Each surface potential measurement was repeated five times. The standard deviation is shown in the figures with a dash line. The result is presented in Figure 4.3, where the distance is measured from the edge of the exposed electrode. The plasma extends only a few millimeters downstream of the edge of the exposed electrode, whereas the dielectric charge extends centimeters away from it, far downstream of the plasma.

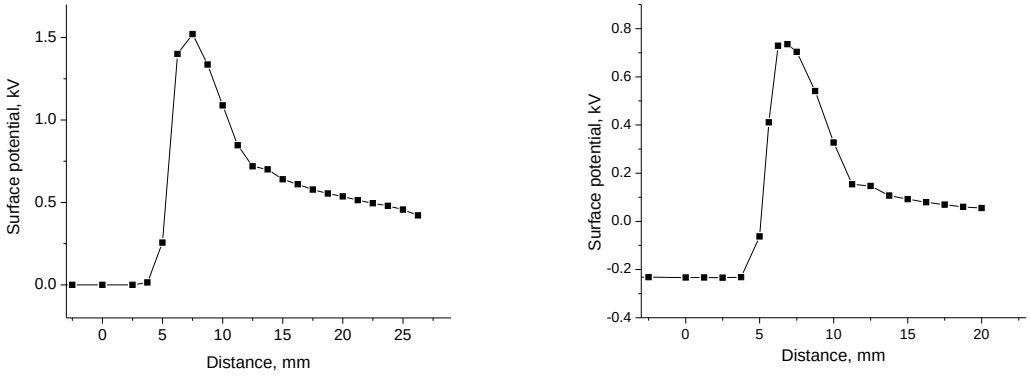

Figure 4.3: Surface potential distribution. Applied voltage profile - sinusoidal 3kHz, 10kV peak-to-peak. Electrodes edge at 0. On the right, the same with 167 pF capacitor in series with the plasma actuator.

The maximum surface potential 1.5 kV is comparable to the applied peak voltage 5 kV. This means that the electric field of the surface charge can significantly distort the electric field produced by the voltage applied to the electrodes. Also, even though the applied voltage is symmetrical sinusoidal with no bias voltage the time-averaged surface charge has a positive polarity. This is possibly due to the much higher mobility of electrons compared to positive ions which leads to a much higher electron current into the exposed electrode during the positive half-cycle of the sinusoidal voltage compared to the positive ion current into the exposed electrode during the negative half cycle.

With this reasoning one might conclude that there is a net negative current into the exposed electrode and positive current flow from the DBD to infinity. This picture is consistent with results from two further experiments. In one, a 167 pF capacitor was inserted in the circuit between the power supply and the exposed electrode. From the results, presented in Figure 4.3, we can see that the potential of the exposed electrode (negative values of distance) is negative and maximum positive potential value decreased. It proves that on average there is a negative current to the exposed

electrode.

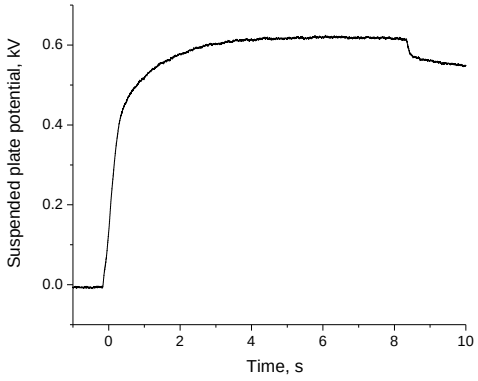

Figure 4.4: Suspended plate in the induced flow potential. A metallic plate put in the induced flow 3 cm downstream gets positive charge S = 35 cm^2. Applied voltage profile - sinusoidal 3kHz, 10kV peak-to-peak.

In the second experiment a copper plate was placed in the plasma induced gas jet 3 cm downstream the plasma. The plate was suspended in the air so it did not touch the actuator, and an electrostatic voltmeter was used to monitor its potential versus time. The result is shown in Figure 4.4. It can be seen that the plate gains a significant positive potential 600 V. Similar behavior is observed in asymmetric rf discharges, where there is a positive current flux to a virtual electrode at infinity, [57]. In addition the role of positive and negative oxygen molecular ions in the plasma, their attachment to the surface, and surface dominated mechanisms of charge build up and charge removal may be important. These effects need to be further studied.

The persistence of surface charge far downstream of the plasma could be due either to surface mobility of the charges or to deposition of the charges onto the surface from the gas jet downstream of the plasma. Estimates show that while the dielectric surface charge mobility is too low, the deposition of ions from the DBD-generated tangential gas jet is likely to persist downstream of the plasma. Indeed, in the DBD generated jet downstream of the visible plasma, plasma electrons, no longer regenerated by ionization, rapidly in tens of nanoseconds recombine with positive ions and attach to oxygen molecules, which results in an ion-ion plasma jet with an

estimated ion-ion recombination time on the order of several milliseconds. At a jet velocity of several m/s, this translates into several centimeters of ion-ion plasma and thus into several centimeters of dielectric surface charge.

4.4.2 Pulses with dc bias experiments

In this set of experiments the voltage profile consisted of 3 kV 8-ns FWHM ionization pulses superimposed on 2 kV dc bias voltage. The pulse repetition rate was 10 kHz and the plasma was run for 10 s. The results of surface potential measurements are presented in Figure 4.5. As in the case of a sinusoidal voltage, the charge builds up far downstream the plasma region. As can be seen from Figure 4.5, the magnitude of the surface potential is quite close to that of the bias voltage, while the magnitude of the ionization pulse voltage has little effect.

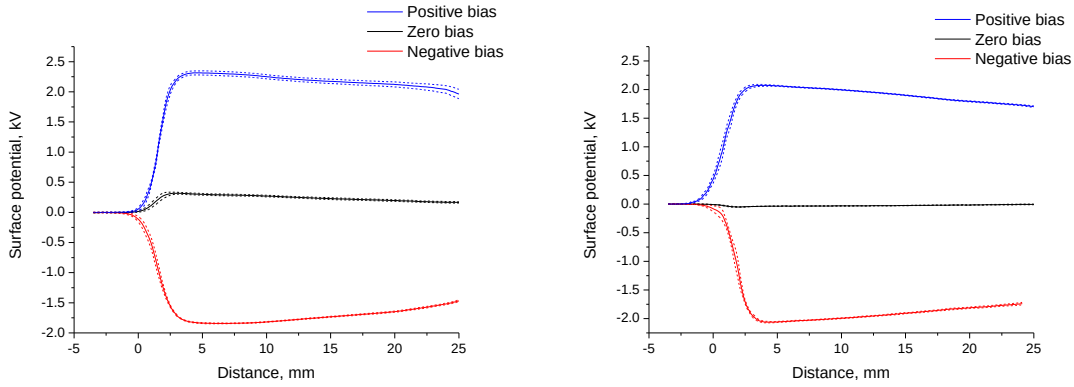

Figure 4.5: Surface potential distribution for positive (right) and negative (left) polarity of ionizing pulses. Applied voltage profile: 2 kV dc bias, 3 kV pulses at 10 kHz PRR.

We next examined how quickly the surface charge builds up. At a selected dc bias voltage, a predetermined number of pulses was sent to the actuator, and then the surface potential was measured. Results for four possible combinations of pulses' and biases' polarities are shown at Figure 4.6. Even though for a small number of

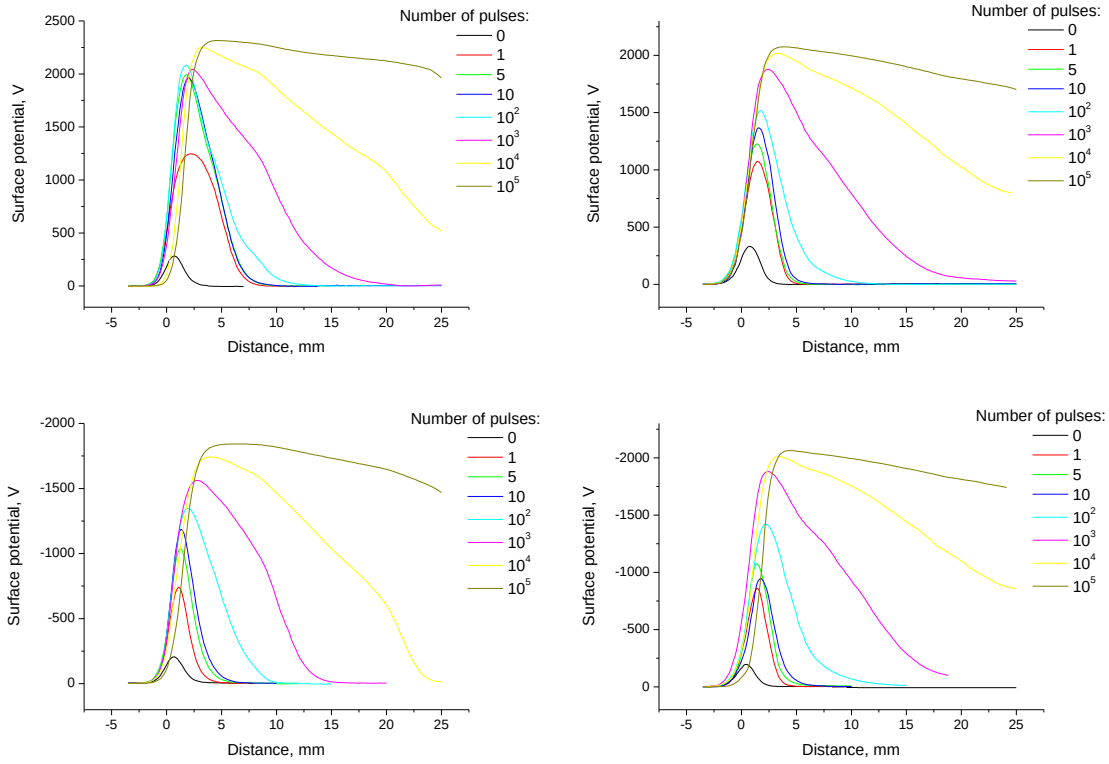

Figure 4.6: Surface potential for a fixed number of pulses in different pulse and bias polarities. Positive pulses (left columb), negative pulses (right columb), positive bias (top row), negative bias (bottom row). Applied voltage profile: 2 kV dc bias, 3 kV pulses at 10 kHz PRR.

pulses the accuracy of the measurements is low, it can be seen that even a single pulse creates a noticeable surface charge. As the number of pulses increases, the surface charge builds up and moves farther away from the plasma. After thousands of pulses, the surface charge is close to its steady-state value. We have also found that 2 kV bias voltage itself builds up some surface charge at the dielectric. The charge is smaller then the one built by a single pulse but is still significant.

We have also found that positive pulses added to positive bias are significantly more efficient in depositing the charge on the surface than other combinations of the pulse and bias polarities. This effect is illustrated in Figure 4.7.

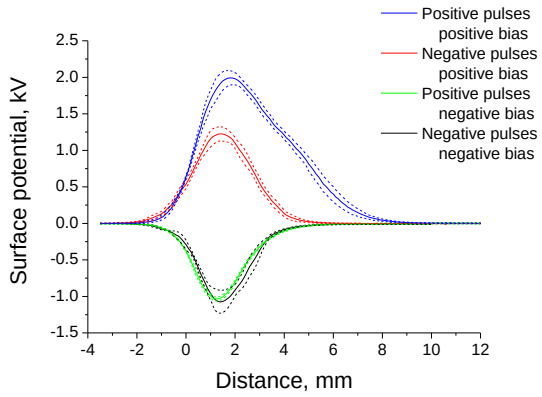

Figure 4.7: Surface potential after 5 ionizing pulses for different pulses and bias polarities. Applied voltage profile: 2 kV dc bias, 3 kV pulses at 10 kHz PRR.

The purpose of the next set of experiments was to study the evolution of the surface charge with time after the discharge has been turned off. The results for both polarities of the bias voltage are presented in Figure 4.8. The results show very similar potential distribution for both signs of the charge. As seen in Figure 4.8, the charge persists for a very long time. In 30 min it depletes by only 15%-20%. There is uniformly slow charge depletion from the surface in the region of low gradients of the charge concentration and a relatively fast depletion close to the exposed electrode in the region of high gradients. The fact that the depletion occurs at the same rate for both positive and negative charge is consistent with the charged particles at the dielectric surface being positive and negative ions from the gas rather than electrons.

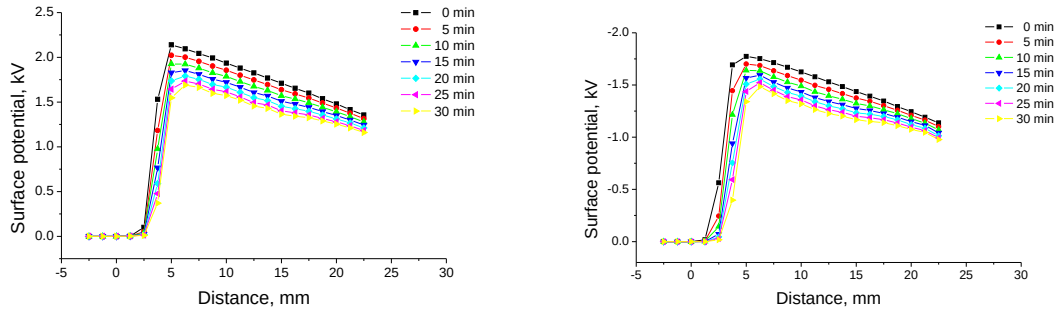

Figure 4.8: Surface potential versus time for positive (right) and negative (left) surface charges.

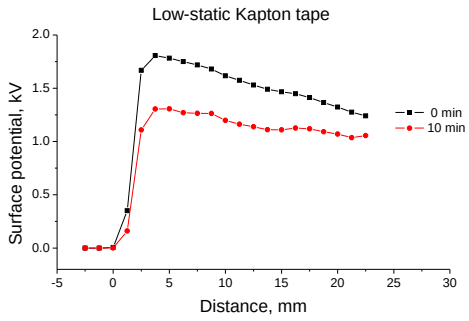

Figure 4.9: Surface potential versus time. In this experiment low-static kapton tape was used instead of conventional kapton tape.

An experiment was conducted with a plasma actuator in which a conventional Kapton tape was substituted by a lowstatic Kapton tape of the same thickness.[24] The results, see Figure 4.9, show that the depletion rate is faster for the low-static Kapton tape, but the characteristic time is still of the order of tens of minutes.

Note that Roth et al, [54], also observed the slow depletion of the residual surface charge on the dielectric after the driving voltage was turned off. The typical time periods were up to 30 s, which is much shorter than the times we observed. This difference is associated with the difference in dielectric materials and their conductivity, Roth et al used glass. A similar, about one minute, charge depletion time was observed by us with MACOR dielectric.

4.4.3 Comparison to numerical simulation

The simulation shows that a positively charged ion cloud drifts downstream along the electric field lines building the surface charge upon the dielectric. The negative ions either recombine with the positive ions remaining in the plasma region or disappear into the exposed electrode. Figure 4.10 presents comparison of the evolution of the surface charge obtained numerically and experimentally. First, we can notice that the charge profiles look the same in both cases. In the beginning, the surface charge builds up in the plasma region mostly. When the surface charge builds up to such a level that it distorts the applied electric field it starts building up downstream.

In both cases, the rate of charge built up decreases with a number of the applied pulses. The computed steady state density of surface charge agrees well with the experimental value. It corresponds to a value at which the applied bias voltage is shielded by the surface charge.

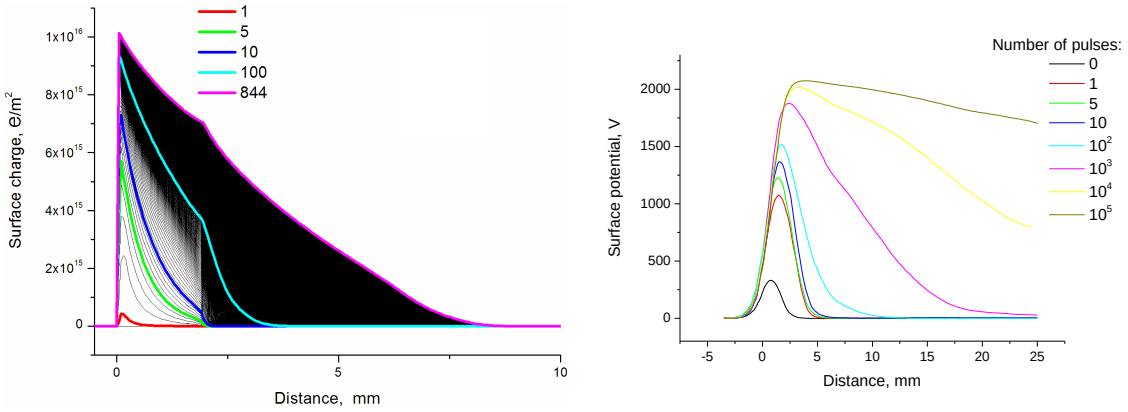

Figure 4.10: Surface build up: simulation (left) vs. experiment (right)

Of course, the assumptions about uniformity and neutrality of the ion-ion plasma introduce some error. As a consequence, the numerical model underpredicts the amount of charge deposited by the first several pulses. Also, the experiment shows that the surface charge extends farther downstream than the model predicts.

4.5 Three-electrode DBD configuration

One of the numerical results published by Likhanskii et al in 2006, [49], was a prediction of efficient operation of DBD plasma actuator driven by short repetitive pulses superimposed on DC positive bias voltage. Schlieren experiments described in Chapter 3 did not confirm this prediction. The reason was found to be the surface charge build-up which shields the applied bias field. As a solution it was proposed to switch the bias periodically.

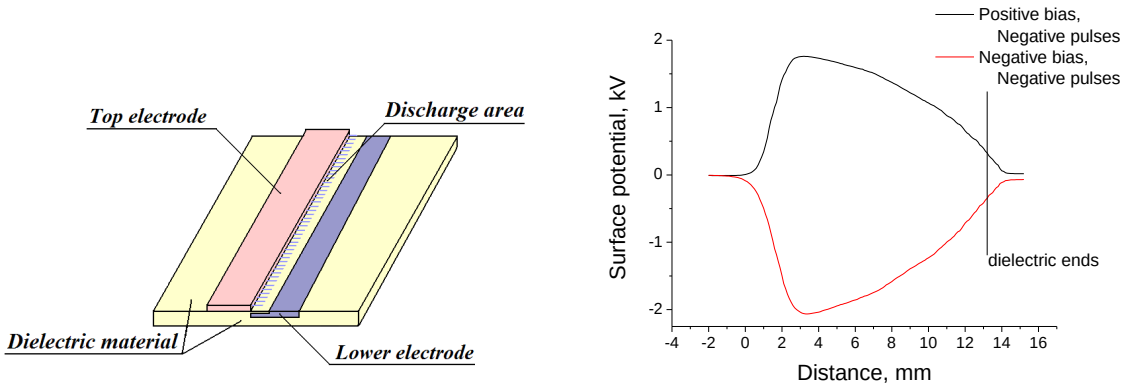

Figure 4.11: Modified DBD plasma actuator and surface potential distribution in it.

In this chapter we found that the surface charge builds up far downstream from the plasma. We therefore propose a modification to the actuator configuration. The dielectric covers only part of the lower electrode, for example half of an inch, leaving the rest of the electrode (another half of an inch) exposed, as shown in Figure 4.11. In such a case the surface charge can not build up far downstream and the DC bias voltage is not shielded. Indeed, the surface potential measurements, presented at Figure 4.11, show the modified charge distribution and suggest that the bias component of the electric field never gets shielded. One of advantages of such an actuator is a simpler bias voltage profile (dc but not ac). One should be careful with applying too high voltages, which can lead to an arcing over the dielectric. Use of a current limited power supply or an high resistance/inductance connected in series with the actuator might alleviate this problem.

Note that if a relatively thick dielectric layer is used, then simply cutting the dielectric layer off over a part of the lower electrode would produce a "step" which can be detrimental to aerodynamic drag. A simple modification of the idea would then be to put a third electrode on the surface and to electrically connect this electrode with the encapsulated electrode, rather than cutting the dielectric off.

The three-electrode DBD configuration resembles that of the sliding discharge, [58, 59, 60]. However, in sliding discharges the plasma actually reaches both exposed electrodes. In contrast, in the three-electrode DBD discharge proposed here, the electrons would not reach the auxiliary electrode whose purpose is simply to reduce or eliminate the charge accumulation on the dielectric surface.

4.6 Summary

In this chapter, surface charge dynamics in DBD plasma actuators was studied. Direct measurements of the dielectric surface potential and its dynamics in asymmetric dielectric barrier discharge DBD plasma actuators show that the charge builds up at the dielectric surface and extends far downstream of the plasma. The electric field of the surface charge can dramatically distort the field produced by the voltage applied to the electrodes and thus reduce the actuator performance. The surface charge persists for a long time tens of minutes after the driving voltage has been turned off. For a sinusoidal voltage waveform, the dielectric surface charges positively. With the voltage waveform consisting of nanosecond pulses superimposed on a dc bias, the sign of the dielectric surface charge is the same as the sign polarity of the bias voltage.

A simplified numerical model has been developed for the surface charge evolution. A good agreement of the modeling with the experimental data has been demonstrated, including evolution of the surface charge, rate of its buildup, and the charge profile shape. This provides evidence that the surface charge is deposited by the ions which drift from the plasma region to the dielectric surface in the applied bias field, and not through the surface conductivity. Some deviations seen when comparing the modeling results with the measurements are due to the assumptions made to simplify the model, particularly the uniformity and neutrality of the initial ion-ion plasma.

Chapter 5

Thrust Measurements

In this chapter DBD plasma actuators driven by repetitive nanosecond pulses added to dc or low frequency bias voltage are studied, and parametric results of plasma-induced thrust versus voltage profile parameters are presented. The results of the thrust measurements agree with schlieren visualization results obtained earlier and indicate that dielectric surface charge plays a major role in the thrust production.

In addition, two new configuration of the DBD plasma actuators are proposed an asymmetric DBD plasma actuator with a slightly conductive dielectric and a DBD plasma actuator with a slightly conductive silicon coating. Two materials that have been considered as slightly conductive dielectrics – zinc oxide and linen based phenolic, show some promise, but one is too conductive, and the other too resistive. Regarding silicon coated DBD, experiments on the produced force and its dependence on the driving voltage and coating parameters are performed. It is shown that the new configuration of the plasma actuator suppresses charge buildup and that it can be efficiently driven by a dc voltage only.

5.1 Introduction

In Chapter 3, the schlieren technique is used to evaluate the plasma actuator performance. This approach is totally non-intrusive and permits studies of the induced flow structure. However, direct plasma-induced thrust measurements are more convenient, because, although not revealing the details of the induced flow, such measurements yield the body force which, when inserted into the equations of fluid dynamics, allows one to model the entire flow. Also, the thrust measurements can be used to verify results obtained by the schlieren experiments. The force measurements for DBD were performed before [15, 29, 61], but we used another voltage profile, namely nanosecond pulses added to dc bias voltage. In this Chapter, a comparison of the DBD thrust driven by different voltage profiles including a time varying bias is made.

5.2 Thrust stand

A PL303 Mettler Toledo balance was used in the experiments. The maximum capacity of the balance is 310 g, readability - 0.001 g, typical settling time 3 s. Difficulties with such experiments are that the balance is electrically operated, and nanosecond pulses used for driving the DBD create a lot of electro-magnetic noise. This noise distorts the force readings significantly. A Faraday cage was constructed to shield the balance as shown at the Figure 5.1. It is mounted on optical table and consists of four aluminum plates (with a hole for the post in the top plate) and one copper grid. The actuator is mounted on a dielectric post. It was found experimentally that instrumental error of the thrust stand was 3 mg.

A set of experiments was conducted in order to verify the accuracy of the measurements. First of all, we confirmed that the connecting wires do not alter the readings. This was done by placing a known weight on top of the actuator with connected wires.

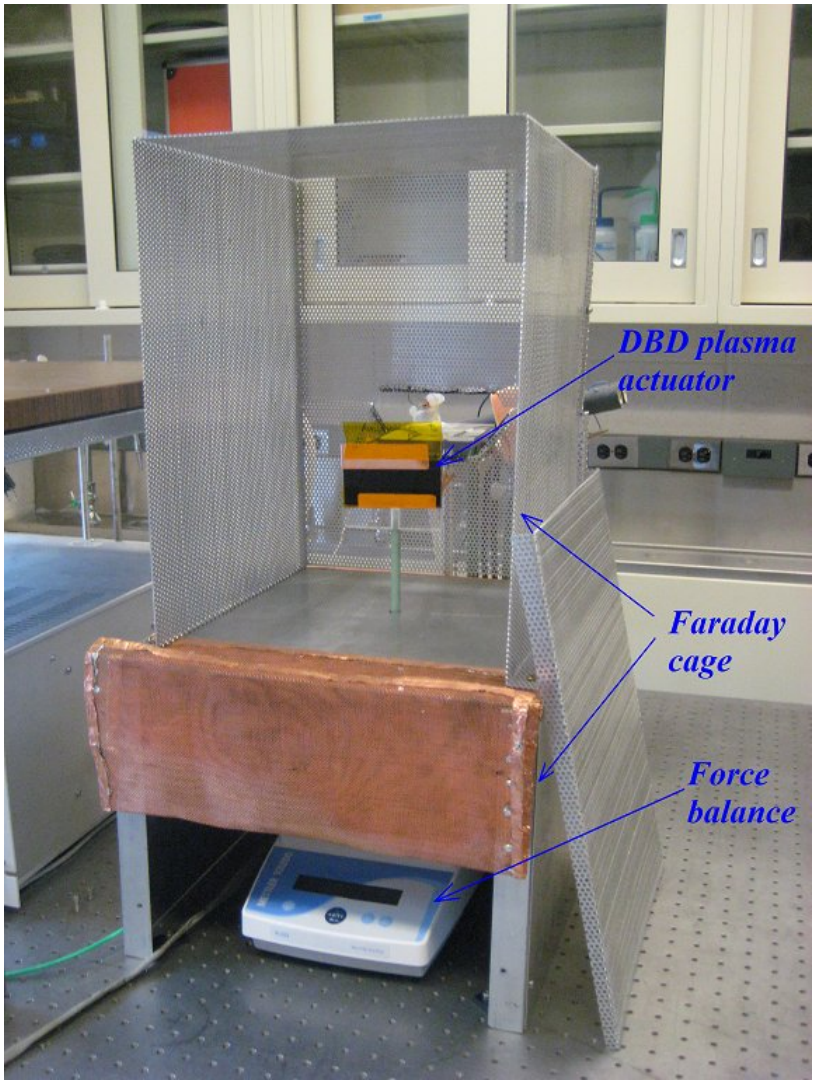

Figure 5.1: Thrust stand.

The weights ranged from 5 mg to 50 g and the error introduced by the connecting wires was not more that 1 mg, i.e. within the reading accuracy of the balance. Also it was noticed that the balance did not measure weights less then 5 mg. Second, the fact that electro-magnetic noise created by the discharge does not affect the readings was checked by fixing the actuator (so it did not act on the balance) and running the plasma. The balance readings remained zero when the plasma was ON. Third,

the actuator was mounted upside down and observed to create the same force on the balance but in the opposite direction. Thus we can conclude that the setup works properly and measures the actuator induced thrust.

Each set of data was taken the same day to exclude air humidity variations mentioned in the Introduction. Each measurement was done three to five times and the result were found to be very repeatable as long as taken close in time.

5.3 Results

5.3.1 AC bias

Schlieren visualization presented in Chapter 3 has demonstrated that running DBD plasma actuator with nanosecond pulses added to alternating bias voltage is an effective way to couple momentum into the gas. This configuration of the actuator was also tested on a thrust stand.

In these experiments the same plasma actuator as for schlieren visualization is used. It consists of two electrodes placed asymmetrically on either side of a thin dielectric, with one electrode encapsulated, and the other exposed to the atmospheric air as shown at Figure 1.5. The electrodes are made of copper foil. The width of the electrodes was equal to 25 mm and their spanwise dimension was 75 mm. A 100 micron thick kapton tape was used as the dielectric in all experiments except where noted. The discharge is ignited by applying high voltage to the top electrode. The encapsulated electrode is grounded.

A comparison of different bias profiles was done. From the results presented in Figure 5.2 we can see that rectangular wave bias profile provides the highest thrust. The produced thrust correlates very well with the average of the absolute value of bias voltage which is defined as $\frac{1}{T}\int_0^T |f(t)|dt$, where T is period, and is proportional

to 0.64 : 1 : 0.5 : 0.5 : 0.5 for sinusoidal, rectangular, triangular, positive and negative sawtooth respectively. The measured thrust is almost the same for both polarities of the pulses. Some deviation from this rule is observed in the case of the rectangular bias profile where negative pulses produce higher force. The question of why the thrust of negative and positive pulses is different for the rectangular bias and is the same for other bias profiles is still open. Based on these results, all further experiments were conducted with rectangular bias voltage profile.

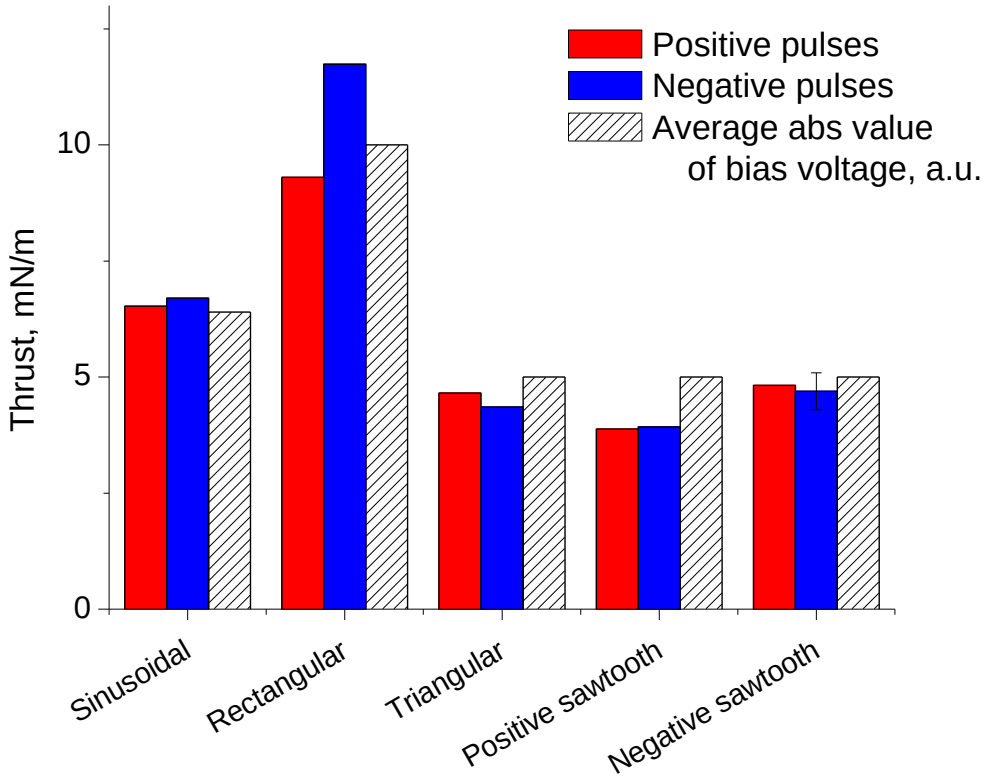

Figure 5.2: Thrust for different bias profiles. Bias 10 kV peak-to-peak, 100 Hz; Pulses 3 kV, 25kHz.

The effect of bias positive and negative duty cycles was also investigated. In these experiments the frequency and voltage of the bias profile were fixed and the relative

time duration of positive and negative periods was varied. The results are presented at Figure 5.3. For case of positive ionization pulses the optimum regime was found to be when the bias is positive for less than 10% of the time and negative the other time. For case of negative ionization pulses 50% duty cycle is most efficient one. The results agree with ones obtained by means of schlieren visualization before, see Figure 3.14 for example. It was shown that in case of positive ionization pulses the plasma actuator induced a very strong wall jet in the negative half cycle of bias voltage and a relatively weak one in positive half cycle. In case of negative ionization pulses, the induced wall jets of both half cycles are approximately of the same strength. It can be due to difference in surface charge build up. The surface charge measurements presented in Chapter 4 showed that positive pulses added to positive bias voltage deposit more surface charge than any other combination of pulse and bias polarities, see Figure 4.7.

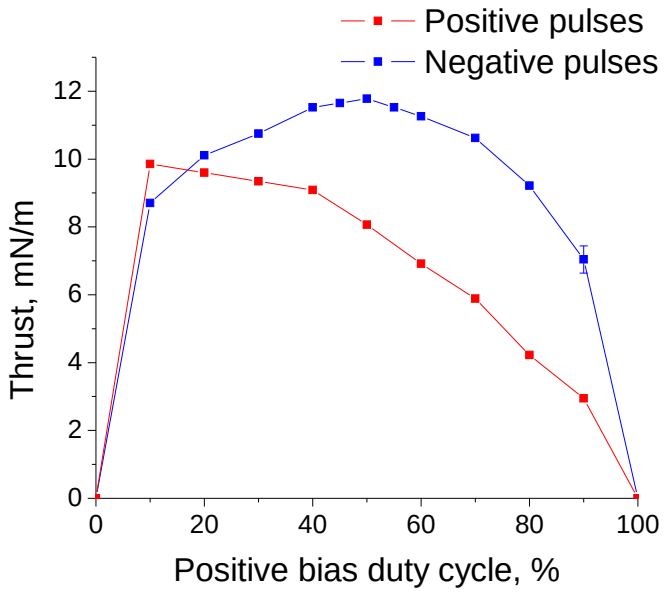

Figure 5.3: Thrust for different bias duty cycles. Bias: rectangular, 10 kV peak-to-peak, 100 Hz; Pulses: 3 kV, 25kHz

Also the effect of ionization pulse duty cycle was investigated. Keeping the total number of ionization pulses the same we increased pulse repetition rate and decreased the ON time. From the results shown at Figure 5.4 we can see that the uniform distribution of pulse in time is most efficient. Reducing the duty cycle down to 50% decreases the effect by 30%.

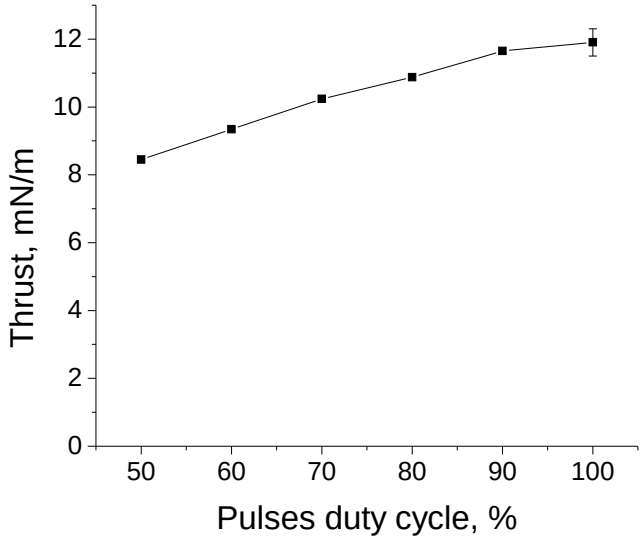

Figure 5.4: Thrust for different pulses duty cycles. Bias: rectangular, 10 kV peak-to-peak, 100 Hz; Pulses: negative 3 kV, 25kHz

Thrust dependence on the pulse repetition rate, pulse voltage, bias frequency and bias voltage was investigated. The results for both polarities of the pulses are presented at Figure 5.5 and Figure 5.6. For these measurements a baseline was chosen: bias voltage 10 kV peak-to-peak, 100 Hz frequency, rectangular, ionization pulse voltage 3 kV at 25 kHz ionization pulse repetition rate in continuous mode. Then one parameter at a time was varied. As can be seen from the figures, the bias voltage has greatest impact on the induced thrust. An increase of the other parameters also leads to an increase in force but not so fast. Note that the effect

saturates with the bias frequency at around 50 Hz.

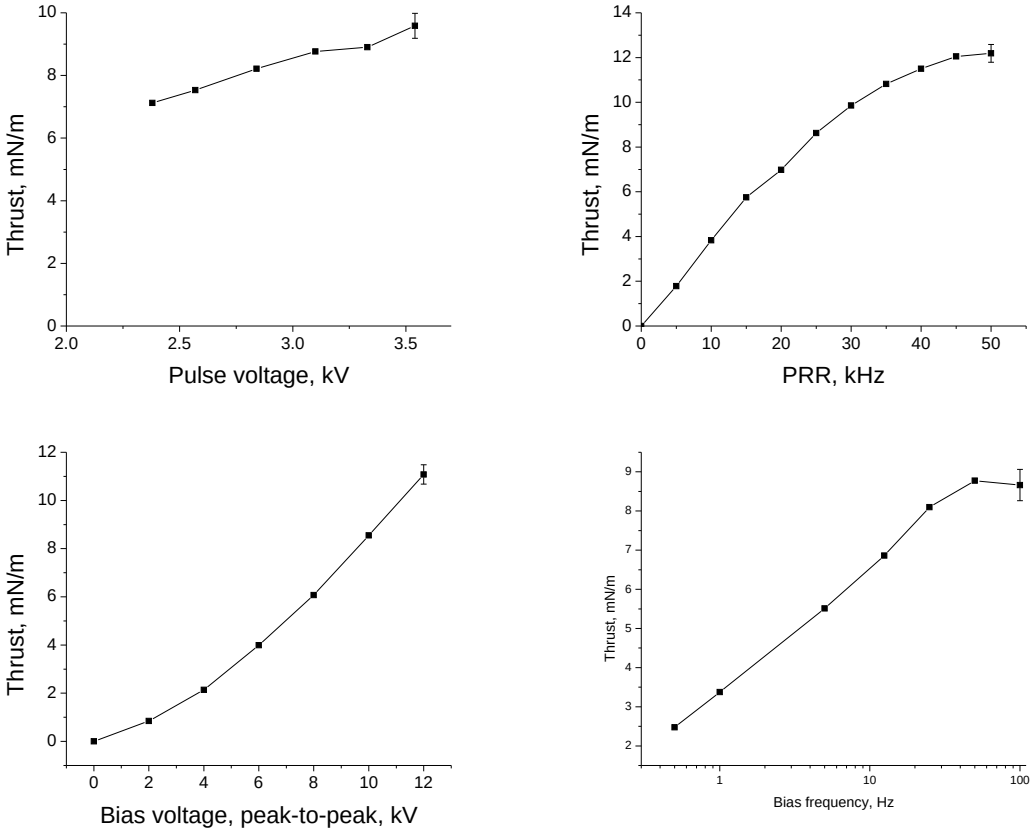

Figure 5.5: Thrust dependence on applied voltage parameters. Positive pulses. Bias: rectangular, 10 kV peak-to-peak, 100 Hz; Pulses: 3 kV, 25kHz

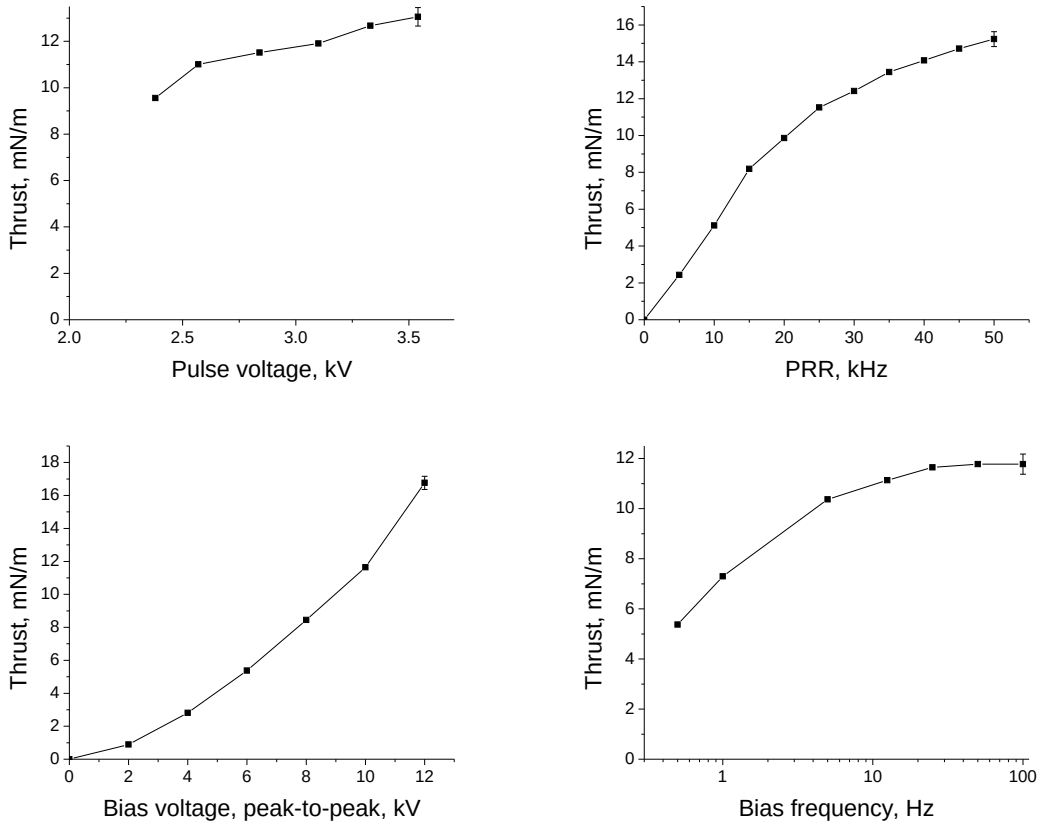

Figure 5.6: Thrust dependence on applied voltage parameters. Negative pulses. Bias: rectangular, 10 kV peak-to-peak, 100 Hz; Pulses: 3 kV, 25kHz

5.3.2 Three-electrode configuration

Three-electrode configuration of DBD plasma actuator was proposed in Chapter 4 as a solution to the surface charge problem. The solution is based on the fact that the surface charge builds up far downstream from the plasma. It was shown that placing a third electrode downstream mitigates the bias voltage shielding.

Plasma actuator used in the experiments is made of MACOR ceramic and copper plates. The length of the actuator is 75 mm. The dielectric (MACOR) covers only part (13 mm) of the lower electrode, leaving the rest (25 mm) of the electrode exposed, as shown in Figure 5.7. In such a case, the surface charge cannot build up far downstream

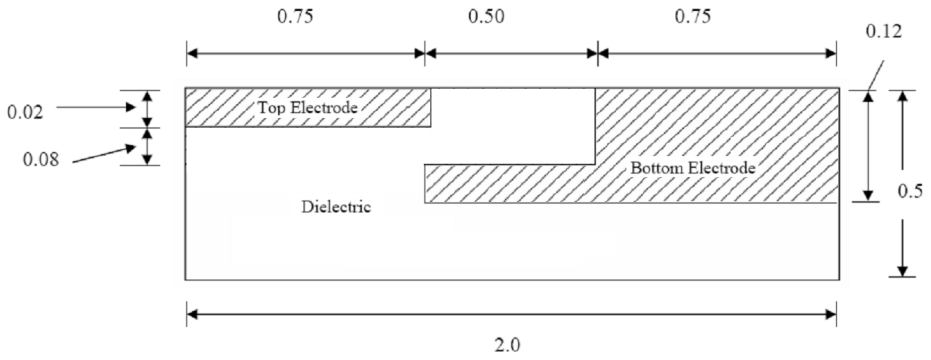

Figure 5.7: Side view of DBD plasma actuator in three-electrode configuration with dimensions. All dimensions in inches (not to scale).

and the dc bias voltage is not shielded, as is shown in Figure 4.11.

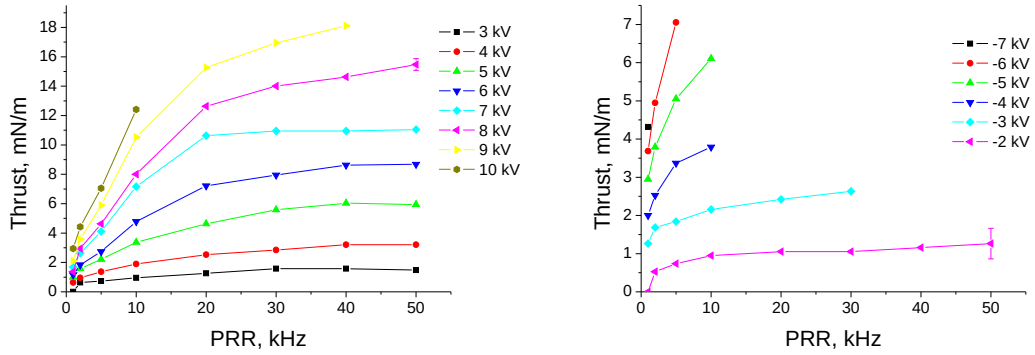

Figure 5.8: Thrust measurements in three-electrode DBD plasma actuator. Left is as a function of pulse repetition rate with positive bias, Right is as a function of pulse repetition rate with negative bias.

Thrust measurements for this configuration were performed and the results are shown at Figure 5.8 and Figure 5.9. The voltage profile consisted of 7 kV 17 ns (FWHM) negative pulses added to dc bias voltage. It can be seen that, similar to the pulses plus ac bias configuration, the produced thrust strongly depends on bias voltage and saturates with the pulse repetition rate.

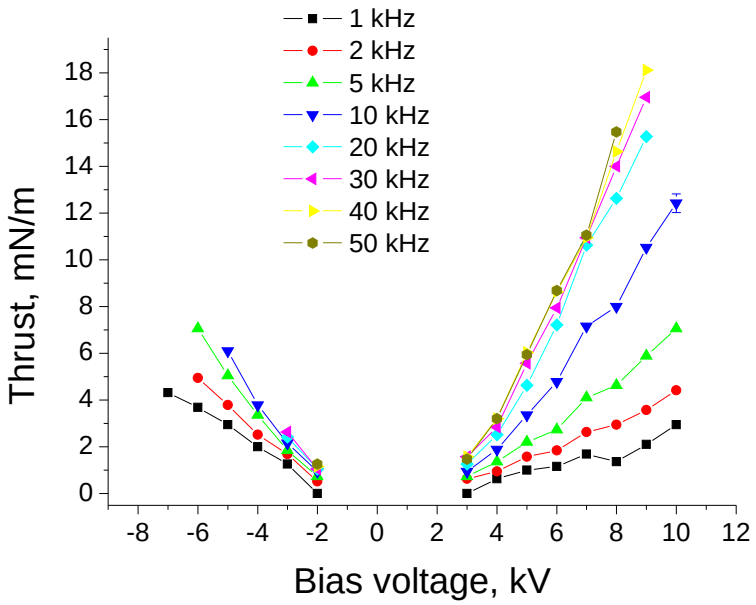

Figure 5.9: Thrust measurements in three-electrode DBD plasma actuator as a function of bias voltage at different pulse repetition rates.

5.3.3 Slightly conductive dielectric configuration

The three-electrode configuration is simple but as voltage or pulse repetition rate increases, a spark across the top and the bottom electrodes occurs. As one of the solutions to avoid the spark, we propose to use a "conductive" dielectric which will deplete the surface charge in the time between the pulses. We looked for materials with volume conductivity, which would allow depletion of the charge between the pulses. The depletion time can be estimated using an RC analogy, see Figure 5.10.

As can be easily seen from Figure 5.10, the depletion time is t = RC , where capacitance and resistance, which leads to C = $\epsilon\epsilon_0$S/d and resistance R = $\frac{d}{\sigma S}$, which leads to $\tau = \epsilon\epsilon_0/\sigma$. For a pulse repetition rate of 10 kHz and $\epsilon \approx 1$ the bulk conductivity should be at least $\sigma \approx 10^{-7}$Ohm^{-1} m^{-1}. At the same time, the conductivity cannot be too high.

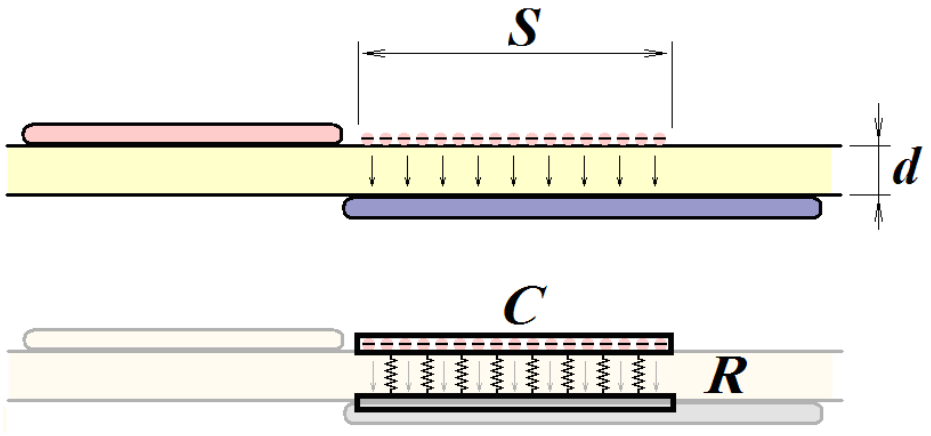

Figure 5.10: Surface charge depletion through the barrier and its RC representation.

3 mm thick, linen based phenolic and zinc oxide (ZnO) plates were used in the experiments. It is known that conductivity of such type of materials can vary significantly with the temperature, applied field, etc. The conductivity dependence on the applied field at room temperature was measured experimentally and is presented in Figure 5.11. The linen based phenolic conductivity was of the order of 5 $\times 10^{-10}$ - 1.5 $\times 10^{-9}$ Mho/m, for zinc oxide the range was 3 $\times 10^{-4}$ - 8 $\times 10^{-4}$ Mho/m.

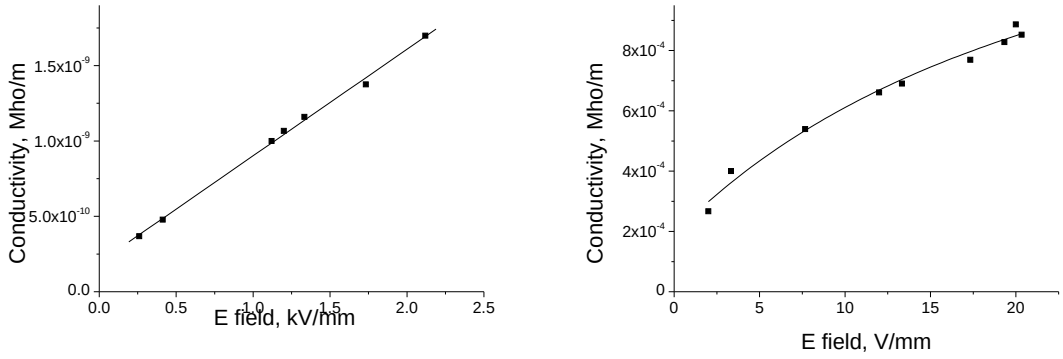

Figure 5.11: Bulk conductivity vs applied electric field for linen based phenolic (left) and zinc oxide (right).

The measurements were done by applying a known voltage to copper foil electrodes

placed symmetrically on the opposite sides of the plates. The Trek Model 20/20C HV Amplifier was used as the voltage source. Because the produced current was limited to 20 mA, the sample voltage applied to ZnO did not exceed 60 V, which is significantly lower than a typical bias voltage applied in the DBD experiments. Therefore, zinc oxide conductivity is expected to be much higher (one-two orders of magnitude) in the experiments. Thus, neither of the materials' conductivities is optimal one being too high, the other too low.

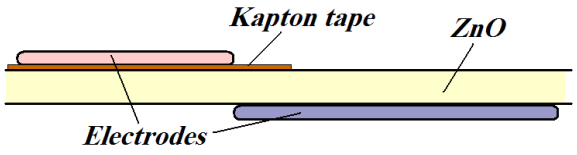

Figure 5.12: ZnO barrier plasma actuator.

The experiments showed that because of too high ZnO conductivity, it was not possible to ignite the discharge at the actuator. Thus, a Kapton tape was placed under the top electrode to insulate it from the plate as shown at Figure 5.12. This modification allowed igniting the discharge using nanosecond repetitive pulses. As a significant bias voltage was added, breakdown over the Kapton to the plate occurred. ZnO conductivity was high enough to provide very fast surface charge depletion and cause the discharge constriction thus making it not very convenient for further experiments.

The next set of experiments on thrust measurements was conducted using linen based phenolic DBD plasmas actuator. First, a waveform consisting of 17 ns FWHM negative pulses superimposed on positive bias voltage was studied.

The measured thrust dependence on the pulse voltage is shown in Figure 5.14. As expected, the thrust increases as the pulse voltage goes up.

Thrust dependence on pulse duration was studied for the first time, and the results are summarized in Figure 5.14. It was shown that for linen based phenolic plasma actuator there is almost no dependence on the pulse polarity and duration, except for 17 ns FWHM (longer) positive pulses that show lower efficiency.

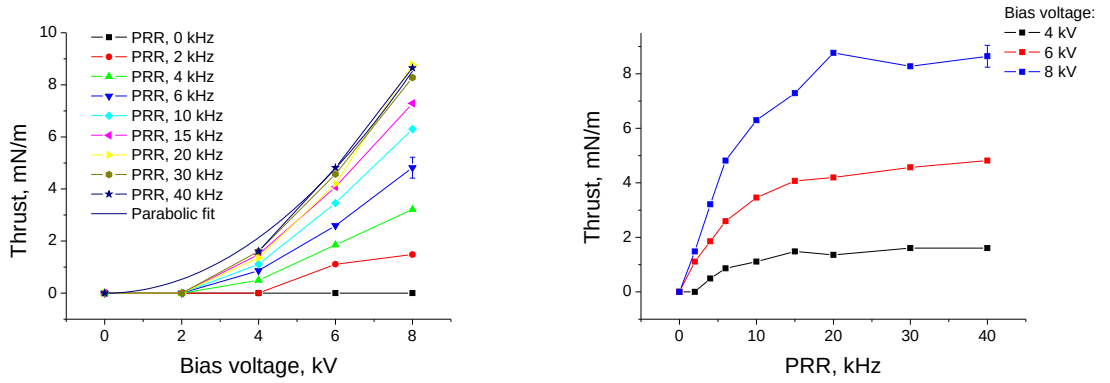

Figure 5.13: Thrust vs pulse repetition rate and bias voltage for linen based phenolic DBD plasma actuator.

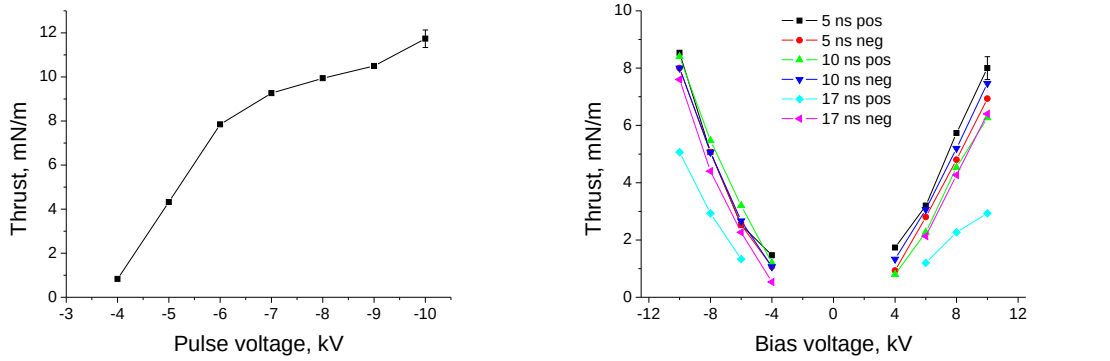

Figure 5.14: Left - Thrust vs pulse voltage. Bias voltage: positive 10 kV; pulse repetition rate: 10 kHz. Right - Thrust vs bias voltage for different pulse polarities and durations.

5.3.4 DBD with partially conductive coating

Alternative approach to the charge depletion is to coat the surface with partially conductive layer that bleeds the charge off. For these experiments the plasma actuators consisted of a 1/16" Macor plate coated with silicon on one side and two electrodes placed asymmetrically on either side, Figure 5.15. The electrodes were made of 100 micron thick copper foil. The width of the electrodes was equal to 1" and their spanwise dimension was about 2". The discharge was ignited by applying high voltage to

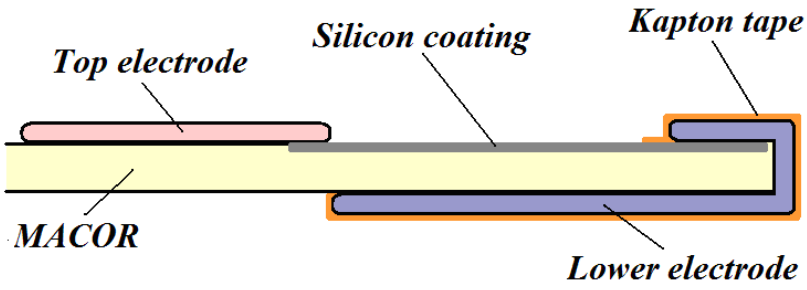

Figure 5.15: DBD plasma actuator with slightly conductive coating (the dimensions are highly exaggerated).

the top electrode. The lower electrode was grounded. The lower electrode was also wrapped around the plates edge to ground the coating and provide the charge bleed-off. It was covered with a Kapton tape to prevent arcing between the electrodes, ensuring that all the charge is depleted through the coating only, and preventing the discharge from passing around the sides to the lower side of the plate. The distance between the electrodes on the top side of the dielectric was equal to 1", length of exposed silicon coating was 3/4".

Silicon layers were deposited using chemical vapor deposition technique and were 0.4, 3.5, and 17.8 micron thick. The resistance of the coatings of a fixed thickness was measured in Ohms per square (or Ohm/□). These units come from the fact that resistance is proportional to the length and inversely proportional to the width. Therefore, a coating of a square shape has resistance that depends on its thickness and material conductivity only and does not depend on the size of the square. Assuming silicon resistance equals to 640 Ohm·m [62], it corresponds to 2.5×10^9, 2.8×10^8, and 5.6×10^7 Ohm/□. The actual resistance readings give somewhat different numbers: 7.5×10^8, 7.6×10^7, and 3.5×10^7 Ohm/□. The deviations might be due to existence of impurities in the silicon, which have a dramatic effect on the conductivity, and the strong temperature dependence of the conductivity of semiconductors. Also, as it

was discovered later by Kortshagen et al in [63, 64], the silicon coating conductivity can be changed over a wide range by luminosity.

An approach utilizing an RC analogy similar to one used before can be used to estimate the optimal conductivity of the coating needed for charge depletion between two sequential pulses, see Figure 5.17. The charge q on the surface equals to:

$$q = \frac{\epsilon\epsilon_0 SL}{d}U \tag{5.1}$$

where S – width of the coating, L – length of the actuator, U – surface potential. The draining current equals to:

$$I = \frac{ULh}{\rho S} \tag{5.2}$$

where h is the thickness of the silicon coating, ρ – bulk resistivity of the amorphous silicon. From Equations 5.1 and 5.2 the optimum conductivity of the silicon coating can be estimated:

$$\sigma = \frac{\rho}{h} = \frac{d}{\epsilon\epsilon_0 \nu W^2} \tag{5.3}$$

where ν is the frequency of the applied pulses.

Assuming $\epsilon_0 = 1$, $\nu = 10$ kHz, W = 18 mm, the optimum conductivity $\sigma \approx 5.2\times10^7$ Mho/$\square$, which close to the values of the conductivity of the tested samples.

Results of thrust measurements of the silicon coated DBD plasma actuators are shown in Figure 5.17. Different colors represent different coating thicknesses and different bias voltages and pulse polarities. Pulses were 17 ns FWHM long and had a 5 kV peak voltage. The pulse repetition rate was varied from 0 to 40 kHz. It can be seen that all combinations of pulse/bias polarities and coating thicknesses give similar values of thrust. As in other configurations of the actuators, the bias voltage has a biggest effect on the produced force. Figure 5.17 shows the effect of pulse repetition

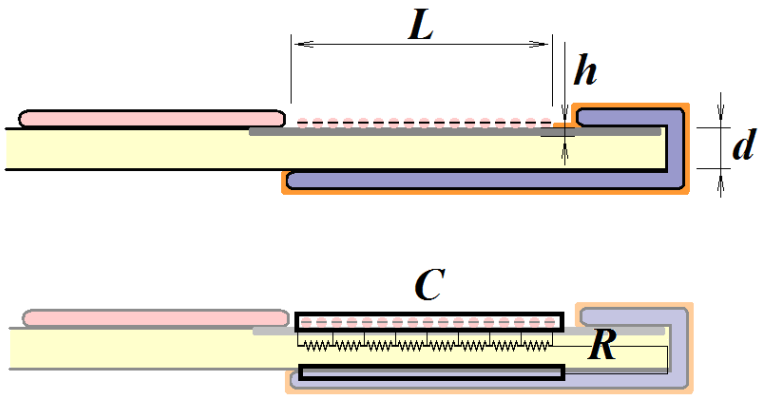

Figure 5.16: Surface charge depletion through the coating and its RC representation.

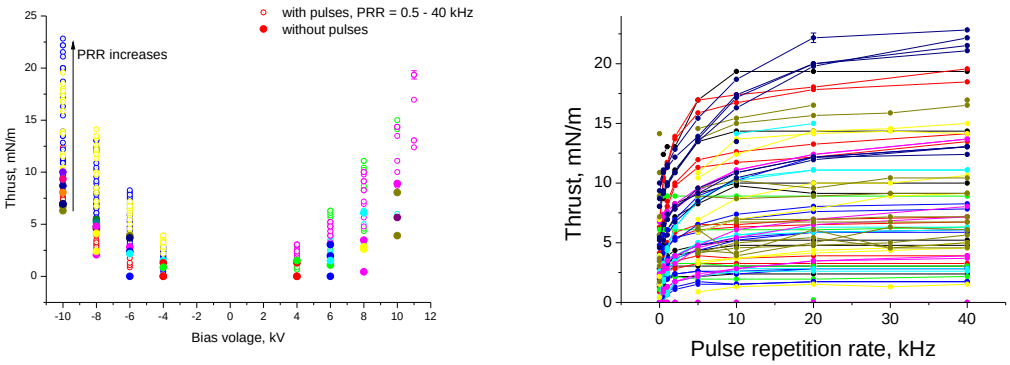

Figure 5.17: Thrust measurements for silicon coated DBD plasma actuator. Left - vs. bias voltage, right - vs. pulse repetition rate. Voltage profile: 17 ns FWHM 5kV pulses added to dc bias, PRR 0-40 kHz, bias voltage -10 - +10 kV.

rate. Again, as in other configurations of the actuators, the dependence is strong for low PRRs and saturates about 20 kHz.

The effect of the pulse polarity on the DBD performance is shown in Figure 5.18. It seems that both positive and negative pulses give comparable thrust values for the same operating conditions.

It also was noticed that with the thin electrodes, between 1/3 and 1/2 of the thrust is produced even in the absence of the ionizing pulses as shown by the solid circles in

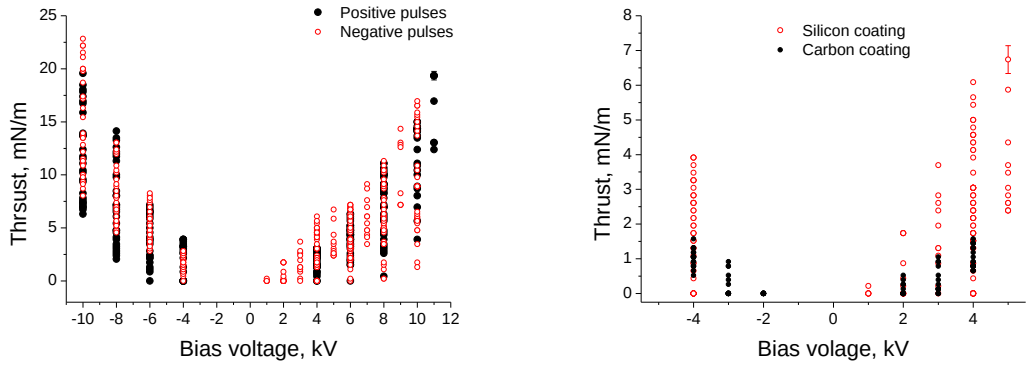

Figure 5.18: Left - produced thrust for different pulse polarities. Right - comparison of silicon and carbon coated actuators.

Figure 5.17. Indeed, the bias voltage is high enough to ignite a corona discharge at the electrodes edge. The nanosecond pulses only enhance the effect. In this case, the ions produced in corona discharge at the edge of the electrode drift towards the coated dielectric surface where they recombine without building up the surface charge. It turns out that the lower (buried) electrode does not play an important role anymore, since the electric field in the gas is defined by the top electrode and the coating, and thus the buried electrode can be removed altogether.

In addition to silicon coating, a 77 micron thick carbon coating on a 2 mm thick glass plate was investigated. The overall configuration was similar to the silicon coated actuator. The electrodes were made of 100 μm thick copper foil, the length of the actuator was 75 mm. The results of the thrust measurements are shown at Figure 5.18. The carbon coating demonstrated lower efficiency comparing to the silicon one. It was also not possible to get to higher bias voltage values because long sparks developed along the carbon surface, initiating a short circuit. It means that besides conductivity some other material characteristics, for example secondary electron emission, photo emission, can play important role when a coated actuator is considered.

5.4 Comparison of tangential body forces

At the present time a few groups have performed thrust measurements for DBD plasma actuators [29, 61, 15, 16] for different voltage profiles and dielectric parameters. Figure 5.19 and Figure 5.20 present some of the literature data plotted together with our results for comparison. Most of the data were obtained for sinusoidal voltage profiles. In the case of the pulses plus AC bias profile, the peak to peak bias voltage was used to characterize the amplitude of the applied voltage. The pulses plus DC bias profile was characterized by the value of the DC voltage.

These results appear to show that the "pulses plus sinusoidal bias" method generates a much stronger tangential force than the conventional sinusoidal voltage at the same voltage amplitude. Of course, since we have pulses, their amplitude also effectively adds to the "overall" voltage amplitude, so the direct comparison is tricky. However, we can claim that the amplitude of neither the sinusoidal bias nor the ionization pulses need be very high to achieve the performance equivalent to that of DBD with a conventional sinusoidal voltage. We can also say that there is a clear trend to improved performance with thicker dielectrics (both for us and for Corke et al [16]) that allow the use of higher voltages, plus there is a trend of improved performance when the bias frequency and ionization pulse repetition frequency are increased. We are optimistic that, if all those parameters are increased, the performance of the "pulses plus sinusoidal bias" system can be significantly higher than that of the conventional devices.

Figure 5.21 shows a comparison of different waveform used to drive the plasma actuator. Trying to compare apples to apples, we used the same dielectric material (100 micron kapton tape) in almost all these actuators. Only the silicon coating configuration utilized a MACOR plate due to the manufacturing requirements. As we can see, pulses plus bias are more effective for thrust production than sinusoidal

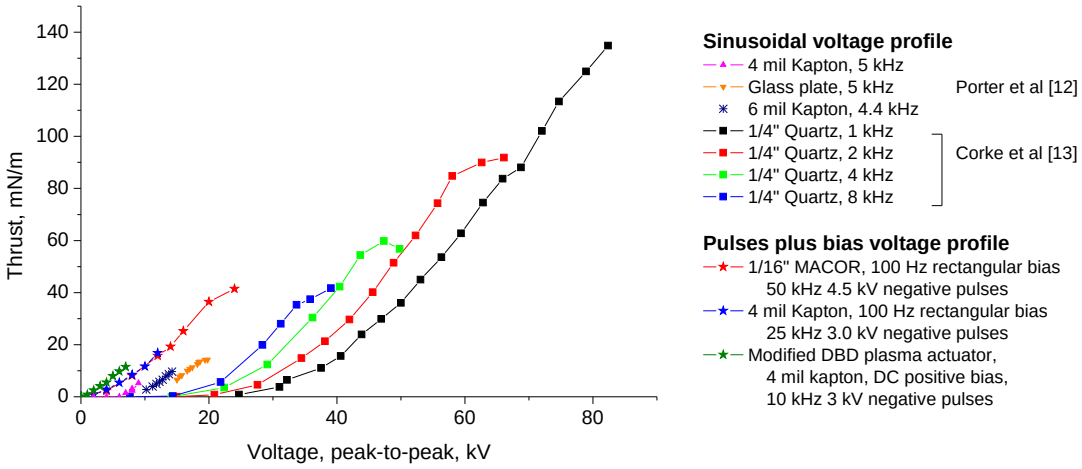

Figure 5.19: "Pulses plus AC bias" versus sinusoidal voltage: comparison of tangential body forces. Some data were taken from Porter et al [15] and Corke et al [16].

profile of the same amplitude. The silicon coating only shows a low performance because of order of magnitude thicker dielectric.

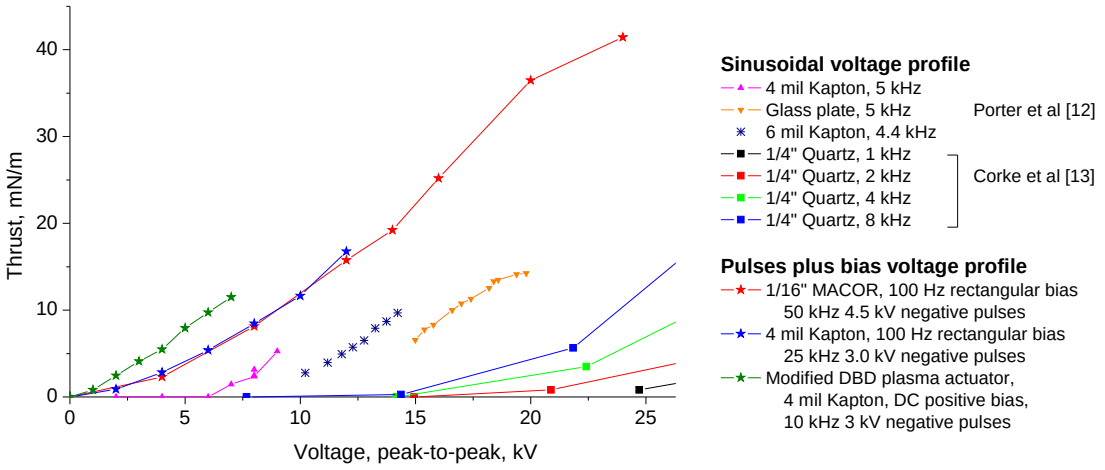

Figure 5.20: "Pulses plus AC bias" versus sinusoidal voltage: comparison of tangential body forces (zoomed-in). Some data were taken from Porter et al [15] and Corke et al [16].

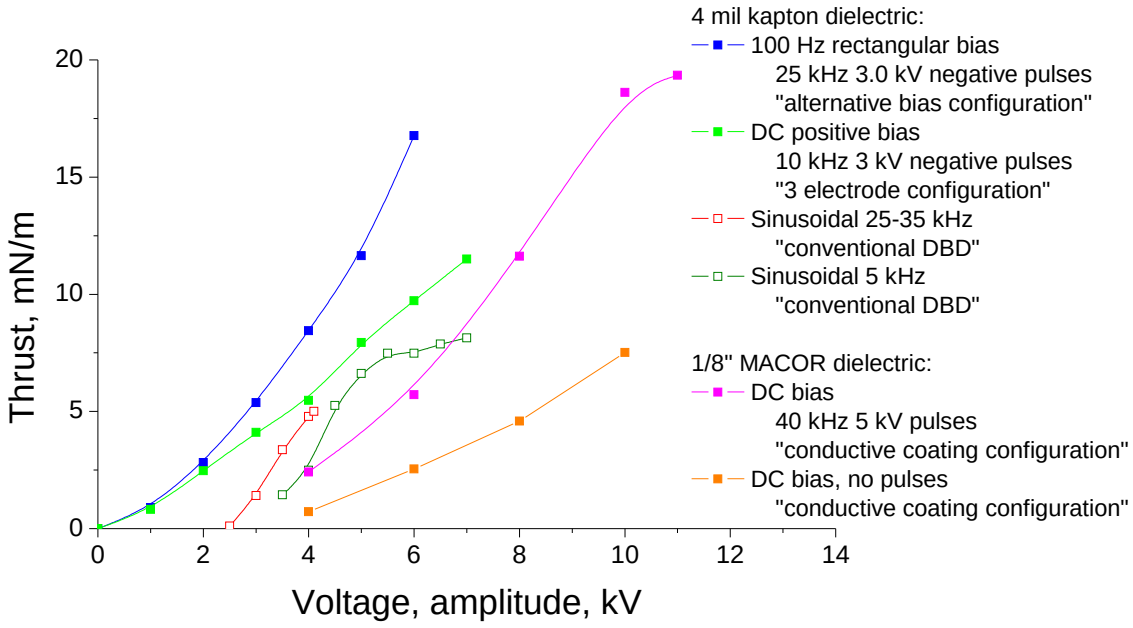

Figure 5.21: DBD produced thrust is different configurations.

5.5 Summary

In this chapter, thrust measurements for four configurations of DBD plasma actuators driven by repetitive ionization pulses added to dc or low frequency ac bias voltages are studied. The results of plasma induced tangential body force (thrust) measurements agree with schlieren visualization results obtained earlier. For all four configuration, force measurements show that the produced thrust is highly depended on the dc bias voltage. Thrust dependence on the ionizing pulses frequency is strong at low repetition rate and saturates around 20-40 kHz. The performance of the actuator is similar for both polarities of the pulses and bias voltage.

- **Pulses plus ac bias.** It is shown that a rectangular bias voltage is more effective than sinusoidal, triangular, or sawtooth. For positive pulses optimum performance is achieved when the bias voltage stays negative for more than 90 % of the cycle. For negative pulses the optimum duty cycle of the bias voltage is 50%-50%.

- **Three-electrode configuration.** Three-electrode configuration generates a slightly lower thrust at the same voltage amplitude but requires a simpler voltage profile than "ac bias". Also, the three-electrode configuration is susceptible to a breakdown over the dielectric since both electrodes are exposed.

- **"Conductive" dielectric configuration.** The optimal bulk conductivity of the dielectric was estimated. Two materials have been considered as slightly conductive dielectrics zinc oxide and linen based phenolic, one being too conductive, the other too resistive. No dependence on the pulse duration or polarity can be observed, except for long (17 ns) positive pulses which show lower performance. The slightly conductive dielectric approach requires a simple dc bias voltage, but strict material requirements (both suitable bulk conductivity and

breakdown voltage) may limit the configuration's applicability.

- **DBD with partially conductive coating.** Also, the effect did not depend on the coating resistivity in the range measured. Carbon coating is also investigated but found to be unsuitable for DBD application, since a spark develops along the surface and short circuits the electrodes. It has also been shown that the new configuration of the plasma actuator can be efficiently driven by DC voltage only. Compared with previously studied DC surface corona discharges [4], the main advantage of the new configuration with the coating is that the dielectric between both electrodes prevents the glow-to-arc transition, resulting in a more stable discharge and in a faster electric wind. In principle, the new configuration can be run without the lower electrode. The electric field in the gas is defined by the top electrode and the coating, so the lower electrode is fully shielded and thus can be removed.

Please note, that time average force is measured in the experiments. While the last three configurations produce steady state jets, the "ac bias" one works in burst mode.

Comparison of the thrust generated by the pulses plus bias waveform and by the conventional sinusoidal voltage shows the advantage of the former. Indeed, nanosecond ionization pulses superimposed on a low-frequency bias generate thrust comparable with that produced by the sinusoidal voltage, but at significantly lower voltage amplitudes. Still, little work has been done on optimization of the new configurations and higher performance can be expected. Based on the available data, ac bias + pulses configuration demonstrates the best performance. The configuration with partially conductive coating has the most flexibility due to the fact that the dielectric and the coating can be chosen independently. These two configurations, pulses + ac bias and partially conductive coating, look most perspective for future development.

Chapter 6

DBD Induced Wall Jets

In addition to wind tunnel tests of flow control, many groups [26, 4, 65, 66, 67, 68, 69, 70] have studied the DBD actuators in initially quiescent air. This approach enables relatively simple plasma and flow diagnostics and simplifies interpretation of the results. The most commonly used parameters of the actuator are the plasma induced jet velocity and thrust. These parameters, measured experimentally, are often used as input parameters for fluid codes to predict the plasma effect on complex flows around various geometries. However, there is some ambiguity in measuring these characteristics. For example, the induced jet velocity is not constant across the flow, which means that one should measure the entire velocity profile.

Since the integrated momentum flux (or thrust) of the jet should be affected by viscous friction, the velocity profile should be measured immediately downstream of the plasma, and, given that the discharge thickness is less that one millimeter, such measurements are very difficult to perform with an acceptable spatial resolution. Thrust measurements also have some disadvantages. It has been shown that most of the momentum coupled to the air can be lost in a relatively short distance due to wall friction [69, 70]. The losses are not the same in all experiments and depend on the streamwise wall length and thickness of the jet. Thus, for a better insight

into the DBD actuator induced flow and thrust and for correct interpretation of the experimental measurements, a deeper understanding of the plasma induced wall jets and their dynamics is required. In this chapter, we use a wall jet model that permits self-similar analytical solution outside the plasma. We validate the analytical models applicability by comparison of the predictions with experimental measurements of the DBD induced flow.

6.1 Analytical model

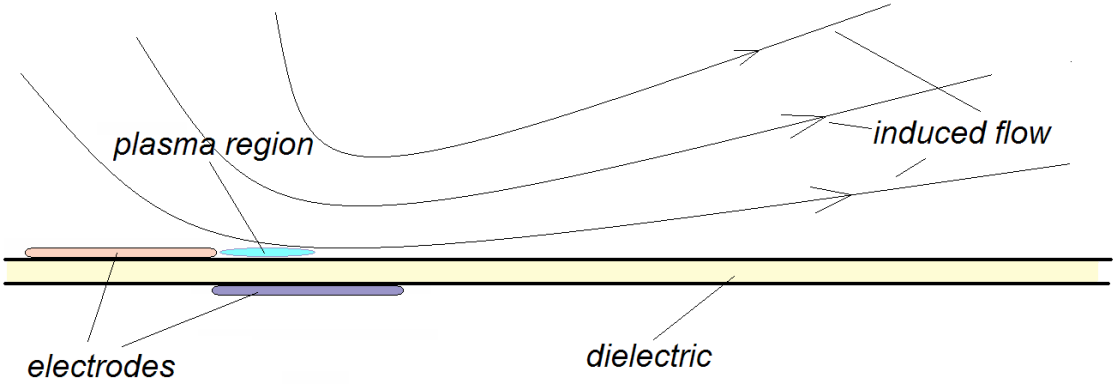

Figure 6.1: DBD plasma actuator and the induced flow.

Numerous thrust and pressure measurements and experiments on visualization of DBD induced flows in quiescent air revealed the ability of plasma to impart momentum to the gas while producing only a slight heating [65]. This momentum coupling produces steady laminar jets usually up to 1 cm thick, much thicker than the original plasma (∼100 micron), observed centimeters and even tens of centimeters downstream, Figure 6.1. To describe the gas flow after it leaves the plasma region, where no body forces are present, we make the following assumptions: (1) the air is originally quiescent and without body forces and pressure gradients, (2) the problem is two- imensional, (3) the flow is incompressible, and (4) the flow is steady. With

these reasonable assumptions, the problem is reduced to the wall jet problem that admits an analytical self-similar solution in the boundary layer approximation. The solution has been found by Akantov, [71] and Glauert, [72]. We will not repeat the derivation, referring the reader instead to the original papers or textbooks (see, for example [73]).

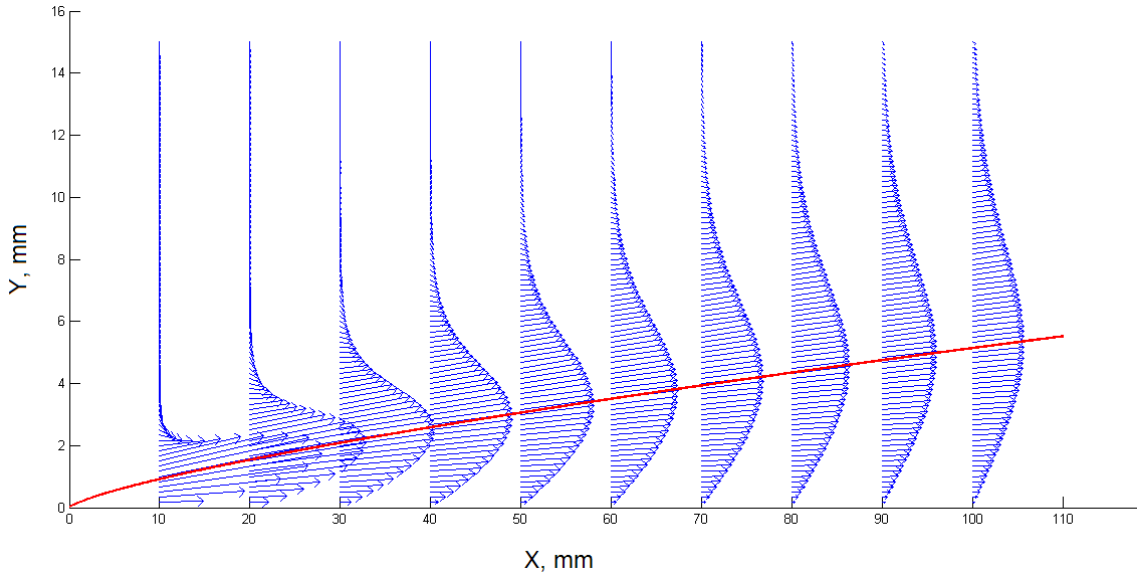

Figure 6.2: Typical flow field produced by a wall jet. X – distance downstream along the wall, Y – distance from the wall. Jet parameter E = 6.38× 10^{-7} m^5/s^2.

A typical flow field produced by the wall jet is shown in Figure 6.2. The red curve shows the thickness of the jet which is defined here as the distance from the wall to the maximum horizontal velocity component of the cross section. Since the boundary layer equations are of parabolic type, the velocity distribution at any cross section completely defines the flow field downstream. The jet expands and slows down with the distance; it thickens as it involves more mass into motion and loses its momentum due to friction at the wall. Similarly, it is possible to formally extrapolate the solution upstream until the jet collapses into a virtual point source at the wall. At that virtual point its total momentum and maximum velocity, as well as the friction

force, diverge. It follows from the self-similar solution [73] that the only parameter which fully characterizes the jet and is conserved at any cross section downstream is a product of the volumetric flux rate $\left(\int_0^\infty u dy\right)$ and the specific momentum flux $\left(\int_0^\infty u^2 dy\right)$

$$E = 0.45 \int_0^\infty u dy \int_0^\infty u^2 dy \tag{6.1}$$

The flow field (u,v) can be expressed through the stream function ψ:

$$u = \frac{\partial \psi}{\partial y} \qquad\qquad v = -\frac{\partial \psi}{\partial x} \tag{6.2}$$

$$u = \sqrt[4]{40 \nu E x}\ \theta(x, y) \tag{6.3}$$

where ν is the kinematic viscosity and the function $\Theta(x, y)$ is found from the following equation [73]:

$$\frac{2}{\sqrt[4]{40}} \left[\ln \frac{1 + \sqrt{\theta} + \theta}{(1 - \sqrt{\theta})^2} + 2\sqrt{3} \arctan \frac{\sqrt{3\theta}}{\sqrt{\theta} + 2} \right] = \sqrt[4]{\frac{E}{\nu^3}} \frac{y}{\sqrt[4]{x^3}} \tag{6.4}$$

Although Equation (6.4) does not permit analytic solution, the function $\theta(x, y)$ can be found from Equation (6.4) numerically. Once $\theta(x, y)$ is found, one can calculate the stream function from Equation (6.3) and the flow field from Equation (6.2).

As mentioned above, the jet is completely characterized by the E parameter. Along with the fluid kinematic viscosity ν , it determines the entire flow field. The principal flow characteristics as a function of the distance along the wall can be found analytically,

$$Q(x) = \int_0^\infty u\ dy \cong 2.5149 (\nu E x)^{1/4} \tag{6.5}$$

$$K(x) = \rho \int_0^\infty u^2 \, dy \cong 0.8836 \frac{\rho E^{3/4}}{\nu^{1/4} x^{1/4}} \tag{6.6}$$

$$\tau(x) = \frac{\partial K}{\partial x} \cong -0.2209 \frac{\rho E^{3/4}}{\nu^{1/4} x^{5/4}} \tag{6.7}$$

$$u_{max} \cong 0.4980 \left(\frac{E}{\nu x} \right)^{1/2} \tag{6.8}$$

$$y_{u_{max}} \cong 3.2265 \frac{\nu^{3/4} x^{3/4}}{E^{1/4}} \tag{6.9}$$

It is important to recognize that the distance x in the formulas (6.5)-(6.9) is measured from the hypothetical jets point of origin, where its thickness is zero, and not from the plasma where the jet is actually created. These relationships not only provide a clear understanding of the wall jet dynamics, but also enable one to restore the entire flow field from a velocity profile u(y) measured at a single location x. By measuring any two values out of the five (6.5)-(6.9), one can find the jet parameter E and distance to the jets point of origin x . This significantly reduces the number of measurements and complexity of the experiment required to obtain the entire flow field.

In the papers by Hoskinson et al. [26] and by Little et al. [68] the authors used an empirical fit to the selfsimilar DBD induced flow velocity profile,

$$v_{fit} = v_0 \sqrt{y} \exp \left[- \left(\frac{y - y_0}{L} \right)^2 \right] \tag{6.10}$$

where v_0, y_0, and L are adjustable parameters. Figure 6.3 shows comparison of the two wall jets velocity profiles, one obtained from the analytical model (the jet parameter is E = 6.38$\times$ 10^{-7} m^5/s^2, distance from the point of origin x = 8 mm) and the other being its least square fit by an empirical functional form of Equation

(6.10) (v_0 = 0.172 m/s, y_0 = 3.344 mm, L = 4.653 mm). It can be seen from the plot that the convenient functional form (6.10) can indeed approximate the actual analytical similarity solution closely. However, it is important to distinguish between our analytical theory that generates a full flow field and the empirical approximation (6.10).

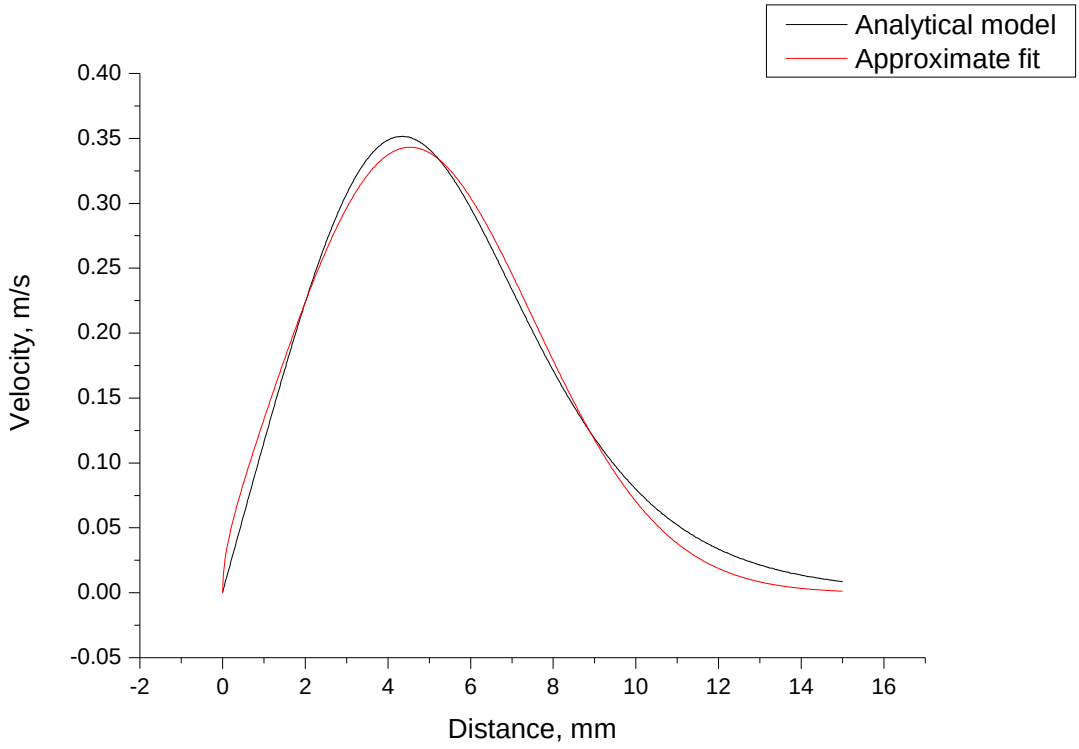

Figure 6.3: Wall jet velocity profiles, analytical model and approximate fit.

6.2 Experimental setup

The applicability of the analytical model of the wall jet to surface plasma induced flows was verified experimentally. A schematic of the setup is shown in Figure 6.4. A 0.8 mm thick pitot probe mounted on a step motor was used to measure the flow

induced by a DBD plasma actuator. The actuator was made of 1/16 MACOR plate and 100 micron thick 5 by 1 copper electrodes. The actuator was driven by a sinusoidal 12 kV peak-to-peak 5 kHz voltage profile. SETRA-339 electronic manometer was used to take dynamics pressure readings. Overall 100 readings were taken during each scan of 15 mm. Each profile was scanned four times and then averaged and filtered out from the noise.

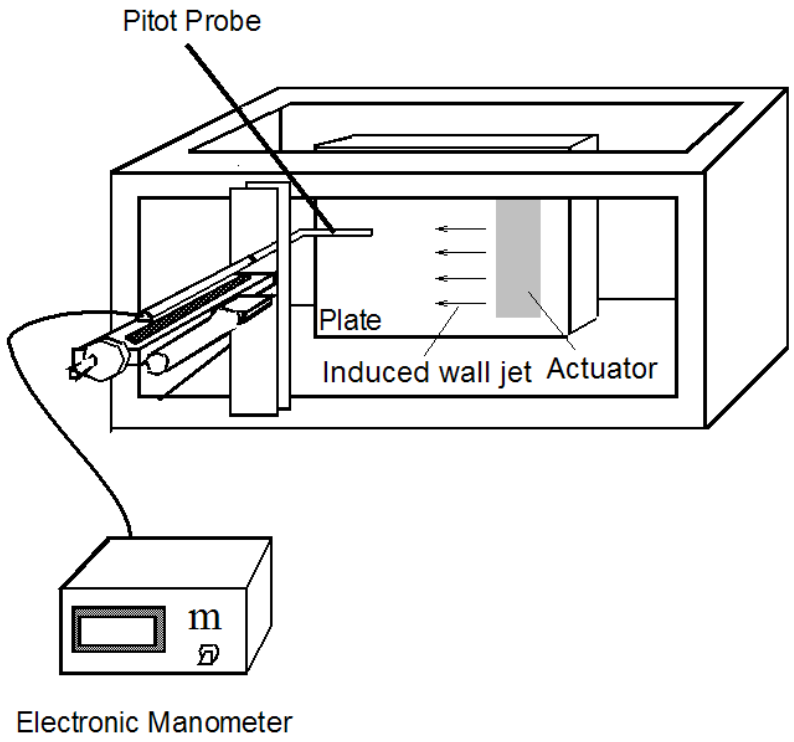

Figure 6.4: Experimental setup for Pitot probe measurements of DBD induced wall jet.

6.3 Results and discussion

Figure 6.5 shows experimentally measured dynamic pressure profiles and their comparison to the analytical model. In this particular case, the analytical solution was

built based on the momentum flux and maximum velocity at the 30 mm profiles, i.e. the entire flow field was extrapolated from this single streamwise location. The comparison demonstrates an excellent agreement and confirms the ability of the model to predict plasma induced wall jets. Note that the distance in the plot is measured from the electrode edge, and the jets virtual point of origin is located 4 mm upstream of that real origin.

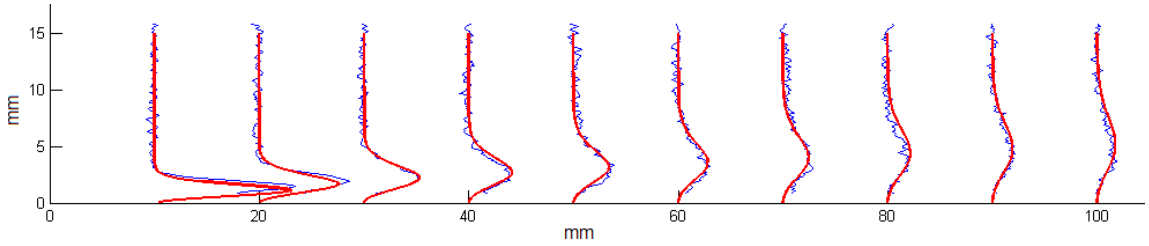

Figure 6.5: Experimental (blue) and analytical (red) dynamic pressure profiles. X distance downstream from the electrodes edge, Y distance from the wall. Jets parameter E=6.44× 10^{-7} m^5/s^2.

The maximum velocity and momentum flux as functions of the streamwise distance are presented in Figure 6.6. The experimentally measured maximum velocity in all streamwise locations is in excellent agreement with the analytical model. As expected, its value decreases as the inverse square root of the distance from the jets virtual point of origin. The calculated and measured momentum fluxes are also in good agreement; however, the measured flux exhibits a significant noise, particularly at large distances downstream from the plasma. This occurs probably due to the fact that the jet expands and partially leaves the region of consideration, thus leaving a part of the momentum flux not included into integration.

For both cases it is possible to extrapolate the analytical solution upstream to the electrode edge (x=0 in Figure 6.6). As we can see, the jet velocity at this point is almost twice that measured 1 cm downstream. The momentum flux also loses half of its value over the first 2 cm and 70% by the time the jet reaches the end of the

plate. These losses are due to the viscous friction after the gas element has left the plasma region and do not include the friction losses in the plasma itself. Therefore, the total losses due to viscous friction are even higher. One consequence is that the force balance measurement of plasma induced thrust show values that are significantly lower than the plasma produced body force. A similar conclusion has been reached by Font et al. in [70] based on results of numerical Navier-Stokes simulation. Note that the momentum losses may vary in different experiments and depend on the jet thickness, velocity, and length of the plate.

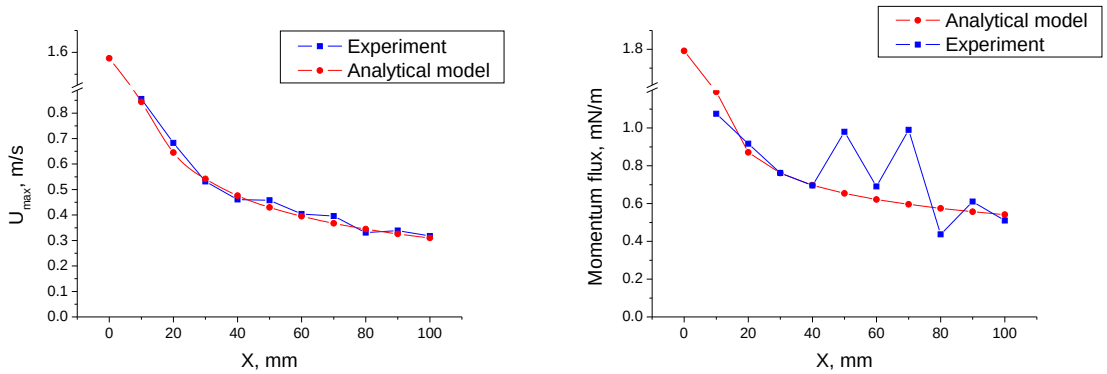

Figure 6.6: *a)* Experimental and analytical maximum velocity of the wall jet. *b)* Experimental and analytical momentum flux of the wall jet. X – distance from the electrode edge.

6.4 Summary

In this Chapter, we studied the surface plasma induced flow using analytical self-similar solution for the wall jet problem. The plasma induced flows in quiescent air can be presented as wall jets that originate from a single point at the wall and are characterized by a single jet parameter number E which is equal to the product of flow rate and momentum flux and is conserved at any cross section downstream. It was

demonstrated that the entire induced flow field can be restored from a velocity profile measured at a single streamwise location. Even though the exact analytical expression for a velocity profile cannot be found, a simple near-Gaussian fit gives a very close approximation. Analytical expressions for the most important plasma induced flows characteristics, such as flow rate, momentum flux, jet thickness, maximum velocity and wall friction, were found. The analytical models applicability to the DBD induced flow has been verified experimentally. The calculations and measurements showed that after the jet leaves the plasma region a significant part (fifty percent in the considered case) of its momentum and velocity is lost due to viscous friction in the first 1-2 cm downstream of the plasma.

Chapter 7

Electrodynamic Effects in Nanosecond Pulse Sustained Long DBD Plasma Actuators

7.1 Motivation

The most promising prospective application of the asymmetric dielectric barrier discharge DBD plasma actuator is flow control over an airfoil, [4, 74, 75, 54]. A number of both numerical [76, 77] and experimental [30, 65, 78] works have demonstrated the effectiveness of nanosecond, high voltage pulse sustained DBDs in achieving improved performance for the generation of surface flow for control authority. While these pulse sustained devices have worked well for laboratory size models tens of centimeters in spanwise direction important issues arise when it comes to scaling the pulse sustained actuator to the practical airfoil sizes several meters spanwise.

If the actuator is extended across a wing its size may become comparable with physical length of the high voltage pulse or to the wavelength of the applied rf voltage

if the actuator discharge is sustained by a rf generator. In such case the electrodes cannot be considered equipotential anymore and the wave nature of the electromagnetic signal propagating along the long line of the actuator must be taken into account. This effect can lead to variations in the voltage along the actuator, voltage doubling at the end, nonoptimized power coupling into the actuator, and ringing due to mismatched impedance of the cable and the actuator. The nonuniform voltage distribution across electrodes was observed for the first time in rf driven CO_2 lasers of slab geometry by Lapucci et al.[79]. Theory of the phenomenon was later developed by Raizer and Shneider in [80]. Later a similar problem was studied for large-area rf plasma chemical reactors by Lieberman et al in [81].

7.2 Long DBD plasma actuator

The plasma actuator used for this study was 2.4 m long and was connected to the pulse generator at one end, as shown in Figure 7.1. The electrodes were made of copper foil. The width and thickness of the electrodes were 25 mm and 100 μm, respectively, which resulted in resistance R = 1.34×10^2 Ω m^{-1}. A 100 μm thick kapton tape was used as the dielectric. The actuators capacitance was measured experimentally using a Fluke 189 multimeter and found to be C=127 pF m^{-1}. Its inductance was found to be L = 0.178 H m^{-1} by measuring the pulse propagation speed v=2.1×10^8 m s^{-1} in the actuator and using the expression v=1/LC. The impedance of the actuator can be found from the expression $Z_{actuator}$=L/C=37 Ω. The voltage was monitored with PP005A 500 MHz LeCroy voltage probe connected to WavePro 7300A 3GHz LeCroy oscilloscope.

The experiments were conducted for low and high voltage pulses. The low voltage pulses were used to measure the pulse propagation speed in the absence of the plasma, which may introduce significant dissipation. A Stanford Research Systems pulse

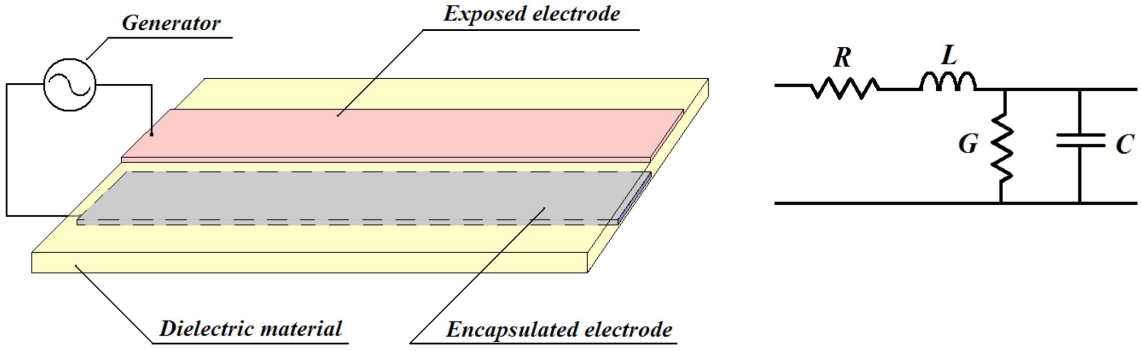

Figure 7.1: DBD plasma actuator *a)* and schematic representation of its elementary components *b)*.

generator was used as a source and the pulses were applied to one end of the actuator through a 50 Ω cable. High voltage pulses of negative polarity were used to ignite the plasma and observe the visible appearance of the discharge. These pulses were generated by FPG 25200MC4 pulser by FID Technology. The pulse profiles are shown in Figure 7.2.

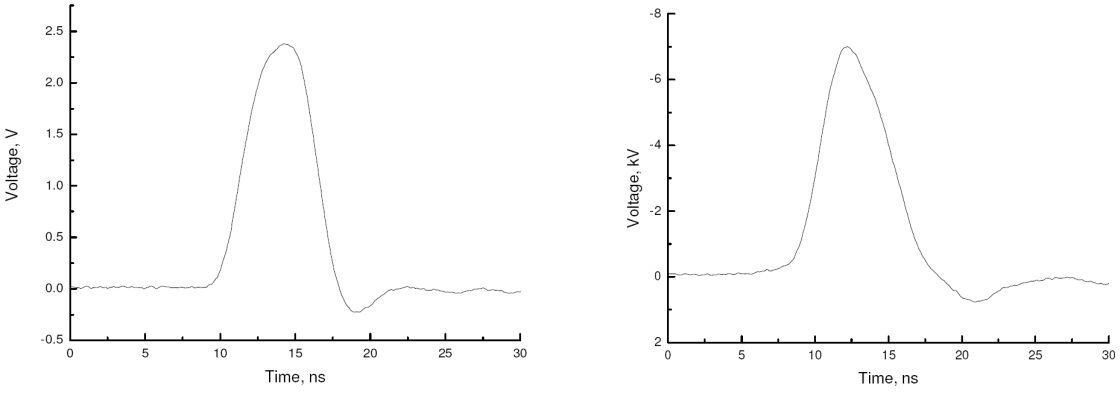

Figure 7.2: Low *a)* and high *b)* voltage pulse profiles.

7.3 Numerical model

The signal propagation in a long line is described by telegraph equations,

$$C\frac{\partial u}{\partial t} + Gu + \frac{\partial i}{\partial x} = 0 \tag{7.1}$$

$$L\frac{\partial i}{\partial t} + Ri + \frac{\partial u}{\partial x} = 0 \tag{7.2}$$

where u and i are voltage and current; L, C, G, and R are the impedance parameters specified per unit length – inductance, capacitance, leakage conductance, and resistance correspondingly. The values of the impedance parameters were taken from the experiment and are specified above. The leakage conductance was considered to be negligibly low.

A numerical code has been developed to solve the set of telegraph (7.1) and (7.2) using a second order Lax–Wendroff method coupled with Flux Corrected Transport technique, [82, 83, 84].

Proper boundary conditions for forward and reversed waves (see for instance [85]) were imposed at the cable/actuator connection point as well as at the end of actuator open circuit. The code allows simulation of the actuator with an arbitrary active noninductive resistor or reactive inductor, capacitor load at the end.

7.4 Results and discussion

Results of both numerical simulation and experimental measurements of the low voltage nanosecond pulse in the long plasma actuator are presented in Figure 7.2. The diagrams show the time evolution of the voltage distribution along the actuator. Negative values of the distance correspond to the voltage in the connecting cable. The finite capacitance, 11 pF, of the voltage probe caused the small amount of pulse broadening seen in the comparison of the modeled voltage left with the measured voltage right.

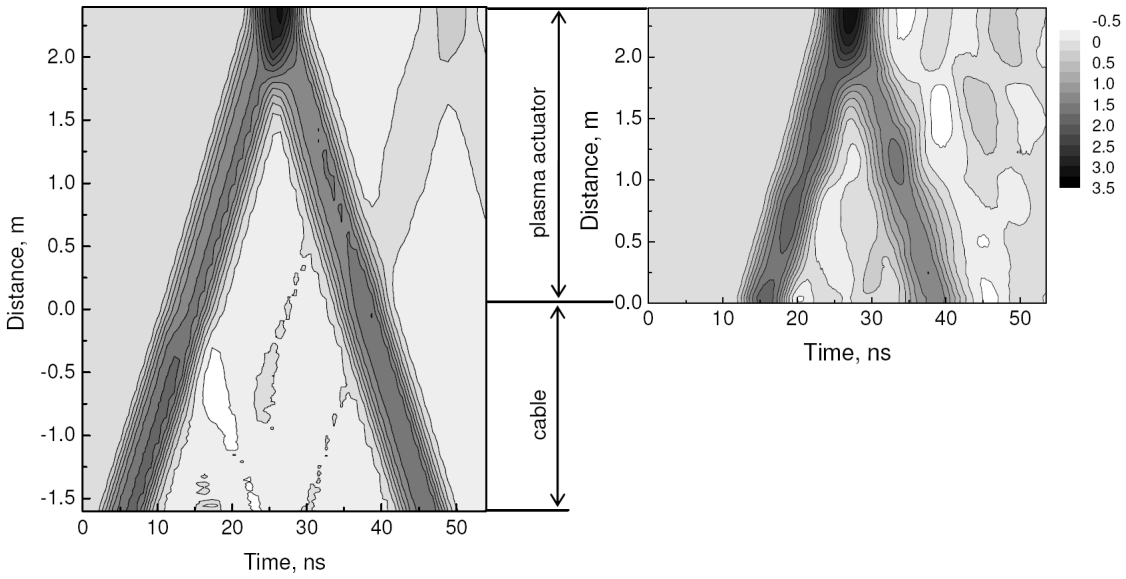

Figure 7.3: Pulse propagation along the actuator. Numerical *a)*, experimental *b)*.

Several phenomena characteristics of long lines can be recognized in these diagrams, Figure 7.3. First of all, the voltage distribution is not uniform along the electrodes. To demonstrate the result better the voltage distribution along the actuator at time t = 20 ns is shown at Figure 7.4 *a)*. Second, the pulse doubles at the end of the actuator which we expect to happen with a high impedance load. This leads to nonuniform discharge parameters along the actuator.

Also the impedance matching of the connecting cable and the DBD actuator is important. The mismatch leads to poor power coupling from the cable to the actuator as can be seen from the modeling. In this particular case the impedances have values which are close Z_{cable}=50 Ω and $Z_{actuator}$=37 Ω so the effect is not particularly strong, but it is still observable. Similarly, a part of the pulse reflects on its way back to the cable which creates a ringing effect, which can be seen most clearly in the model results at Figure 7.3 *a)* and Figure 7.4 *b)*. By choosing the proper dimensions and dielectric constant, the actuator could be designed in a way to match the cable impedance. It means that pulse would be transferred from the cable to the actuator and back

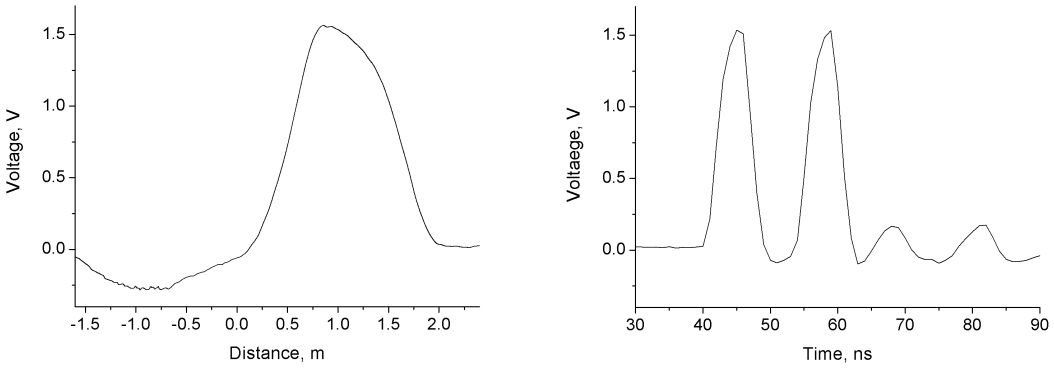

Figure 7.4: Electrodynamic effects in long DBD plasma actuators. *a)* nonuniform potential distribution, voltage disctribution along the actuator at t = 20 ns; *b)* ringing effect, voltage profile vs. time at x = 1.1 m.

without any distortion and losses, so there would not be any ringing effect or poor power coupling. The finite conductivity of the electrodes did not play a significant role in the pulse propagation. The effect of the various boundary condition on the pulse propagation was studied numerically.

7.5 Visual plasma appearance

Experiments with the high voltage nanosecond pulses were conducted in order to observe the plasma nonuniformity visually. The pictures of the discharge at different pulse voltages are shown in Figure 7.5. The top left picture, Figure 7.5*a)*, corresponds to the pulse voltage slightly below the breakdown value. In this case, the pulse travels along the actuator without ingiting the discharge until it hits the open circuit at the far end where the pulse voltage doubles and the discharge is initiated. In the second picture, Figure 7.5*b)*, the pulse voltage is higher than the breakdown value and the discharge ignites along the whole length of the actuator. The image in Figure 7.5*c)*, which is the top view of Figure 7.5*a)*, shows the nonuniformity of the discharge, which

becomes brighter and wider toward the end of the actuator. The size of the discharge is in agreement with the numerical simulation and equals to a half of the pulse length in the actuator. Gaps in the discharge are due to local variations in the electrode edges.

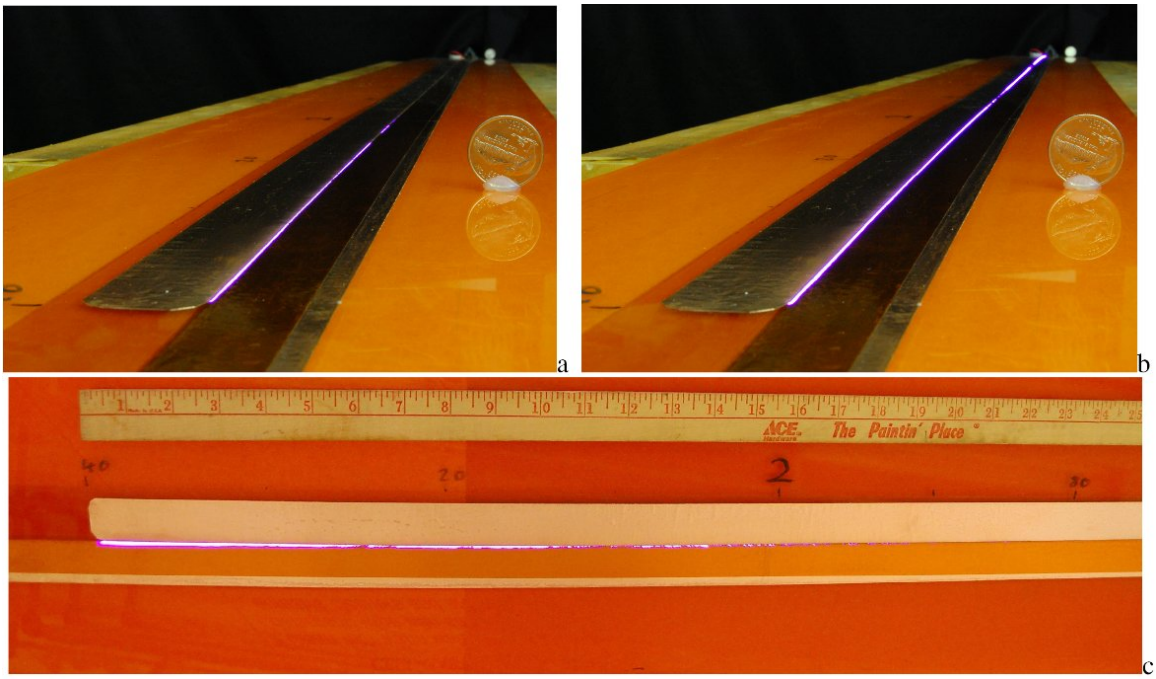

Figure 7.5: Images of DBD at different voltages. *a)* low voltage, *b)* high voltage, *c)* low voltage seen from above.

7.6 Summary

Experiments on the nonuniformity of the pulse voltage distribution in a long DBD plasma actuator have been conducted. Images of the discharge appearance have been taken and direct voltage distribution measurements have been made. The images demonstrate the discharge nonuniformity. Numerical modeling of short pulse propagation in long lines has also been performed and agreement between the experimental

and the simulated voltage distribution was obtained. The results show the importance of the wave nature of pulse propagation. This leads to a nonuniform potential distribution along the electrodes, a doubling of the pulse voltage, at the end of the actuator, nonoptimized power coupling, ringing effects, etc.

Chapter 8

Ozone Visualization

Dielectric barrier discharges are well known sources of ozone. This type of discharge is widely used in commercial ozonators. Its effectiveness is due to high non-equilibrium of the plasma; the electron temperature reaches values of several electron volts whereas heavy particles stay at the room temperature. It allows efficient oxygen dissociation by electron impact followed by formation of ozone from O and O_2. DBD plasma actuators for flow control, both pulsed and driven by ac voltage, also produce a significant amount of ozone.

Ozone in the lower atmosphere is an air pollutant with harmful effects on the respiratory systems of animals and will burn sensitive plants, it also causes smog and greenhouse effect; however, the ozone layer in the upper atmosphere is beneficial, preventing potentially damaging ultraviolet light from reaching the Earth's surface. In addition to a possible effect of the produced ozone on the environment, the ozone production needs a special study due to its effect on combustion processes (if DBD is used in turbine engines), personnel safety during lab testings, and its possible use for flow visualization. The visualization is based on the strong absorption band of ozone around 254 nm, [86, 17, 87] and was first demonstrated by Dickerson and Stedman [88]. The advantage of this technique is that the flow is seeded with the

ozone naturally and no additional seeding is required. It perfectly suits for purpose of boundary layer visualization.

The diagram of the setup is shown in Figure 8.1. A mercury lamp illuminates the actuator from a side; the light is collected by a UV lens, goes through a notch filter, and the backlit actuator is imaged by a CCD camera.

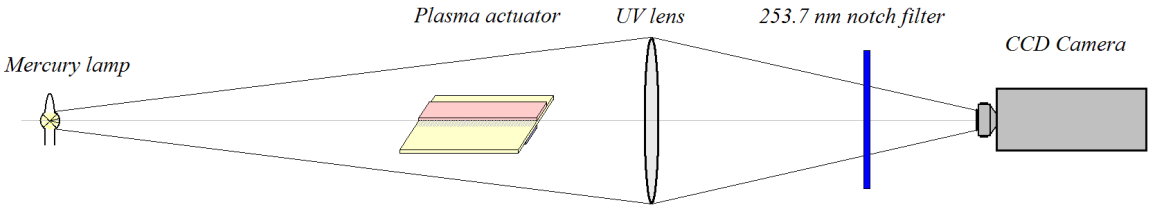

Figure 8.1: Experimental setup (not to scale).

If there is ozone, it produces a shadow by absorbing the light at 253.7 nm. The image of the shadow is then captured by the camera. Based on the absorption intensity, ozone concentration can be found from Beers Law,

$$\frac{I_{ozone} - I_b}{I_0 - I_b} = \exp(-\sigma L n) \tag{8.1}$$

or,

$$n = \frac{1}{\sigma L} \ln \frac{I_{ozone} - I_b}{I_0 - I_b} \tag{8.2}$$

where I_{ozone} – intensity with the actuator ON, I_0 – intensity with the actuator OFF, I_b – background intensity, with the lamp OFF, L = 75 mm – integration length, $\sigma = 1.13 \times 10^{-17}$ cm^2 – ozone absorption cross section.

Figure 8.2 presents the ozone absorption cross section, taken from [17], and the mercury lamp spectrum after the 253.7 nm notch filter. It can be seen that the absorption is almost constant across the mercury line.

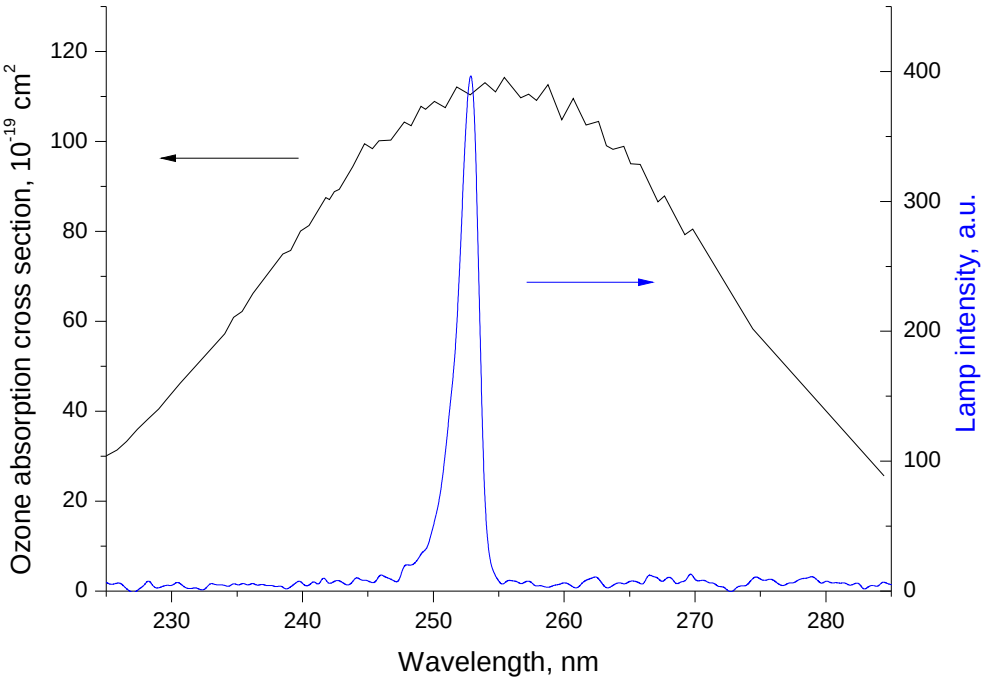

Figure 8.2: Ozone cross section (from [17]) and mercury lamp spectrum.

In each run, the camera took ten frames during several seconds, which were averaged to increase signal-to-noise ratio. The exposure time of each frame was equal to one millisecond. The experiments on ozone visualization were conducted using 3 mm thick, linen based phenolic DBD plasmas actuator. This actuator was chosen because it produced a steady jet, which is convenient for preliminary experiments. The actuator was driven by 17 ns FWHM 7 kV negative pulses at different repetition rates added to 6 kV positive dc bias voltage. The images shown at Figure 8.3, present the results. Pictures on the left are unprocessed images of the ozone shadow. Pictures on the right are ozone concentration distribution in cm^{-3}. Dimensions are given in mm. The point of origin is at the electrode edge.

It can be seen that this visualization technique clearly shows the location of the

jet and provides quantitative ozone concentration measurements, which are on the order of 10^{16} cm^{-3}. The concentration of the ozone increases with the PRR, and the jet speed does as well. The ozone production, which is proportional to both of these quantities, goes up significantly.

On the shadow pictures, one can notice a bright line above the plasma region. A

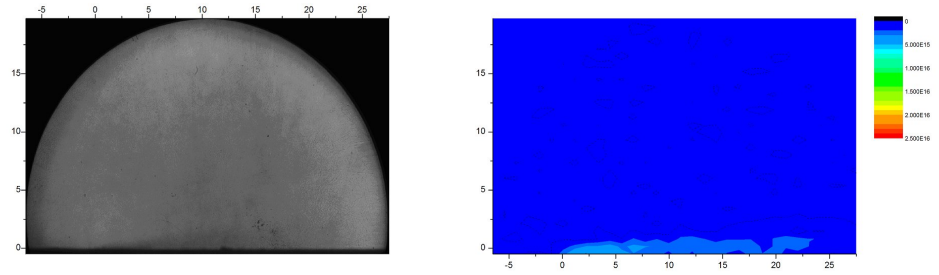

1 kHz

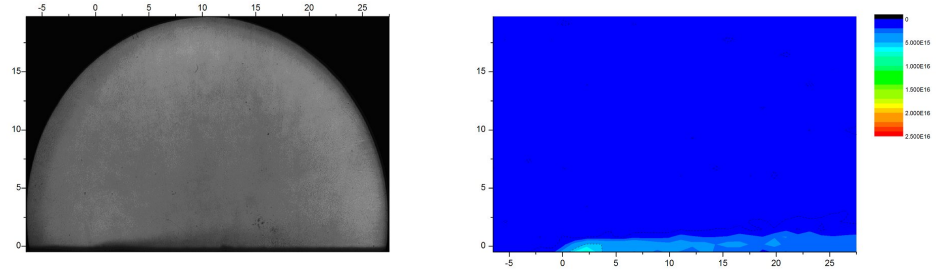

2 kHz

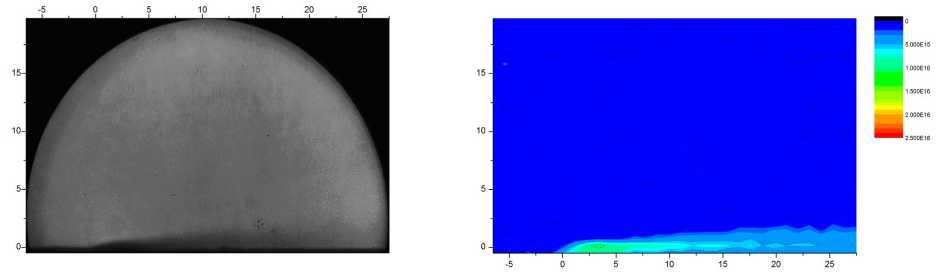

5 kHz

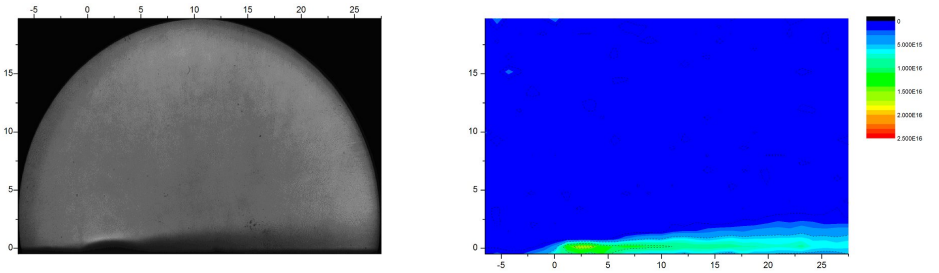

10 kHz

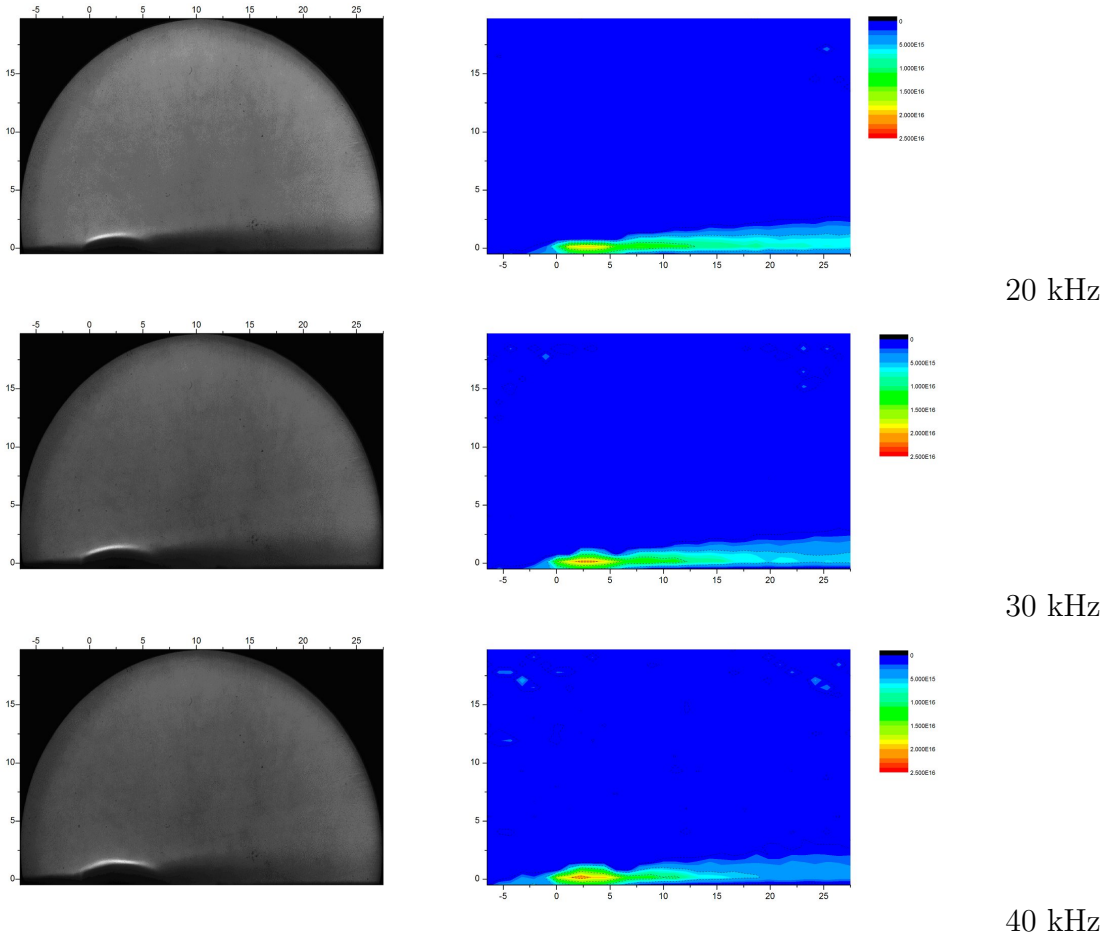

Figure 8.3: Ozone visualization of DBD induced flow at different pulse frequencies. Left – original image of ozone absorption, right – post processed image of ozone distribution.

set of experiments was performed in order to establish the origin of that line. First, it was checked to determine if the light comes from the plasma. To do that the lamp was turned off and a picture was taken with the plasma on. No line was observed. Then we changed the color filter in front of the camera to a yellow one. In this case, no ozone could be observed and the bright line was still there. Based on this, it can be concluded that a lensing effect takes place and the light is refracted as it passes close to the discharge in a strong density gradient. It means that the ozone concentration

measurements in the immediate proximity to plasma are not very accurate.

Nevertheless, it is possible to use the obtained data to estimate ozone production DBD plasma actuators. Ozone concentration downstream the discharge, where the readings are not affected by the lensing effect, is $\sim 10^{16}$ cm^{-3}. Jet velocity at that location is around 1 m/s and its thickness equals to 2 mm. It can calculated that ozone production rate is about 1.6 mg/sec per one meter of DBD length.

In 2010, US Environmental Protection Agency set a limit for ground level ozone as 0.075 ppm (or 0.16 ng/cm^3) for 8-hour averaging time, [89]. This means that one meter long DBD pollutes 10 m^3 of air per second. According to Stevenson et al [90], the tropospheric ozone lifetime equals to 22 days. This means that ozone production should be taken into account when the plasma actuators are implemented for use.

Another observation can be made about rate of production of the ozone. First, as the pulse frequency increases, the ozone concentration goes up. But starting from 20 kHz increase in pulse repetition rate leads to a lower concentration of the ozone in the jet. As we know from thrust stand experiments, the jet speed saturates at these values of pulse frequency, so the decline in the ozone concentration cannot be explained by the increase of the jet velocity. Indeed, the ozone production decreases. However, the lensing effect in the discharge region becomes stronger which means higher temperatures. It is known that the ozone is destructed by heat and that is what is observed here. This suggests one of the solution to excessive ozone production – thermal destruction.

Also, if the camera is able to take high repetition rate consecutive images, this method can be used for visualization of unsteady flows and velocity measurements by correlation of sequential images.

Chapter 9

Conclusions

9.1 Overview

It was the goal of this dissertation to gain a through understanding of dielectric barrier discharge plasma actuation for flow control applications. The driving voltage profile consisted of two parts, each serving its own function. Short pulses were responsible for ionization production, while the bias component provided an electric field to act on the produced charged particles between the pulses. Based on the performed studies it can be concluded that the force production in DBD plasma actuators occurs by means of ion wind. The electric breakdowns, though capable of producing high instantaneous forces, last for very short time (about 10 ns) and thus do not contribute significantly to the total transfered momentum. The residual ions driven by the bias voltage transfer momentum to the neutral gas over microseconds. In the case of ions, the lower force is compensated by longer interaction time, so the total transfered momentum is significantly higher than for electrons during the breakdowns. Surface charge deposited by the ions shields the bias voltage thus reducing the performance of the actuator. Four configurations were suggested in this work to mitigate the effect. Scaling of the thrust with the bias voltage, pulse repetition rate, and pulse voltage

was similar in every case. Indeed, the force production mechanism was identical – ion wind, the different configuration just provided different ways of the depleting the surface charge.

Resolving the structure of the DBD induced flow demonstrates the importance of the viscous losses. In addition to the impact it may have on practical applications, it also means that induced velocity or thrust are not good enough metrics for DBD characterization. The induced flow is better described by the velocity profile and distance to point of origin. Some factors, such as air humidity, have a strong impact on the overall DBD performance and can lead to discrepancy in the obtained data as high as 25% on day-to-day basis.

9.2 Summary of findings

The use of dielectric barrier discharges for flow control has been the focus of a wide range of recent studies [4]. The conventional plasma actuator is driven by a sinusoidal voltage waveform at a frequency of 1-20 kHz and amplitude of up to 30 kV. In this dissertation, it was proposed to use what is essentially non-self-sustained discharge: the plasma is generated by repetitive short pulses, and the pushing of the gas occurs primarily due to the low-frequency (bias) voltage. The advantage of this non-self-sustained discharge is that the parameters of ionizing pulses and the driving bias voltage can be varied independently, which adds flexibility to control and optimization of the actuator performance. It has been also shown that the voltage waveform consisting of short nanosecond pulses added to a low frequency or DC bias voltage is more efficient.

We have used a burst mode of plasma actuator operation in conjunction with non-intrusive schlieren diagnostic of the actuator induced flows in quiescent gas. With this technique, the DBD actuator was observed to generate periodic pulsed wall jets

that evolve into vortices, and parametric studies of the vortex speed and size versus parameters of the waveform (pulses in repetitive-burst mode plus dc or ac bias voltage) were performed. Matching 2-D numerical fluid modeling to the experimental results allowed us to infer the magnitude of plasma-generated body force exerted on the gas. The knowledge of the body force magnitude can then be used to compute the entire flow field in both burst and continuous modes of plasma actuator operation.

Surface potential measurements have revealed that during the operation of both the conventional and the pulse sustained DBD, performance is significantly reduced due to charge that builds up on the dielectric surface. The surface charge builds up quickly (with a few pulses), extends far downstream of the discharge region, and depletes slowly. For pulse sustained, dc driven discharges, this charge opposes the applied dc bias voltage. Several solutions for this problem have been suggested and proven to be effective. In the first approach, switching the polarity of the bias voltage periodically leads to alternate depletion and recharging the dielectric with the charges of the opposite signs. This approach is quite effective at eliminating the charge buildup problem, but it requires relatively sophisticated equipment and suffers a loss in thrust from the reduced duty cycle compared to the DC bias case. In the second approach to the charge buildup problem, since the plasma is only a few millimeters long and the charge builds up centimeters away, placing a third electrode downstream allows the depletion of the charge in the area and thus a reduction in the overall charge buildup. This case is relatively simple but there is a substantial probability of a spark across the dielectric to the third electrode. In the third approach, to avoid the spark we are exploring the use of a high, but finite resistance dielectric that depletes the surface charge between the pulses. This method also turns out to be quite effective but imposes limitations on the materials which can be used for the dielectric layer due to the resistance requirements. In the fourth approach, as

an alternative to the conducting dielectric, we are using a slightly conductive thin silicon coating applied on top of the dielectric layer and electrically connected to a covered surface electrode, which, in turn, is connected to the buried electrode. This approach bleeds the charge away from the surface to the covered electrode and allows use of any dielectric substrate. It also has the advantage of operating in a corona mode with only a DC applied voltage. This DBD can be operated with or without a buried electrode, and the covered surface electrode can be separate or connected to the buried electrode.

Thrust measurements demonstrated higher performance of the proposed pulsed DBD configurations than of the sinusoidal ones. When the pulsed DBD configurations are compared to each other, scaling with pulse voltage and repetition rate, bias voltage, is similar. Indeed, the force production mechanism is the same in all cases – ions drift from the discharge region to the surface of the dielectric through the neutral gas in the bias electric field. It is the way the ions are produced and depleted from the dielectric makes the difference. Separating the ionization pulses from the pushing bias voltage – that is what gives the pulsed DBDs their advantage over the sinusoidal ones.

Pitot probe measurements showed the laminar wall jet structure of the DBD induced flow. An analytical model shows that the entire flow field can be established from a velocity profile measured at a single cross section, which greatly simplifies the diagnostic. It showed that the DBD induced jet can be described using two parameters – the jet's parameter (which is proportional to product of volumetric flux and momentum flux) and distance to the point of origin – and allows simple comparison of the induced jets. In contrast, both the experiments and the analytical model have shown that the maximum velocity and the induced thrust, widely used to characterize the DBD performance, are heavily affected by the viscous losses to the

wall and not constant. Results of their measurements should be used only as a rough estimate of the actuator's performance.

The use of ozone for visualization of the DBD plasma induced flow has been demonstrated. The ozone is produced by the plasma and is present in the jet naturally. Therefore, this method does not require any artificial seeding. In addition, quantitative measurements of ozone concentration and production rate were performed. Since high levels of ozone are harmful to humans and the environment, it is suggested to use heat destruction to lower the production rate. On the other hand, if used in turbine engines, the production of ozone may be beneficial for combustion process.

If the actuator is scaled up to wing span size, the electrodynamic effects can become important. Experiments on the nonuniformity of the pulse voltage distribution in a long DBD plasma actuator have been conducted. Images of the discharge appearance have been taken and direct voltage distribution measurements have been made. The images demonstrate the discharge nonuniformity. Numerical modeling of short pulse propagation in long lines has also been performed and agreement between the experimental and the simulated voltage distribution was obtained. The results show the importance of the wave nature of pulse propagation. This results in a nonuniform potential distribution along the electrodes, a doubling of the pulse voltage, at the end of the actuator, nonoptimized power coupling, ringing effects, etc.

9.3 Future direction

While DBD plasma actuators have been proven to be effective for flow control at relatively low free stream speeds (upto 30 m/s), which corresponds to wind turbines and low speed UAVs, many practical application lie in the area of trans- and supersonic flows, for example turbine engines, commercial and military planes, etc. To extend the actuator's flow control capabilities into these regimes the research thrust should

be pointed towards the following directions:

- *Increasing the induced jet velocity.* At current configurations the DBD plasma actuator produces momentum through steady ions drift through the gas, so called ion wind or corona regime. The maximum induced velocity produced this way is limited to ∼8 m/s by the maximum electric field (breakdown, 30 kV/cm in atmospheric air) due to space charge limitations. The next step should be to explore the high velocity opportunities by going into non-steady regimes of plasma generation, where electric fields can reach above breakdown values (upto Stoletov's field, 300 kV/cm in atmospheric air).

- *Extending the thickness of the jet.* The wall jet studies show that a large portion of the induced momentum is being lost to the wall due to viscosity effects. The losses are very sensitive to the thickness of the jet. Thus an increase in the jet's thickness will not only spread the zone of the DBD's influence farther into the flow and lead to higher thrust production but also make the imparted momentum less vulnerable to the viscous losses. This may be possible to achieve by modifying the electrode configuration to repel the electric field lines from the surface so that the drifting ions penetrate deeper in the flow.

- *New opportunities for airfoils design.* DBD plasma actuators have been demonstrated to improve aerodynamic characteristics of well established airfoils which have been designed and optimized to work without any plasma assistance. It is promising to investigate what new opportunities plasma actuators can provide for airfoil design. There can be new advanced aerodynamic profiles which perform not so well without plasma compared to the traditional ones, but achieve superior performance once the plasma technology becomes available. For example, airfoils with backward facing steps, see Figure 9.1, were shown to have

higher lift than the smooth ones but in narrow range of angles of attack, see [18]. Using DBD plasma actuators may extend the range of operation and allow even more aggressive solutions.

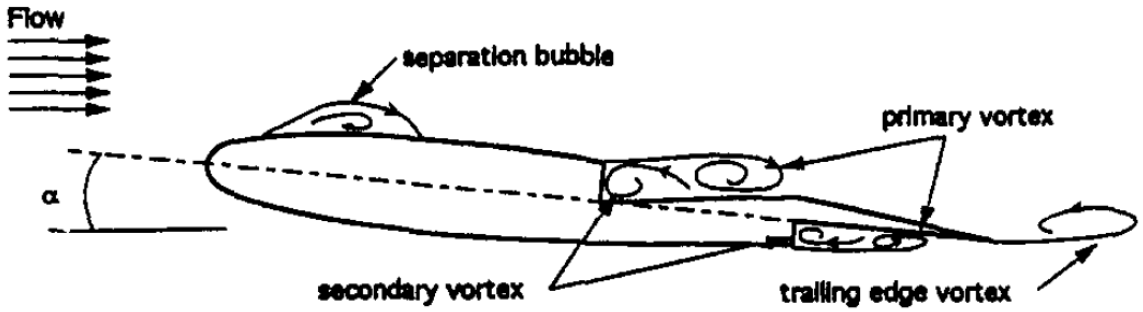

Figure 9.1: Schematic of flow development over airfoil with step, from [18].

These tasks represent a compelling body of the future research to be performed in order to improve DBD flow control.

References

[1] Sergey O. Macheret, Ronald J. Lipinski, Richard B. Miles, and Mikhail N. Shneider. Electron-Beam-Generated Plasmas in Hypersonic Magnetohydrodynamic Channels. *AIAA Journal*, 39(6):1127–1138, June 2001.

[2] Sergey O. Macheret, Richard B. Miles, and Mikhail N. Shneider. Magnetohydrodynamic Control of Hypersonic Flows and Scramjet Inlets Using Electron Beam Ionization. *AIAA Journal*, 40(1):74–81, January 2002.

[3] S.O. Macheret, R.B. Miles, and M.N. Shneider. Magnetohydrodynamic and Electrohydrodynamic Control of Hypersonic Flows of Weakly Ionized Plasmas. *AIAA Journal*, 42(7):1378–1387, July 2004.

[4] Eric Moreau. Airflow control by non-thermal plasma actuators. *Journal of Physics D: Applied Physics*, 40(3):605–636, February 2007.

[5] T.C. Corke and M.C. Post. Overview of Plasma Flow Control: Concepts, Optimization, and Applications. In *43rd AIAA Aerospace Sciences Meeting and Exhibit*, page 563, Reno, NV, 2005.

[6] J. Reece Roth. Aerodynamic flow acceleration using paraelectric and peristaltic electrohydrodynamic effects of a One Atmosphere Uniform Glow Discharge Plasma. *Physics of Plasmas*, 10(5):2117, 2003.

[7] J Reece Roth. Physics and phenomenology of plasma actuators for control of aeronautical flows. *Journal of Physics D: Applied Physics*, 40(3), February 2007.

[8] A.M. Mkhitaryan, G.N. Boyarskii, V.A. Kasyanov, and A.F. Tishkov. Experimental studies of driving voltage frequency effects on EHD CBL, 1968.

[9] J. Reece Roth, Daniel M. Sherman, and Stephen P. Wilkinson. Bondary layer flow control with a one atmosphere uniform glow discharge surface plasma. In *36th Aerospace Sciences Meeting and Exhibit*, volume 1, page 0328, December 1998.

[10] D.V. Roupassov, A.A. Nikipelov, M.M. Nudnova, and A.Yu. Starikovskii. Flow Separation Control by Plasma Actuator with Nanosecond Pulsed-Periodic Discharge. *AIAA Journal*, 47(1):168–185, January 2009.

[11] S Leonov, D Yarantsev, V Gromov, and A Kuriachy. Mechanisms of Flow Control by Near-Surface Electrical Discharge Generation. In *43rd AIAA Aerospace Sciences Meeting and Exhibit*, page 780, Reno, NV, 2005.

[12] N. Benard, N. Balcon, and E. Moreau. Electric Wind Produced by a Surface Dielectric Barrier Discharge Operating Over a Wide Range of Relative Humidity. In *47th AIAA Aerospace Sciences Meeting*, page 488, Orlando, FL, 2009.

[13] www.accuratus.com/macormats.html.

[14] DuPont. Summary of Properties for Kapton Polyimide Films.

[15] C. Porter, J. Baughn, T.E. McLaughlin, C.L. Enloe, and G.I. Font. Temporal Force Measurements on an Aerodynamic Plasma Actuator. In *44th AIAA Aerospace Sciences Meeting and Exhibit*, page 104, Reno, NV, 2006.

[16] T.C. Corke, F. Thomas, D.M. Orlov, M. Iqbal, A. Kozlov, H. Othman, and D. Shatzman. Order of Magnitude Improvement of SDBD Actuator Effect. In *DBD Plasma Actuator Workshop*, Colorado Springs, CO, 2006.

[17] J. Brion, A. Chakir, D. Daumont, J. Malicet, and C. Parisse. High-resolution laboratory absorption cross section of O3. Temperature effect. *Chemical Physics Letters*, 213(5-6):610–612, October 1993.

[18] Fathi Finaish and Stephen Witherspoon. Aerodynamic Performance of an Airfoil with Step-Induced Vortex for Lift Augmentation. *Journal of Aerospace Engineering*, 11(1):9–16, January 1998.

[19] W Siemens. Poggendorff's. *Ann. Phys. Chem*, 102:66–122, 1857.

[20] Yu.P. Raizer. *Gas discharge physics*. Springer-Verlag, 1991.

[21] John M. Meek and J. D. Craggs. *Electrical breakdown of gases*. Wiley, 1978.

[22] A Fridman, A Chirokov, and A Gutsol. Non-thermal atmospheric pressure discharges. *Journal of Physics D: Applied Physics*, 38(2):R1–R24, January 2005.

[23] J Flatt. *Boundary layer in flow control*, pages 122–143. Pergamon Press, New York, 1961.

[24] L Prandtl. Fluid motion with very small friction. *Proc. 3 Int. Congr. on Mathematics, Heidelberg*, 1904.

[25] M. Gad-el Hak. *Flow control: passive, active, and reactive flow management*. Cambridge Univ Pr, 2000.

[26] A.R. Hoskinson, N. Hershkowitz, and D.E. Ashpis. Force measurements of single and double barrier DBD plasma actuators in quiescent air. *Journal of Physics D: Applied Physics*, 41(24):245209, December 2008.

[27] A.R. Hoskinson and N. Hershkowitz. Flow Measurements and Plasma Simulations of Double and Single Barrier DBD Plasma Actuators in Quiescent Air. In *46th AIAA Aerospace Sciences Meeting and Exhibit*, page 1370, Reno, NV, 2008.

[28] A. Santhanakrishnan and J.D. Jacob. Flow Control Using Plasma Actuators and Linear/Annular Plasma Synthetic Jet Actuators. In *3rd AIAA Flow Control Conference*, page 3033, San Francisco, CA, 2006.

[29] R.D. Van Dyken, T.E. McLaughlin, and C.L. Enloe. Parametric Investigations of a Single Dielectric Barrier Plasma Actuator. In *42nd AIAA Aerospace Sciences Meeting and Exhibit*, page 846, Reno, NV, 2004.

[30] D. F. Opaits, D.V. Roupassov, S.M. Starikovskaia, A.Yu. Starikovskii, I.N. Zavialov, and S. Saddoughi. Plasma Control of Boundary Layer Using Low-Temperature Non-equilibrium Plasma of Gas Discharge. In *43rd AIAA Aerospace Sciences Meeting and Exhibit*, 2005.

[31] A.Yu. Starikovskii, A.A. Nikipelov, M.M. Nudnova, and D.V. Roupassov. SDBD plasma actuator with nanosecond pulse-periodic discharge. *Plasma Sources Science and Technology*, 18(3):034015, August 2009.

[32] J. Poggie, C. Tilmann, P. Flick, J. Silkey, B. Osborne, G. Ervin, D. Maric, S. Mangalam, and A. Mangalam. Closed-Loop Stall Control on a Morphing Airfoil Using Hot-Film Sensors and DBD Actuators. In *48th AIAA Aerospace Sciences Meeting*, page 547, Orlando, FL, 2010.

[33] M.M. Nudnova, N.L. Aleksandrov, and A.Yu. Starikovskii. Influence of the voltage polarity on the properties of a nanosecond surface barrier discharge in atmospheric-pressure air. *Plasma Physics Reports*, 36(1):90–98, February 2010.

[34] G.G. Raju. *Dielectrics in Electric Fields*. CRC Press, 2003.

[35] G.A. Mesiats, S.A. Nasibov, and V.V. Kremnev. *Formirovanie Nanosecundnih Impulsov Visokogo Napriazhenia*. Energia, Moscow, 1970.

[36] S.B. Leonov. Plasma-Assisted Aerodynamics: Approach and Problem of Measurements. In *Proceedings of FLUCOME*, Tallahassee, FL, 2007.

[37] C.L. Enloe, T.E. McLaughlin, G.I. Font, and J. Baughn. Frequency Effects on the Efficiency of the Aerodynamic Plasma Actuator. In *44th AIAA Aerospace Sciences Meeting and Exhibit*, page 166, Reno, NV, 2006.

[38] R. Sosa, E. Arnaud, and G. Artana. Schlieren Image Velocimetry applied to EHD flows. In *International Symposium on Electrohydrodonamics ISEHD*, Buenos Aires, Argentina, 2006.

[39] T. Jukes, K. Choi, G. Johnson, and S. Scott. Turbulent Drag Reduction by Surface Plasma Through Spanwise Flow Oscillation. In *3rd AIAA Flow Control Conference*, page 3693, San Francisco, CA, 2006.

[40] A.M. Konchakov, V.M. Krivtsov, S.B. Leonov, V.R. Soloviev, and D.A. Yarantsev. preprint of Institute of High Temperature RAS 2-491 (unpublished), 2006.

[41] G.I. Font, S. Jung, C.L. Enloe, T.E. McLaughlin, W. Morgan, and J. Baughn. Simulation of the Effects of Force and Heat Produced by a Plasma Actuator on Neutral Flow Evolution. In *44th AIAA Aerospace Sciences Meeting and Exhibit*, page 167, Reno, NV, 2006.

[42] M.R. Visbal and D.V. Gaitonde. Control of Vortical Flows Using Simulated Plasma Actuators. In *44th AIAA Aerospace Sciences Meeting and Exhibit*, page 505, Reno, NV, 2006.

[43] M.R. Visbal, D.V. Gaitonde, and S.P. Gogineni. Direct numerical simulation of a forced transitional plane wall jet. In *29th Fluid Dynamics Conference*, page 2643, Albuquerque, NM, 1998.

[44] S. Gogineni, M. Visbal, and C. Shih. Phase-resolved PIV measurements in a transitional plane wall jet: a numerical comparison. *Experiments in Fluids*, 27(2):126–136, July 1999.

[45] S. Gogineni, M. Visbal, and C. Shih. Experimental and numerical investigation of transitional plane-wall jet. In *Aerospace Sciences Meeting and Exhibit*, page 71, Reno, NV, 1997.

[46] G.S. Settles. *Schlieren and shadowgraph techniques: visualizing phenomena in transparent media*. Springer, 2001.

[47] A.V. Likhanskii, D.F. Opaits, M.N. Shneider, S.O. Macheret, and R.B. Miles. Numerical modeling of DBD plasma actuators and the induced air flow. In *38th AIAA Plasmadynamics and Lasers Conference In conjunction with the 16th International Conference on MHD Energy Conversion*, page 4533, Miami, FL, 2007.

[48] D.A. Anderson, J.C. Tannehill, and R.H. Pletcher. *Computational Fluid Mechanics and Heat Transfer*. Taylor & Francis, New York, 1984.

[49] A.V. Likhanskii, M.N. Shneider, S.O. Macheret, and R.B. Miles. Modeling of Interaction Between Weakly Ionized Near-Surface Plasmas and Gas Flow. In *44th AIAA Aerospace Sciences Meeting and Exhibit*, page 1204, Reno, NV, 2006.

[50] Alexandre V. Likhanskii, Mikhail N. Shneider, Sergey O. Macheret, and Richard B. Miles. Modeling of dielectric barrier discharge plasma actuators driven by repetitive nanosecond pulses. *Physics of Plasmas*, 14(7):073501, 2007.

[51] A.V. Likhanskii, M.N. Shneider, S.O. Macheret, and R.B. Miles. Optimization of Dielectric Barrier Discharge Plasma Actuators Driven By Repetitive Nanosecond Pulses. In *45th AIAA Aerospace Sciences Meeting and Exhibit*, Reno, NV, 2007.

[52] Francoise Massines, Ahmed Rabehi, Philippe Decomps, Rami Ben Gadri, Pierre Segur, and Christian Mayoux. Experimental and theoretical study of a glow discharge at atmospheric pressure controlled by dielectric barrier. *Journal of Applied Physics*, 83(6):2950, 1998.

[53] R.B. Gadri. One atmosphere glow discharge structure revealed by computer modeling. *IEEE Transactions on Plasma Science*, 27(1):36–37, 1999.

[54] J Reece Roth, Jozef Rahel, Xin Dai, and Daniel M Sherman. The physics and phenomenology of One Atmosphere Uniform Glow Discharge Plasma (OAUGDP) reactors for surface treatment applications. *Journal of Physics D: Applied Physics*, 38(4):555–567, February 2005.

[55] G.I. Font, C.L. Enloe, T.E. McLaughlin, and D.M. Orlov. Plasma Discharge Characteristics and Experimentally Determined Boundary Conditions for a Plasma Actuator. In *45th AIAA Aerospace Sciences Meeting and Exhibit*, page 188, Reno, NV, 2007.

[56] C.L. Enloe, T.E. McLaughlin, J. Gregory, R. Medina, and W. Miller. Surface Potential and Electric Field Structure in the Aerodynamic Plasma Actuator. In *46th AIAA Aerospace Sciences Meeting and Exhibit*, page 1103, Reno, NV, 2008.

[57] Yu.P. Raizer, M.N. Shneider, and N.A. Yatsenko. *Radio-Frequency Capacitive Discharges*. CRC Press, 1995.

[58] C. Louste, E. Moreau, and G. Touchard. Sliding discharge in air at atmospheric pressure: mechanical properties. In *Proceedings of the ESA-IAS-IEJ Joint Symposium*, Berkeley, CA, 2006.

[59] C. Louste, G. Artane, E. Moreau, and G. Touchard. Sliding discharge in air at atmospheric pressure: electrical properties. *Journal of Electrostatics*, 63(6-10):615–620, June 2005.

[60] B. Arad, Y. Gazit, and A. Ludmirsky. A sliding discharge device for producing cylindrical shock waves. *Journal of Physics D: Applied Physics*, 20(3):360, 1987.

[61] J. Gregory, C.L. Enloe, G.I. Font, and T.E. McLaughlin. Force Production Mechanisms of a Dielectric-Barrier Discharge Plasma Actuator. In *45th AIAA Aerospace Sciences Meeting and Exhibit*, page 185, Reno, NV, 2007.

[62] R.A. Serway. *Principles of Physics*. Saunders College Publishing, Fort Worth, TX, 2nd edition, 1998.

[63] S. Guo, D. Poon, M. Mamunuru, T. Simon, D. Ernie, and U. Kortshagen. Separation Control Using DBD Plasma Actuators: Designs for Thrust Enhancement. In *39th AIAA Fluid Dynamics Conference*, page 4184, San Antonio, TX, 2009.

[64] S. Guo, T. Simon, D. Ernie, and U. Kortshagen. Separation Control Using DBD Plasma Actuators: Thrust Enhancement Studies. In *48th AIAA Aerospace Sciences Meeting*, page 1090, Orlando, FL, 2010.

[65] Dmitry F. Opaits, Alexandre V. Likhanskii, Gabriele Neretti, Sohail Zaidi, Mikhail N. Shneider, Richard B. Miles, and Sergey O. Macheret. Experimental investigation of dielectric barrier discharge plasma actuators driven by repetitive high-voltage nanosecond pulses with dc or low frequency sinusoidal bias. *Journal of Applied Physics*, 104(4):043304, 2008.

[66] D. F. Opaits, M. N. Shneider, Richard B. Miles, A. V. Likhanskii, and S. O. Macheret. Surface charge in dielectric barrier discharge plasma actuators. *Physics of Plasmas*, 15(7):073505, 2008.

[67] R. B. Miles, D. F. Opaits, M. N. Shneider, S. H. Zaidi, and S. O. Macheret. Non-thermal atmospheric pressure plasmas for aeronautic applications. *The European Physical Journal Applied Physics*, 47(2):22802, May 2009.

[68] Jesse Little, Munetake Nishihara, Igor Adamovich, and Mo Samimy. High-lift airfoil trailing edge separation control using a single dielectric barrier discharge plasma actuator. *Experiments in Fluids*, 48(3):521–537, October 2009.

[69] C.L. Enloe, M. McHarg, G.I. Font, and T.E. McLaughlin. Plasma-induced Force and Self-induced Drag in the Dielectric Barrier Discharge Aerodynamic Plasma Actuator. In *47th AIAA Aerospace Sciences Meeting including The New Horizons Forum and Aerospace Exposition*, page 1622, Orlando, FL, 2009.

[70] G.I. Font, C.L. Enloe, and T.E. McLaughlin. Effect of Volumetric Momentum Addition on the Total Force Production of a Plasma Actuator. In *39th AIAA Fluid Dynamics Conference*, page 4285, San Antonio, TX, 2009.

[71] N.I. Akantov. *Expansion of flat laminar liquid jet along hard wall*, pages 24–31. Mashgis, Leningrad, USSR, 1952.

[72] M. B. Glauert. The wall jet. *Journal of Fluid Mechanics*, 1(06):625–643, March 1956.

[73] L.G. Loitsanskii. *Liquid and gas mechanics*. Nauka, Moscow, 1970.

[74] C.L. Enloe, T.E. McLaughlin, R.D. VanDyken, and K.D. Kachner. Mechanisms and responses of a single dielectric barrier plasma actuator: plasma morphology. *AIAA journal*, 42(3):589, 2004.

[75] C.L. Enloe, T.C. Corke, O. Haddad, E. Jumper, K. Kachner, T.E. McLaughlin, M. Post, and R.D. Van Dyken. Mechanisms and Responses of a Dielectric Barrier Plasma Actuator: Geometric Effects. *AIAA Journal*, 42(3):595–604, March 2004.

[76] T Unfer and J P Boeuf. Modelling of a nanosecond surface discharge actuator. *Journal of Physics D: Applied Physics*, 42(19):194017, October 2009.

[77] AV Likhanskii, MN Shneider, and SO Macheret. Modeling of dielectric barrier discharge plasma actuator in air. *Journal of Applied ...*, 2008.

[78] D.V. Roupassov, I.N. Zavyalov, and A.Yu. Starikovskii. Boundary Layer Separation Plasma Control Using Low-Temperature Non-Equilibrium Plasma of Gas Discharge. In *44th AIAA Aerospace Sciences Meeting and Exhibit*, page 373, Reno, NV, 2006.

[79] A. Lapucci, F. Rossetti, M. Giofini, and G. Orlando. On the longitudinal voltage distribution in radio-frequency-discharged CO2 lasers with large-area electrodes. *IEEE J. Quantum Electron*, 31(8):1537–1542, 1995.

[80] Yu.P. Raizer and M.N. Shneider. Radio-frequency capacitive discharge in a long strip line. *IEEE Transactions on Plasma Science*, 26(3):1017–1021, June 1998.

[81] M A Lieberman, J P Booth, P Chabert, J M Rax, and M M Turner. Standing wave and skin effects in large-area, high-frequency capacitive discharges. *Plasma Sources Science and Technology*, 11(3):283–293, August 2002.

[82] PD Lax and B Wendroff. Systems of conservative laws. *Comm. Pure Appl. Math*, 13:213, 1960.

[83] E.S. Oran and J.P. Boris. *Numerical Simulation of Reactive Flow*. Cambridge University Press, Cambridge, 2000.

[84] Y.N. Dnestrovskii and D.P. Kostomarov. *Numerical Simulation of Plasmas*. Springer, Berlin, 1985.

[85] P.N. Herbert. *Introductory Electromagnetics*. Wiley, New York, 1991.

[86] J Orphal. A critical review of the absorption cross-sections of O3 and NO2 in the ultraviolet and visible. *Journal of Photochemistry and Photobiology A: Chemistry*, 157(2-3):185–209, May 2003.

[87] D. Daumont, J. Brion, J. Charbonnier, and J. Malicet. Ozone UV spectroscopy I: Absorption cross-sections at room temperature. *Journal of Atmospheric Chemistry*, 15(2):145–155, August 1992.

[88] R R Dickerson and D H Stedman. Qualitative and quantitative flow visualization technique using ozone. *The Review of scientific instruments*, 50(6):705, June 1979.

[89] US Enviromental Protection Agency. Ozone Air Quality Standards, 2010.

[90] D. S. Stevenson, F. J. Dentener, M. G. Schultz, K. Ellingsen, T. P. C. van Noije, O. Wild, G. Zeng, M. Amann, C. S. Atherton, N. Bell, D. J. Bergmann, I. Bey, T. Butler, J. Cofala, W. J. Collins, R. G. Derwent, R. M. Doherty, J. Drevet, H. J. Eskes, A. M. Fiore, M. Gauss, D. A. Hauglustaine, L. W. Horowitz, I. S. A. Isaksen, M. C. Krol, J.-F. Lamarque, M. G. Lawrence, V. Montanaro, J.-F. Müller, G. Pitari, M. J. Prather, J. A. Pyle, S. Rast, J. M. Rodriguez, M. G. Sanderson, N. H. Savage, D. T. Shindell, S. E. Strahan, K. Sudo, and S. Szopa. Multimodel ensemble simulations of present-day and near-future tropospheric ozone. *Journal of Geophysical Research*, 111(D8), 2006.

REPORT DOCUMENTATION PAGE		Form Approved OMB No. 0704-0188

1. REPORT DATE *(DD-MM-YYYY)*	2. REPORT TYPE	3. DATES COVERED *(From - To)*
01-09-2012	Final Contractor Report	

4. TITLE AND SUBTITLE
Dielectric Barrier Discharge Plasma Actuator for Flow Control
Final Report

5a. CONTRACT NUMBER
NNX07AC02A

5b. GRANT NUMBER

5c. PROGRAM ELEMENT NUMBER

6. AUTHOR(S)
Opaits, Dmitry, F.

5d. PROJECT NUMBER

5e. TASK NUMBER

5f. WORK UNIT NUMBER
WBS 561581.02.08.03.21.66

7. PERFORMING ORGANIZATION NAME(S) AND ADDRESS(ES)
Princeton University
Princeton, New Jersey 08544

8. PERFORMING ORGANIZATION REPORT NUMBER
E-18232

9. SPONSORING/MONITORING AGENCY NAME(S) AND ADDRESS(ES)
National Aeronautics and Space Administration
Washington, DC 20546-0001

10. SPONSORING/MONITOR'S ACRONYM(S)
NASA

11. SPONSORING/MONITORING REPORT NUMBER
NASA/CR-2012-217655

12. DISTRIBUTION/AVAILABILITY STATEMENT
Unclassified-Unlimited
Subject Categories: 02, 07, 34, and 75
Available electronically at http://www.sti.nasa.gov
This publication is available from the NASA Center for AeroSpace Information, 443-757-5802

13. SUPPLEMENTARY NOTES
This report was submitted as a dissertation in partial fulfillment of the requirements for the degree Doctor of Philosophy to Princeton University, Department of Mechanical and Aerospace Engineering, Princeton, New Jersey, September 2010. Grant technical monitor, David E. Ashpis, Aeropropulsion Division, Glenn Research Center, organization code RTTO, ashpis@nasa.gov

14. ABSTRACT
This report is Part II of the final report of NASA Cooperative Agreement contract no. NNX07AC02A. It includes a Ph.D. dissertation. The period of performance was January 1, 2007 to December 31, 2010. Part I of the final report is the overview published as NASA/CR-2012-217654. Asymmetric dielectric barrier discharge (DBD) plasma actuators driven by nanosecond pulses superimposed on dc bias voltage are studied experimentally. This produces non-self-sustained discharge: the plasma is generated by repetitive short pulses, and the pushing of the gas occurs primarily due to the bias voltage. The parameters of ionizing pulses and the driving bias voltage can be varied independently, which adds flexibility to control and optimization of the actuators performance. The approach consisted of three elements coupled together: the Schlieren technique, burst mode of plasma actuator operation, and 2-D numerical fluid modeling. During the experiments, it was found that DBD performance is severely limited by surface charge accumulation on the dielectric. Several ways to mitigate the surface charge were found: using a reversing DC bias potential, three-electrode configuration, slightly conductive dielectrics, and semi conductive coatings. Force balance measurements proved the effectiveness of the suggested configurations and advantages of the new voltage profile (pulses+bias) over the traditional sinusoidal one at relatively low voltages. In view of practical applications certain questions have been also addressed, such as electrodynamic effects which accompany scaling of the actuators to real size models, and environmental effects of ozone production by the plasma actuators.

15. SUBJECT TERMS
Flow control; Tubomachinery; Low pressure turbine; Turbulence; Wall jet; Separation; Dielectric barrier discharge plasma; DBD; Electric field; Dielectric; Electrode; Glow discharge nanosecond pulsing

16. SECURITY CLASSIFICATION OF:			17. LIMITATION OF ABSTRACT	18. NUMBER OF PAGES	19a. NAME OF RESPONSIBLE PERSON
a. REPORT	b. ABSTRACT	c. THIS PAGE			STI Help Desk (email:help@sti.nasa.gov)
U	U	U	UU	162	19b. TELEPHONE NUMBER *(include area code)* 443-757-5802